Geofísica Internacional

— Geofísica Internacional —

Contents

Evaluation of soil liquefaction from surface analysis.
Efraín Ovando Shelley, Vanessa Mussio, Miguel Rodríguez, José G. Acosta Chang

Two algorithms to compute the electric resistivity response using Green's functions for 3D structures

E. Leticia Flores-Márquez*, Andrés Tejero-Andrade, Adrián León-Sánchez, Claudia Arango-Galván and René Chávez-Segura

Resumen

Se introduce una solución integral para el problema directo de la respuesta geoeléctrica DC para cuerpos tri-dimensionales en un semi-espacio, mediante las funciones de Green. El primer algoritmo que se presenta se basa en el método integral de volumen (MIV); aquí, únicamente la corriente eléctrica primaria se utiliza para calcular el potencial eléctrico. El segundo caso emplea el método integral de superficie (MIS), en donde se asume que la carga inducida es debida al campo eléctrico primario. Ambos algoritmos son una combinación de integrales de volumen y de condiciones de frontera. Este artículo muestra la aplicabilidad de estos algoritmos para generar imágenes de perfiles de resistividad que reproducen algunos arreglos de electrodos para ejemplos sintéticos tradicionales, y posteriormente estas imágenes se comparan con resultados ya publicados en la literatura. Finalmente, la comparación entre estos resultados muestra que el concepto de carga inducida utilizada en MIS produce una mejor aproximación, que el esquema MIV en el cálculo del potencial eléctrico.

Palabras Clave: Modelo eléctrico 3D, funciones de Green, método integral, teorema de Gauss, condiciones de frontera.

Abstract

An integral solution of the forward DC geoelectric response for three-dimensional target-bodies in a half-space, based on Green's functions, is introduced. The first algorithm presented is based on a volume integral method (*VIM*); here, only the primary electrical current is involved to compute the electric potential. The second one employs the surface integral method (*SIM*), and it is assumed the induced charge is due to the primary electrical field. Both algorithms are a combination of boundary and volume integrals. This paper shows the applicability of these algorithms to generate resistivity profile images reproducing some electrode arrays for traditional synthetic examples, and then these images were compared with already published results. Finally, the comparison between results shows the concept of induced charge used in *SIM* produces a better approach than *VIM* scheme in computing the electrical potential.

Keywords: 3D electrical model, Green's functions, integral method, Gauss theorem, Boundary conditions.

E. L.Flores-Márquez
C. Arango-Galván
R. Chávez-Segura
Instituto de Geofísica
Universidad Nacional Autónoma de México
Circuito Exterior, Cd. Universitaria
04510 México D.F., México
*Corresponding author: leticia@geofisica.unam.mx

A. Tejero-Andrade
A. León-Sánchez
División de Ciencias de la Tierra
Facultad de Ingeniería
Universidad Nacional Autónoma de México
Circuito Interior, Cd. Universitaria
04510 México D.F., México

Introduction

The last three decades have been characterized by an increased use of computerized methods in the interpretation of geoelectrical data, due to the evolution of the computer systems. Most reconstructive algorithms are iterative and need a forward solution, i.e., to compute the electrical response for a given resistivity distribution and a given set array of current injection electrodes. Thus, the electrical potential needs to be calculated at a set of measured points. This forward problem consists on solving an elliptic partial differential equation (PDE): the Poisson equation, with boundary conditions. The formulation leads to solve a system with two kinds of unknown quantities: the electrical potential and a current-related quantity.

The PDE problem is usually solved with finite-difference schemes that specially has been helpful to compute the apparent electrical resistivity in a two-dimensional medium (e.g. Forsythe and Wasow, 1960; Mufti, 1976; Dey and Morrison, 1979; Marchuk, 1989; Thomée, 1989; Spitzer, 1995; Zhang *et al*., 1995; Loke and Barker, 1996). Another scheme extensively used in solving this PDE problem has been finite-element scheme (e.g. Coggon, 1971; Strang and Fix, 1973; Wait, 1977; Fox *et al.*, 1980; Pridmore *et al.*, 1980; Johnson, 1987; Ciarlet, 1991; Sasaki, 1994; Tsourlous and Ogilvy; 1999; Li and Spitzer, 2002, 2005; Marescot *et al.*, 2008; Ren and Tang, 2010). Finite volume schemes have also produced excellent results in computing electrical resistivity (e.g. Snyder, 1976; Baliga and Patankar, 1980; Cai *et al.*, 1991; Eskola, 1992; Perez-Flores, 1995; Perez-Flores *et al.*, 2001; León-Sánchez, 2004; Pidlisecky et al., 2007). The methods based on a finite-element scheme have been widely studied in the past 40 years and give rise to very high-performing techniques as mixed methods (Lesur *et al.*, 1999), or h-p methods (Babuska and Suri, 1994). Nevertheless, the already mentioned methods lead to very large systems of linear equations, which are very demanding even for the supercomputers.

One limitation in integral methods is the heterogeneity of the medium and the geometrical complexity of the bodies immersed in the modeled medium. An alternative to reduce this limitation is to propose a linearization procedure or some hypothesis about the interaction between bodies, as the weak scattering problem (Eskola, 1992; Hvozdara and Kaikkonen, 1998). Such alternatives make integral equation method a good option to solve PDE, since this method does not need linearization, even in the case of bodies with complex geometry.

The boundary-element methods (BEM) (Okabe, 1981; Nedelec, 1985, 1994; Wendland, 1987) can be thought as a particular version among the finite-element methods. An example of the application of this method to 3-D electrical modeling can be found in Poirmeur and Vasseur (1988). In this methodology, only the boundaries between media, of constant resistivity, need to be discretized and integrated. Therefore, unbounded homogeneous media are easily treated, and 3-D problems are solved using only 2-D integrals. Moreover, the boundary-element method can be coupled with standard finite element methods. The modification of the integral equations method with BEM, introduced by Hvozdara and Kaikkonen (1998), is physically more meaningful and not so much demanding on computer resources, which made the method more accessible for routine prospecting work.

This work follows the integral solution of the forward DC geoelectrical problem introduced
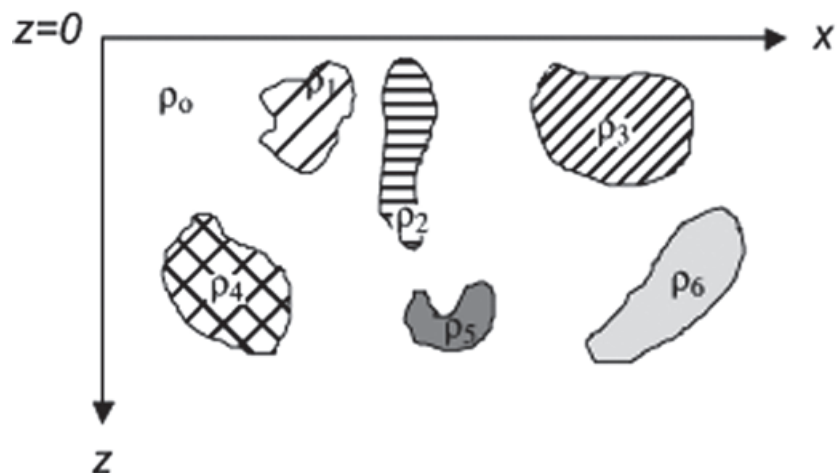
Figure 1. Conceptual model of a heterogeneous half-space formed by some bodies, with different but constant resistivity values, $\rho_1 \cdots \rho_6$, immersed in a homogeneous medium with a constant resistivity value ρ_0.

by Hvozdara and Kaikkonen (1998; Hvozdara, 1982), which consists of interpreting the electric response of three-dimensional disturbing body of non-uniform conductivity, immersed in a planar homogeneous half-space, under the assumption of weak scattering (Figure 1). In this research two algorithms are proposed to solve this forward problem, by introducing the resistivity contrast between bodies and the homogeneous half-space and the concepts of: additive potential sources for immersed bodies and density surface charges, which result in two types of solutions: volume (*VIM*) and surface integral methods (*SIM*). *SIM* and BEM use the same theoretical background but the boundary surfaces in *SIM* are not discretized and therefore no finite element is employed. *SIM* and *VIM* are used to solve the geoelectrical problem, with mixed boundary conditions, by considering a dipole-dipole electrode array to reproduce an electric tomography profile. The results of some synthetic examples are compared with those obtained by alternative methods in solving PDE already published by other authors (e.g. Tsourlos and Ogilvy, 1999; Pridmore, 1978; Hvozdara and Kaikkonen, 1998; Perez-Flores *et al.*, 2001).

Theoretical Setting

For a 3D heterogeneous half-space with a resistivity $\rho(\bar{r})$, the total electric potential for a point source at the surface $z = 0$, is expressed by:

$$\nabla \cdot \left[\frac{\nabla U(\bar{r})}{\rho(\bar{r})} \right] = -I\delta(\bar{r}) \quad z \geq 0$$

$$\left. \begin{array}{l} \dfrac{\partial U(\bar{r})}{\partial(z)} = 0; \qquad z = 0 \\[2mm] U(r) = 0 \text{ when } r \to \infty \text{ and } z \geq 0 \end{array} \right\} \text{boundary conditions}$$

$$(1)$$

This PDE problem with boundary conditions can be rewritten as:

$$\nabla^2 U(\bar{r}) = -I\rho(\bar{r})\delta(\bar{r}) - \rho(\bar{r})\nabla(1/)\rho(\bar{r})) \cdot \nabla U(\bar{r})$$

$$(2)$$

One solution for this equation can be expressed for the potential U(r) using the Green's theorems and Green's function method:

$$U(\bar{r}) = \int_V \nabla' U(\bar{r}) \cdot \nabla' G(\bar{r},\bar{r}') dV - \oint_S U(\bar{r})\nabla' G(\bar{r},\bar{r}') \cdot d\bar{S}$$

$$(3)$$

where $\vec{r}' = (x',y',z')$ is related to *local coordinates system,* $\vec{r} = (x,y,z)$ related to

global coordinates system, and $\oint_S$ denotes the integral over the boundaries *s*. In particular the integral over all boundaries can be written as:

$$\oint_S U(\vec{r})\nabla' G(\vec{r},\vec{r}') \cdot d\vec{S} = \oint_{z=0} U(\vec{r})\nabla' G(\vec{r},\vec{r}') \cdot d\vec{S} + \oint_{S_r} U(\vec{r})\nabla' G(\vec{r},\vec{r}') \cdot d\vec{S}$$

Where $\oint_{S_r} U(\vec{r})\nabla' G(\vec{r},\vec{r}') \cdot d\vec{S} = 0$ if , $\vec{r} \to \infty$ due to the boundary conditions (Hvozdara and Kaikkonen, 1998), and G is the Green's function. Green's function, G, is is defined for a half-space problem (eq. 3) for Neumann condition, where

$$\left[\frac{\partial G}{\partial z}_{z=0} \right] = 0.$$

$\nabla' U(\vec{r}') = -\vec{E}(\vec{r}')$ and by using $\vec{E}(\vec{r}') = \rho(\vec{r}')\vec{J}(\vec{r}')$, the expression (3) can be rewritten as

$$U(\vec{r}') = -\int_V \rho(\vec{r}')\vec{J}(\vec{r}') \cdot \nabla' G(\vec{r},(\vec{r}')dV$$

$$(4)$$

The *Volume Integral Method (VIM)* evaluates U(r) from equation (4), so it is necessary to know the current density function $\vec{J}(\vec{r})$ in half-space. The computation of $\vec{J}(\vec{r})$ is not an easy task, since there are several types of currents involved, particularly those present in the heterogeneous half-space. The "weak scattering problem" assumes that the primary conduction current is more significant that the secondary, that is $\left| \vec{J}_2(\vec{r}) \right| << \left| \vec{J}_p(\vec{r}) \right|$ (Eskola, 1992). Due to the interaction between bodies, we can express $\vec{J}_p(\vec{r})$ as:

$$\vec{J}_p(\vec{r}) = \frac{I}{2\pi} \left[\frac{(x - x_S)\vec{i} + (y - y_S)\vec{j} - z\vec{k}}{\left[(x - x_S)^2 + (y - y_S)^2 + z^2 \right]^{\frac{3}{2}}} \right]$$

$$(5)$$

where sub-index *s* represents the location of source electrodes.

The Neumann Green function for half space can be defined, as was done by Kaufman (1992) as:

$$G(\vec{r},\vec{r}') = \frac{1}{4\pi} \left(\frac{1}{\left(r_g^2 + (z - z')^2 \right)^{\frac{1}{2}}} + \frac{1}{\left(r_g^2 + (z + z')^2 \right)^{\frac{1}{2}}} \right)$$

$$(6)$$

where $r_g^2 = (x - x')^2 + (y - y')^2$. Introducing this definition into eq. 4, and evaluating eq. 5 in $z = 0$, it becomes:

$$U(\vec{r}) = -\frac{I}{4\pi^2} \int_V \left[\frac{(x'-x_s)(x-x')+(y'-y_s)(y-y')-z'^2}{\left[(x'-x_s)^2+(y'-y_s)^2+z'^2\right]^{3/2}\left[(x-x')^2+(y-y')^2+z'^2\right]^{3/2}} \rho(x',y',z') \right] dV \tag{7}$$

Gómez-Treviño (1987), Pérez-Flores *et al.* (2001) and León-Sánchez (2004) used a similar relation to estimate the apparent resistivity $\rho_a(\vec{r})$ in a heterogeneous half-space.

Also $U(\vec{r})$ can be expressed as a surface integral, leading to the *Surface Integral Method* **(SIM)**. If $\rho(\vec{r})\vec{J}(\vec{r}) = \vec{E}_p(\vec{r}) = \vec{E}_p(\vec{r}) + \vec{E}_2(\vec{r})$ then eq. (4) can be rewritten as:

$$U(\vec{r}) = -\int_V \vec{E}_p(\vec{r}) \cdot \nabla' G(\vec{r},\vec{r}') dV - \int_V \vec{E}_2(\vec{r}) \cdot \nabla' G(\vec{r},\vec{r}') dV \tag{8}$$

Here $\vec{E}_p(\vec{r})$ is the primary electrical field due to the point source and $\vec{E}_2(\vec{r})$ the secondary electric field due to the heterogeneities of the medium.

The first term of the right hand of equation (7) is equal to the primary source's potential $U_p(\vec{r})$. The second term implies the whole half-space volume. This integral could be separated in volumes for each heterogeneous body, for instance if we define:

$$-\int_V \vec{E}_2(\vec{r}) \cdot \nabla G(\vec{r},\vec{r}') dV = \sum_{i=1}^{N} \int_{V_i} \vec{E}_{2,i}(\vec{r}) \cdot \nabla G(\vec{r},\vec{r}') dV_i' \tag{9}$$

Using the next vector property for each V_i,

$$\nabla' \cdot \left(\vec{E}_2(\vec{r}) G(\vec{r},\vec{r}') \right) = \vec{E}_2(\vec{r}) \cdot \nabla' G(\vec{r},\vec{r}') + G(\vec{r},\vec{r}') \nabla' \cdot \vec{E}_2(\vec{r}) \tag{10}$$

and assuming that the resistivity of each body within the half-space (Figure 1), is constant, then $\nabla' \cdot \vec{E}_2(\vec{r}') = 0$. Thus, we can use the divergence theorem for each V_i and eq. 8 becomes:

$$\int_{V_i} \vec{E}_2(\vec{r}) \cdot \nabla' G(\vec{r},\vec{r}') dV_i = \int_{V_i} \nabla' \cdot \left[\vec{E}_2(\vec{r}') G(\vec{r},\vec{r}') \right] dV_i = \int_{S_i} G(\vec{r},\vec{r}') \vec{E}_2(\vec{r}) dS_i \tag{11}$$

This equation should be applied to the whole surface delimitating each immersed body; in our case, we assume the body as a regular prism. Then, the corresponding integral for the case of two contiguous prismatic bodies (b_1, b_2) with a common surface, is:

$$\int_S \left(\vec{E}_{2,b_2}(\vec{r}') - \vec{E}_{2,b_1}(\vec{r}') \right) G(\vec{r},\vec{r}') \cdot \vec{n}_{b1,b2} dS \tag{12}$$

Where $\vec{n}_{12}$ is the unit normal vector of the surfaces (1, 2) between the two bodies.

The boundary conditions allow to define:

$$\left(\vec{E}_{2,b_2}(\vec{r}') - \vec{E}_{2,b_1}(\vec{r}') \right) \cdot \vec{n}_{b_1 b_2} = \frac{\sigma_s(\vec{r}')}{\varepsilon_0} \tag{13}$$

where $\sigma_s(\vec{r}')$ is the density surface charges and ε_0 is the free-space electrical permittivity.

Taking into account the equations (10 to 13), the electric potential (eq. 7) is rewritten as:

$$U(\vec{r}) = U_p(\vec{r}) + \sum_{j=1}^{M} \sum_{i=1}^{6} \frac{1}{\varepsilon_0} \int_{S_{i,j}} \sigma_{s,i,j}(\vec{r}') G(\vec{r},\vec{r}') dS'_{i,j} \tag{14}$$

Where number 6 denotes the total number of surfaces of one prismatic body and M the number of bodies within the half-space, this eq. constitutes the **SIM**.

Eskola (1992) has obtained an expression similar to equation (14) using different analytical approach, under the same type of hypothesis. However, a problem to solve is to know $\sigma(\vec{r}')$ (the density surface charges) for each surface of the each prismatic body. Kaufman (1992) expressed $\sigma(\vec{r}')$ for two contiguous surfaces as:

$$\sigma(\vec{r}') = 2\varepsilon_0 \frac{\rho_2 - \rho_1}{\rho_2 + \rho_1} \hat{E}_{\vec{n}}(\vec{r}') \tag{15}$$

where

$$\hat{E}_{\vec{n}} = \frac{\vec{E}_{\vec{n},b_1}(\vec{r}') + \vec{E}_{\vec{n},b_2}(\vec{r}')}{2} = \frac{2\vec{E}_p^{\vec{n}}(\vec{r}') + \vec{E}_{2,b_1}^{\vec{n}}(\vec{r}') + \vec{E}_{2,b_2}^{\vec{n}}(\vec{r}')}{2} \tag{16}$$

If we neglect the normal electrical secondary field in expression (16), *i.e.* $\vec{E}_{2,b_1}^{\vec{n}}(\vec{r}')$ and, $\vec{E}_{2,b_2}^{\vec{n}}(\vec{r}')$ then the equation (15) becomes:

$$\sigma_s(\vec{r}') = 2\varepsilon_0 \frac{\rho_2 - \rho_1}{\rho_2 + \rho_1} E_p^{\vec{n}}(\vec{r}') = 2\varepsilon_0 R_{12} E_p^{\vec{n}}(\vec{r}') \tag{17}$$

Where, R_{12}, is the reflectivity coefficient between surfaces. This expression is the approximation of the induced surface electric charge and it is equivalent to the so-called "*weak scattering problem"*.

Numerical Approach

Equations (6 and 14) are expressed in arbitrary coordinate systems with a fixed origin. However, to solve the corresponding integrals we redefine the origin of the coordinate system at the middle point of the prismatic body; that is the "*local coordinate system*". The transformation between both coordinate systems will be defined as follows: Assuming **P** an arbitrary point in the space, its position vector in terms of the global coordinates system is $\vec{r}$ and $\vec{r}'$ is its position vector in terms of the *local coordinate system*. Consequently, the relationship between the origins for both systems is defined by $\vec{r}_a$ (see Figure 2), that is:

$$\vec{r} = \vec{r}' + \vec{r}_a \qquad (18)$$

where $\vec{r}' = \left(x', y'z'\right)$, $\vec{r}_a = \left(x_a, y_a, z_a\right)$, and $\vec{r} = \left(x, y, z\right)$.

Assuming isolated heterogeneous bodies immersed in a half space, let us introduce the resistivity contrast as $\rho = \rho_c - \rho_m$, where ρ_m is the resistivity of the half-space and ρ_c is the resistivity of the immersed body.

Then, by applying equation (6) for a quadrupole array, that is to a vertical electric sounding (VES) (where electrodes are usually named: A, B, N, M, A and B indicate current electrodes and M and N reception electrodes), the potential U_{sN}^M associated with a point source electrode can be expressed as eq. (19). This equation also assumes the concept of additive potential sources (Orellana, 1972) :

$$\Delta U_{sN}^M = \frac{|I|}{4\pi^2} \Delta\rho \int_V \left[-\left[\frac{(x'-x_s)(x-x')+(y'-y_s)(y-y')-(z'+z_a)^2}{\left[(x'-x_s)^2+(y'-y_s)^2+(z'+z_a)^2\right]^{3/2}\left[(x-x')^2+(y-y')^2+(z'+z_a)^2\right]^{3/2}} \right]_{AM} \right.$$

$$+ \left[\frac{\left[(x'-x_s)(x-x')+(y'-y_s)(y-y')-(z'+z_a)^2\right]}{\left[(x'-x_s)^2+(y'-y_s)^2+(z'+z_a)^2\right]^{3/2}\left[(x-x')^2+(y-y')^2+(z'+z_a)^2\right]^{3/2}} \right]_{BM}$$

$$+ \left[\frac{\left[(x'-x_s)(x-x')+(y'-y_s)(y-y')-(z'+z_a)^2\right]}{\left[(x'-x_s)^2+(y'-y_s)^2+(z'+z_a)^2\right]^{3/2}\left[(x-x')^2+(y-y')^2+(z'+z_a)^2\right]^{3/2}} \right]_{AN}$$

$$\left. - \left[\frac{\left[(x'-x_s)(x-x')+(y'-y_s)(y-y')-(z'+z_a)^2\right]}{\left[(x'-x_s)^2+(y'-y_s)^2+(z'+z_a)^2\right]^{3/2}\left[(x-x')^2+(y-y')^2+(z'+z_a)^2\right]^{3/2}} \right]_{BN} \right] dV \qquad (19)$$

This equation allows us to compute the secondary electric potential by the volume integral method, **VIM**.

In the eq. 14, *SIM*, the density surface charges expressed in terms of the *local coordinates system* is:

$$\sigma\left(\vec{r}'\right) = 2\varepsilon_0 R_{12} \left[\frac{I\rho_M\left(\left(x'-x_s\right)\vec{i}+\left(y'-y_s\right)\vec{j}+\left(z+z_a\right)\vec{k}\right)}{2\pi\left[\left(x'-x_s\right)+\left(y-y_s\right)+\left(z+z_a\right)\right]^{3/2}} \right] \cdot \vec{n}_{12} \qquad (20)$$

By substituting equation (20) in equation (14), the contribution of each surface of the immersed body, to the secondary potential field for the same quadrupole array, is expressed as:

$$\frac{1}{\varepsilon_0}\int \sigma\left(\vec{r}'\right)G\left(\vec{r},\vec{r}'\right)dS = \frac{1}{2\pi\varepsilon_0}\int_s \left[\left(\frac{\sigma_A\left(\vec{r}'\right)}{\sqrt{(x-x')^2+(y-y')^2+(z+z_a)^2}} \right)_{AM} \right.$$
$$- \left(\frac{\sigma_B\left(\vec{r}'\right)}{\sqrt{(x-x')^2+(y-y')^2+(z+z_a)^2}} \right)_{BM}$$
$$- \left(\frac{\sigma_A\left(\vec{r}'\right)}{\sqrt{(x-x')^2+(y-y')^2+(z+z_a)^2}} \right)_{AN}$$
$$\left. + \left(\frac{\sigma_B\left(\vec{r}'\right)}{\sqrt{(x-x')^2+(y-y')^2+(z+z_a)^2}} \right)_{BN} \right] dS \qquad (21)$$

Then the apparent resistivity ρ_a can be expressed as:

$$\rho_a = \rho_m + \left(\frac{2\pi}{\dfrac{1}{AM} - \dfrac{1}{BM} - \dfrac{1}{AN} + \dfrac{1}{BN}} \right) \frac{\Delta U_N^M}{I} \qquad (22)$$

To solve the integrals involved in equations (19 and 21) (*VIM* and *SIM,* respectively) we use the Gauss-Legendre Quadrature, by using the subroutines QGAUS and DQDAGI, that are in-cluded in the IMLS Fortran numerical libraries (Meissner, 1995; Press *et al*., 1992). DQDAGI subroutine makes use of Gauss-Kronrod approximation with 21 points, and by using an *e*-algorithm (Piessens *et al*., 1983), these integrals can be estimated even when the ending interval is a singularity.

The computational program developed in this work computes the apparent resistivity profile for 3D inmersed bodies, by entering the data listed in table 1. The output data are the apparent resistivity values in an array that corresponds to a resistivity pseudo-section cutting the half-space in the input direction.

Synthetic examples

In order to illustrate the validity of the *VIM* and *SIM* developed in this work, we studied some synthetic examples and compared them to results obtained by others authors.
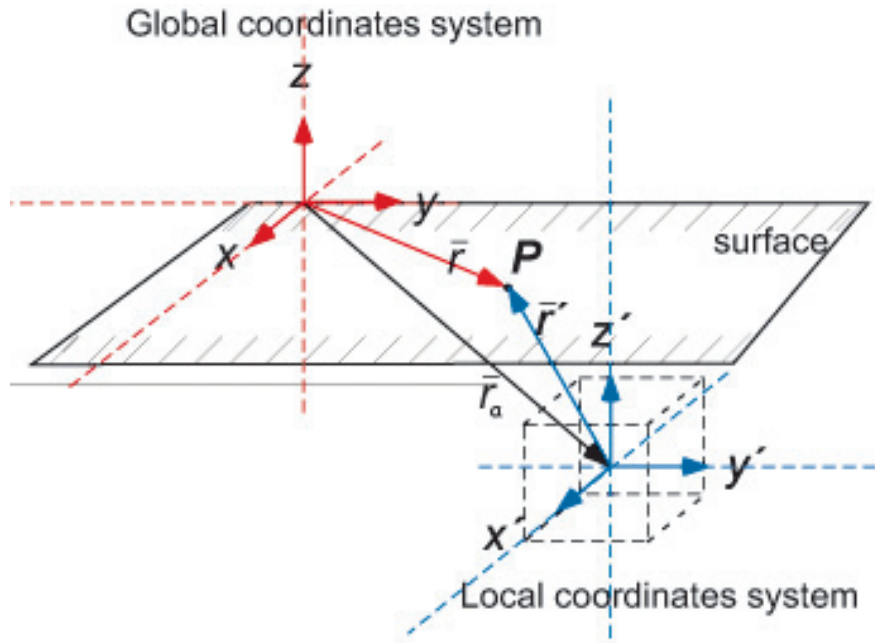
Figure 2. Relationship between two coordinate systems: global, refers to the external coordinates and local, that it is centered at the origin of the immersed resistive body $\vec{r} = \vec{r}' + \vec{r}_a$.
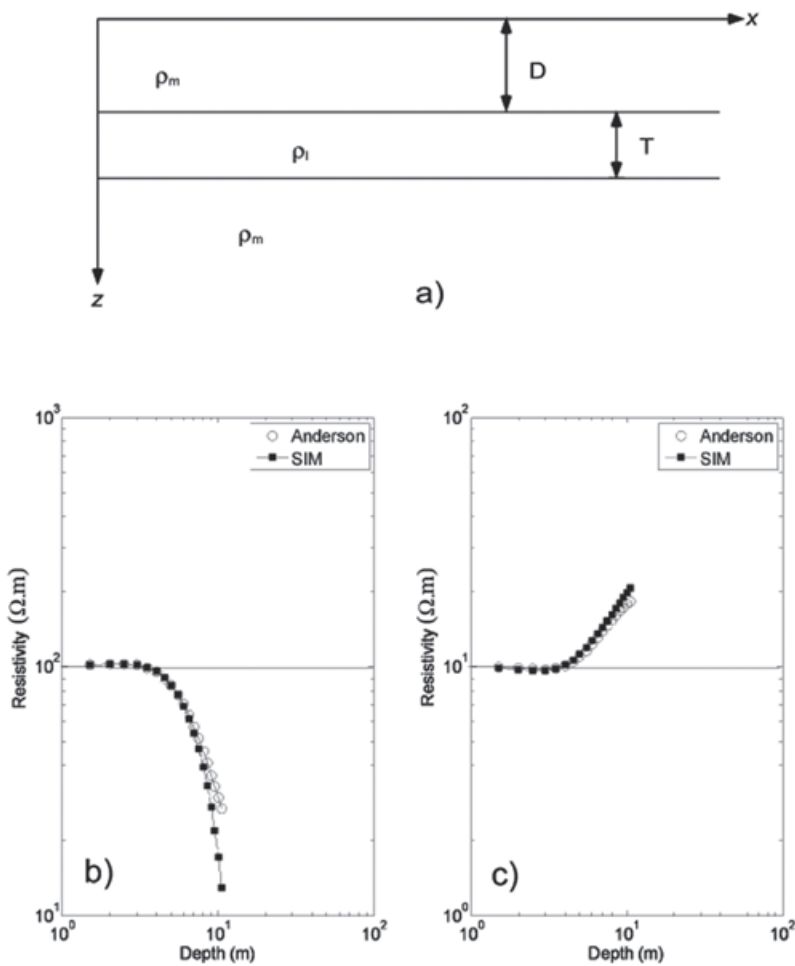
Figure 3. a) Synthetic example assuming a stratified half-space of three layers with D = 5 m and T = 2.5 m. The log-log plot shows the comparison between the SIM and the Anderson filter (Anderson, 1979) using two different contrasts of resistivities: b) a middle conductive layer with $\rho_m = 100\ \Omega m$, $\rho_l = 10\ \Omega m$ and c) a middle resistive stratum with $\rho_m = 10\ \Omega m$, $\rho_l = 100\ \Omega m$.

Table 1. Required data in the computational program to computes the apparent resistivity.

Input data
Electrode type array
Number of electrodes
Spacing between electrodes
Number of bodies
Location of bodies
Resistivity of each body
Resistivity of the half-space
Direction of the 2D output section

A stratified media, with three layers of different resistivities, constitutes the first example (Figure 3a). One case considers a middle conductor layer: 100, 10, 100 ohm-m (Figures 3b); and the other case considers a middle resistive layer: 10, 100, 10 ohm-m (Figure 3c). The results of the SIM model for a dipole-dipole array are compared (Figures 3b and 3c) to those results obtained by applying the algorithm based on the adaptive digital filtering proposed by Anderson (1979), which uses Hankel transforms. This comparison shows coincidences in the computed resistivity values at the subsurface assignation points corresponding to an electrodic separation of **a** = 1m, and until the level $n = 14$; however, after level $n = 15$ the results show differences between values (each level n corresponds to 0.5 m), because the computed induced charge by SIM is a poor approximation. It is important to point out that *SIM* is one method that needs to model closed bodies and the middle layer was considered as a body of 400 by 400 m and thickness of $T = 2.5$ m, the depth D = 5 m this assumption involves numerical errors that could explain the enlargement of the differences between both methods at depth (for levels n > 15 and depth > 10.5 m). But also it is important to point out the assumption of weak scattering concerns the use of Born approximation (Guozhong and Torres-Verdín, 2006) and this is also a contribution in those discrepancies, as it was signaled by Zhdanov and Fang (1996), the Born approximation produces curves of the correct shape but incorrect magnitude. In summary, we can conclude the approximation with SIM is good enough.

The second example consists of a 3D homogeneous half-space, with $\rho_m = 100$ ohm-m,

and one conductor immersed prismatic body, of $\rho_c = 20$ ohm-m (Figure 4). The results of VIM method (Figure 5a) shows differences between 3 and 21 ohm-m in the lower values region compared to those computed by Pridmore (1978); while the SIM modeling of a dipole-dipole array over the prism are compared (Figure 5b) to those obtained by Tsourlos and Ogilvy (1999). As it is observed, the differences between values are within 1 and 10 ohm-m. In contrast (Figure 5d), and only rise up to 14 ohm-m compared to those obtained by Tsourlos and Ogilvy (1999), Figure 5c. In spite of the differences depicted between the results of SIM and VIM, the results are good enough since the computed resistivity values do not exceed 15 ohm-m (Figures 5a and 5b). That is about 18 % of the resistivity contrast between body and half-space.

The third example showed in Figure. 6a, is constituted by the synthetic example published by Perez-Flores *et al.* (2001) with 4 immersed bodies of constant resistivity, $\rho_c = 20$ ohm-m. This model is based on a volume integral scheme (Perez-Flores *et al.*, 2001) and it is similar to the hypothesis of the *VIM* proposed here. The comparison between SIM and model shows similar results (Figure 6b). Also, the VIM shows quite the same data for this particular case (not showed in figure); however, for general cases, we would expect bigger differences from VIM results. A possible explanation is that the electrode separation is smaller than the dimensions of the bodies.

The fourth example presented consists of two conductive bodies (Figure 7) of $\rho_c = 20$ ohm-m, immersed in a homogeneous half-space of $\rho_m = 100$ ohm-m. The bodies have the same dimensions, 10 m thick (T, in the z direction), 10 m long (L, in the x direction) and 10 m width (W, in the y direction) and both are located at 2.5 m depth (D). This example is proposed just to show the interaction between bodies by changing the separation between them, with two possibilities: closer and distant (far) bodies, with S equal to 6 m and 40 m respectively. We assume a dipole-dipole array consisting of 31 electrodes, with a 5 m distance between them. Figure 8 shows the results obtained with *SIM* and *VIM* for the case with S = 6 m. The apparent resistivity values with *SIM* are those expected for the bodies. In contrast, *VIM's* resistivity values are bigger than those expected. It is important to point out that we obtain two minimum resistivities in the location corresponding to the bodies, as we expect, those anomalies in resistivities correspond to the bodies. However, it is also observed a third anomaly at the center of the resistivity image that corresponds to a
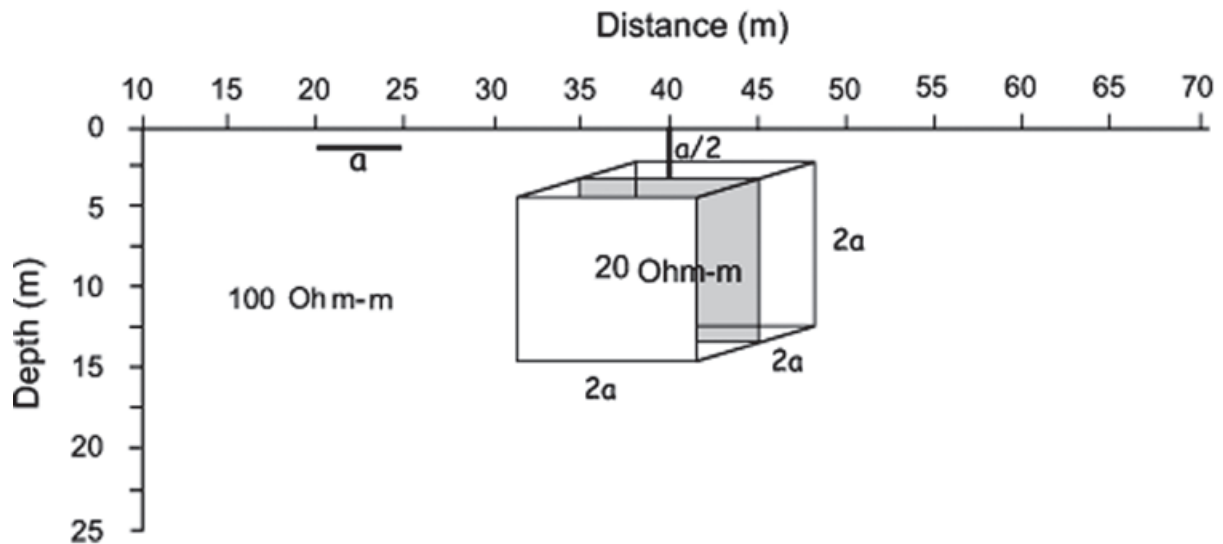
Figure 4. The schematic model shows a 3D body, $\rho_c = 20\ \Omega m$, immersed in a homogeneous half-space $\rho_m = 100\ \Omega m$. a/2 is the depth to the top of the body, 2a is the longitude of all sides of the cube, and a is the inter-electrode separation. Distance along the profile is x-coordinate (meters) and z-coordinate designates the positive depth (meters).
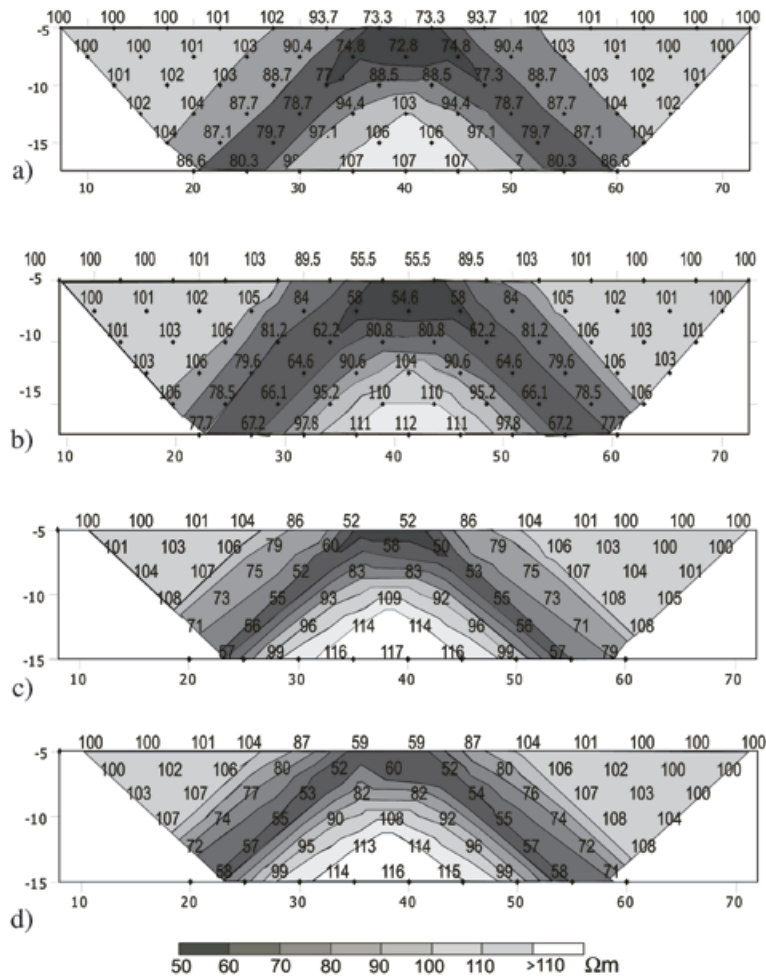
Figure 5. Comparison between results of the second example, constituted by the conductor immersed prismatic body shown in fig. 4, a) the results of the *VIM* model, b) the results of the *SIM* model, and those already published c) Tsourlos and Ogilvy (1999), and d) Pridmore (1978).
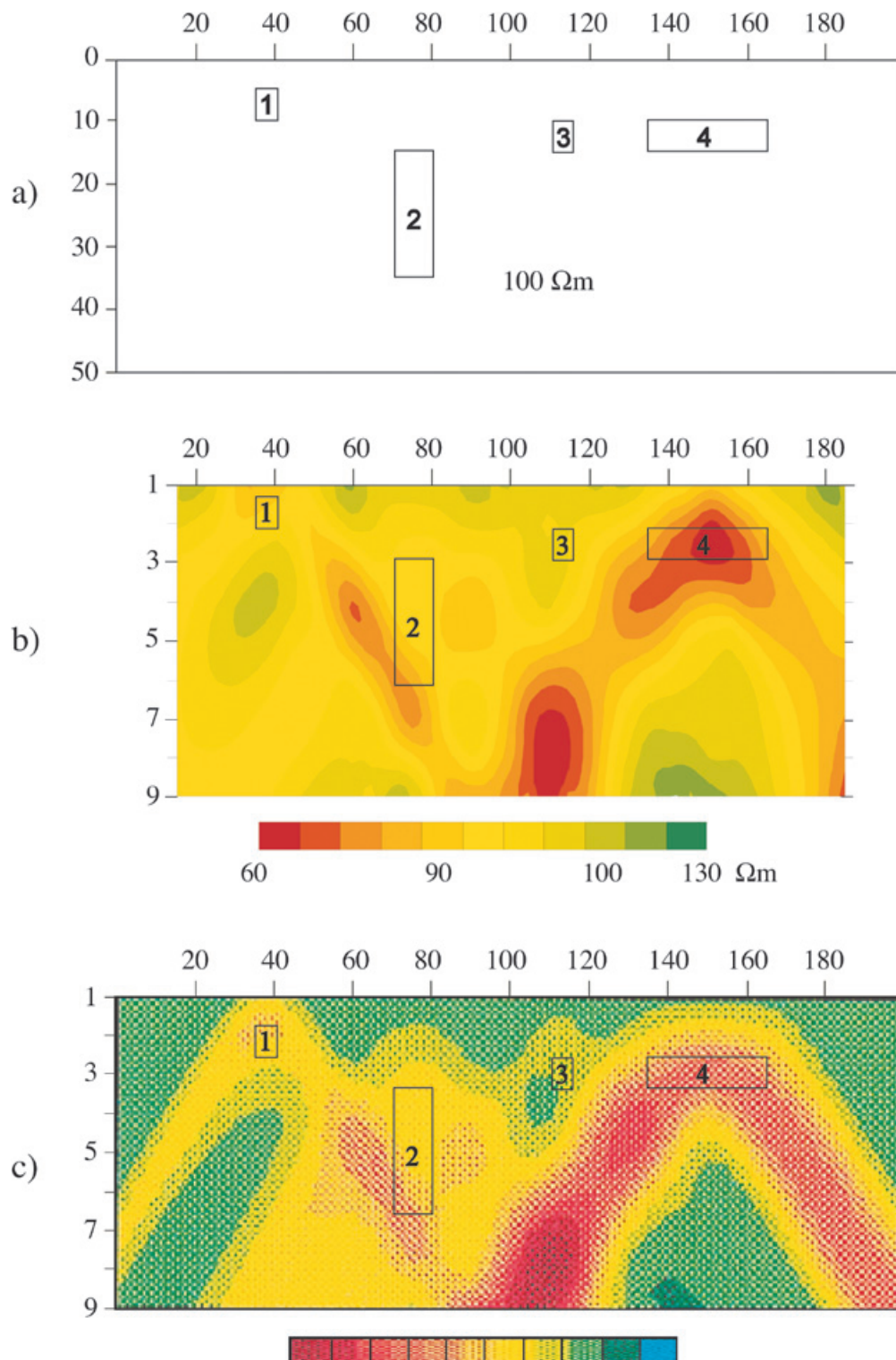
Figure 6. Third synthetic example constituted by (a) 4 immersed 3D bodies $\rho_c = 20$ Ωm in a homogeneous half space, b) The results of the *SIM* model, c) the results published by Pérez-Flores *et al.* (2001).
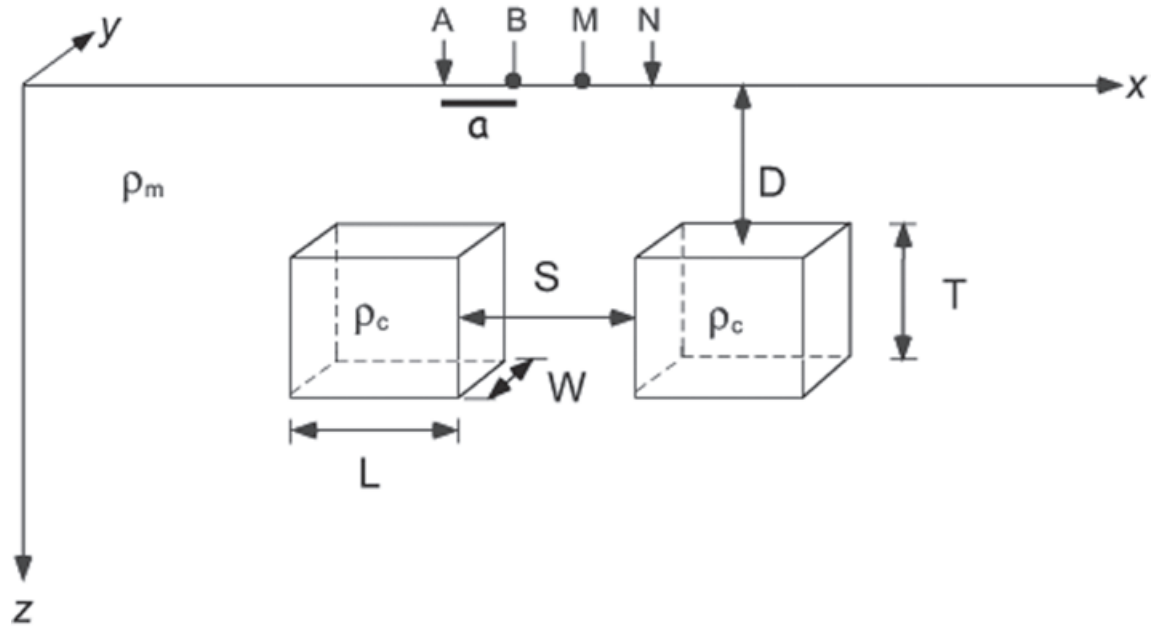
Figure 7. The schematic model shows a homogeneous half-space (ρ_m) and two immersed bodies of constant resistivity ρ_c. D is depth from soil to the top of the bodies (a /2), S is the horizontal distance between bodies, (T) high of bodies, (W) wide in y direction and (L) large in x direction, and a is the inter-electrodic separation.

Figure 8. Pseudo-section model obtained for the fourth example (figure 7), with $\rho_c = 20$ Ωm and $\rho_m = 100$ Ωm. Simulating a dipole-dipole array of 31 electrodes, with a = 5 m. The apparent resistivities were computed for separation between immerse bodies of S = 6 m. a) SIM and b) VIM.
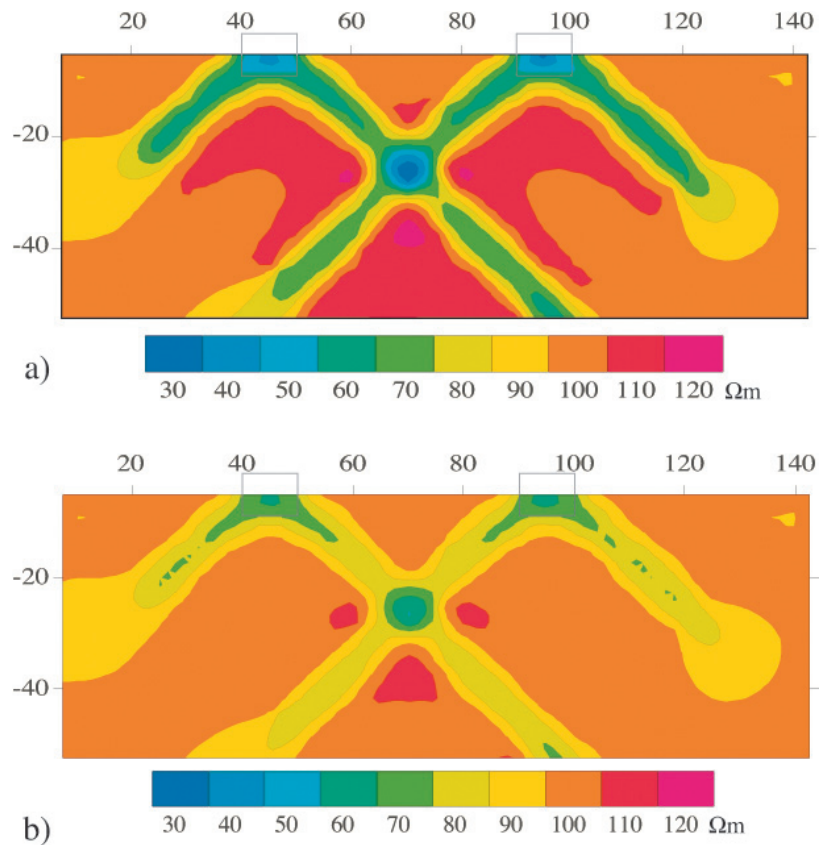
Figure 9. Pseudo-section model obtained for the same characteristic of the bodies of the fourth example (fig. 7), with $\rho_c = 20\ \Omega m$ and $\rho_m = 100\ \Omega m$, but for separation between immerse bodies of S = 40 m, simulating a dipole-dipole array of 31 electrodes, with a = 5 m, a) *SIM* and b) *VIM*.

numerical feature, of a lower resistivity value. Figure 9 shows results for the case S =40 m, they are similar to those obtained for isolate bodies (Figure 6). As well as previous case, it is also observed a third anomaly at the center of the resistivity image that corresponds to a numerical feature.

In all the studies cases, we can observe, *SIM* produces better approach than *VIM* in computing the electrical potential.

Conclusions

This paper introduces two algorithms for the integral solution of the forward DC geoelectrical problem introduced by Hvozdara and Kaikkonen (1998) with mixed boundary conditions using Green's function. The two types of solutions: volume (VIM) and surface integral methods (SIM) make use of the resistivity contrast between immersed bodies and the homogeneous half-space. These methods also use the concepts of: additive potential sources for immersed bodies, and density surface charges. Both algorithms are not so much demanding on computer time and memory because they do not produce to very large systems of linear equations. This

made the methods more accessible for personal computers, quotidian prospecting work and also makes it attractive for educational purposes. In particular could be useful to easily validate the field measurements interpretation.

The algorithms developed here can help in the interpretation of the field data obtained from resistivity profile methods, in two and three dimensions. The advantage of using the integral equation technique is that it is performed for each immersed body in the half space, in contrast to the usual procedure in finite-element and finite-difference methods. In order to find the induced charge, we do not need to define a grid on the surface of the body, due to the fact that we use the density surface charges on each surface.

The conducted tests with synthetic data indicated that both algorithms (SIM and VIM) produced reasonably good results compared to already published results for similar problems, obtained by other algorithms. The synthetic examples allow us to conclude that SIM produces a better approximation of the apparent resistivity values than those based on the volume integral (VIM).

These results are particularly attractive for computation in parallel, because they provide the mode to obtain the forward response for each body in simultaneous way.

Acknowledgements

References

Anderson W.L., 1979, Numerical integration of related Hankel transforms of orders 0 and 1 by adaptive digital filtering, *Geophysics*, 44, 1287–1305.

Arfken G.B., Mathematical methods for physicists (Academic Press, New York 1970).

Babuska I., Suri M., 1994, The p and h-p versions of the finite element method, basic principle and properties, SIAM Rev. 36, 578–632.

Baliga B.R., Patankar S.V., 1980, A new finite-element formulation for convection-diffusion problems, Numer. Heat Transfer 3, 393–409.

Cai Z., Mandel J., McCormick S., 1991, The finite volume element method for diffusion equations on general triangulations, SIAM J. Numer. Anal. 28, 392–402.

Ciarlet P.G., The finite element method for elliptic problems, In Handbook of numerical analysis (ed. Ciarlet, P.G., and Lions, J.L.) (North-Holland Publishing Co., Amsterdam 1991) pp. 17–351.

Coggon J.H., 1971, Electromagnetic and electrical modelling by the finite element method, *Geophysics* 36, 132–155.

Dey A., Morrison H.F., 1979, Resistivity modeling for arbitrarily shaped three-dimensional structures, *Geophysics* 44, 753–780.

Eskola L., Geophysical interpretation using integral equations (Chapman and Hall, London 1992).

Forsythe G.E., Wasow R., Finite difference methods for partial differential equations (Wiley, New York 1960).

Fox R.C., Hohmann G.W., Killpack T.J., Rijo L., 1980, Topographic effects in resistivity and induced-polarization surveys, *Geophysics* 45, 75–93.

Gómez-Treviño E., 1987, Nonlinear integral equations for electromagnetic inverse problems, *Geophysics* 52, 1297–1302.

Ghosh D.P., 1971, The application of linear filter theory to the direct interpretation of Geoelectric Sounding Measurement, *Geophys*. Prosp. 19, 192–217.

Guozhong G., Torres-Verdín C., 2006, High-Order Generalized Extended Born Approximation for Electromagnetic Scattering. IEEE *Transactions on Antennas and propagation*, 54-4, 1243-1256.

Griffits D.H., Turburllo J., 1985, A multi-electrode array for resistivity surveying, *First Break* 3, 16–20.

Hvozdara M., 1982, Potential field of a stationary electric courrent in a stratified medium with a three-dimensional perturbing body. Stud. *Geophys. Geod.* 26, 161-172.

Hvozdara M., Kaikkonen P., 1998, An integral equation solution of the forward D.C. geoelectric problem for a 3-D body of inhomogeneous conductivity buried in a halfspace. *J. of App*. Geophys. 39, 95-107.

Johnson C., Numerical solution of partial differential equations by finite element method (Cambridge University Press, Cambridge 1987).

Kauffman A.A., Geophysical field theory and method: Part A - Gravitational, electric and magnetic fields (Academic Press, St. Louis 1992).

León-Sánchez A.M., Modelación de la respuesta eléctrica de estructuras 3D en un semiespacio conductor, BSc thesis (UNAM, México 2004).

Lesur V., Cuer M., Straub A., 1999, 2-D and 3-D interpretation of electrical tomography measurements - Part 1: The forward problem, *Geophysics* 64, 396–402.

Li Y., Spitzer K., 2002, 3D direct current resistivity forward modeling using finite-element in comparison with finite-difference solutions, *Geophys. J. Int.* 151, 924–934.

Li Y., Spitzer K., 2005, Finite-element resistivity modeling for 3D structures with arbitrary anisotropy, Phys. *Earth Planet. Inter.* 150, 15–27.

Loke M.H., Barker R.D., 1996, Practical techniques for 3D resistivity surveys and data inversion, *Geophys.* Prosp. 44, 499–523.

Marchuk G.I., Splitting and alternative direction techniques, In Handbook of numerical analysis (ed. Ciarlet, P.G., and Lions, J.L.) (North-Holland Publishing Co., Amsterdam 1989) pp. 197–464.

Marescot L., Lopes S.P., Rigobert S., Green A.G., 2008, Nonlinear inversion of geoelectric data acquired across 3-D objects using a finite-element approach, *Geophysics* 73, F121–F133.

Meissner L.P., Fortran 90 (PWS Publishing Company, Boston 1995).

Mufti I.R., 1976, Finite-difference resistivity modeling for arbitrarily shaped two-dimensional structures, *Geophysics* 41, 62–78.

Nedelec J.C., 1985, Equations integrales associees aux problemes aux limites eliptiques dans les domaines de R^3, In Analyse mathematique et calcul numerique pour les sciences et les techniques (ed. Dautray, R., and Lions, J.L.) (Masson, Paris 1985) chap. XI, part B, pp. 645–702.

Nedelec J.C., 1994, New trends in the use and analysis of integral equations, *Proc. Sympos. Appl. Math.* 48, 151–176.

Okabe M., 1981, Boundary element method for the arbitrary inhomogeneities problem in electrical prospecting, *Geophys*. Prosp. 29, 39–59.

Oldenburg W.D., 1978, The interpretation of direct current resistivity measurements. *Geophysics* 43, 610–625.

Perez-Flores M.A., Méndez-Delgado S., Gomez-Treviño E., 2001, Imaging low frequency and dc electromagnetic fields using a simple linear approximation. *Geophysics* 66, 1067–1081.

Perez-Flores M.A., Inversión rápida en 2-D de datos de resistividad, magnetotelúricos y electromagnéticos de fuente controlada a bajo número de inducción, PhD thesis (Centro de Investigación Científica y de Estudios Superiores de Ensenada, Ensenada 1995).

Pidlisecky A., Haber E., Knight R., 2007, RESINVM3-D: A MATLAB 3-D resistivity inversion package, *Geophysics* 72, H1–H10.

Piessens R., deDoncker-Kapenga E., Uberhuber C., Kahaner C., Quadpack: a subroutine package for automatic integration (Springer-Verlag, Berlin 1983).

Poirmeur C., Vasseur G., 1988, Three-dimensional modeling of a hole-to-hole electrical method: Application to the interpretation of a field survey, *Geophysics,* 53 402–414.

Press W.H., Flannery B.P., Teukolsky S.A., Vetterling W.T., Numerical Recipes in Fortran (Cambridge University Press, Cambridge 1992).

Pridmore D., Three-dimensional modelling of electric and electromagnetic data using the finite element method, PhD thesis (University of Utah, Salt Lake City 1978).

Pridmore D.F., Hohmann G.W., Ward S.H., Sill W. R., 1980, An investigation of finite-element modeling for electrical and electromagnetical data in 3D, *Geophysics* 46, 1009–1033.

Ren Z., Tang J., 2010, 3D direct current resistivity modeling with unstructured mesh by adaptive finite-element method, *Geophysics* 75, H7–H17.

Roach G.F., Green's functions (Cambridge University Press, Cambridge 2004).

Sasaki Y., 1994, 3D resistivity inversion using the finite-element method, *Geophysics* 59, 1839–1848.

Snyder D.D., 1976, A method for modeling the resistivity and IP response of two dimensional bodies, *Geophysics* 41, 997–1015.

Spitzer K., 1995, A 3D finite-difference algorithm for DC resistivity modeling using conjugate gradient methods, *Geophys*. *J. Inter*. 123, 903–914.

Strang, G., and Fix, G.J., An analysis of the finite element method (Prentice-Hall, Englewood Cliffs 1973).

Thomée V., Finite difference methods for linear parabolic equations, In Handbook of numerical analysis (ed. Ciarlet, P.G., and Lions, J.L.) (North-Holland Publishing Co., Amsterdam 1989) pp. 5–196.

Tsourlos P.I., Ogilvy R.D., 1999, An algorithm for the 3-D inversion of tomographic resisitivity and induced polarisation data: preliminary results, *J. Balkan Geophys. Soc.* 2, 30–45.

Wait R., Finite element methods for elliptic problems, In The state of the art in numerical analysis (ed. Jacobs, D.) (Academic Press, St. Louis 1977) pp. 883–914.

Wendland W.L., Strongly elliptic boundary integral equations, In The state of the art in numerical analysis (ed. Iserles, A., and Powell, M.J.D.) (Clarendon Press, Oxford 1987) pp. 511–562.

Zhdanov M.S., Fang S., 1996, Quasi-linear approximation in 3-D electromagnetic modeling, *Geophysics,* 61-3, 646-665.

Zhang J., Mackie R.L., Madden T.R., 1995, 3-D resistivity forward modeling and inversion using conjugate gradients, *Geophysics* 60, 1313–1325. $z = 0$

Dynamics of internal waves generated by mountain breeze in Alchichica Crater Lake, Mexico

Anatoliy Filonov[*], Iryna Tereshchenko, Javier Alcocer and Cesar Monzón

Resumen

Mediciones hidrofísicas realizadas en el lago cráter profundo Alchichica, México, mostraron la presencia de ondas internas intensas con período de un día, generadas por la influencia regular de la brisa de montaña. Las ondas diurnas generan ondas internas semidiurnas, las cuales tienen periodos cercanos a las oscilaciones de resonancia del lago. Las ondas internas rompen cerca de la orilla y en el fondo del lago, causando circulación baroclínica y mezcla de masas de agua. De acuerdo con los datos obtenidos con un ADCP, dos ondas inclinadas diurnas y dos semidiurnas se propagan en el lago unas hacia las otras en profundidad y pueden producir fluctuaciones de un modo vertical, cuando la profundidad del lago es un múltiplo de la semilongitud de onda vertical. Esta multiplicidad se aplica tanto a las ondas diurnas como a las semidiurnas. La existencia simultánea de modos horizontales y verticales corresponde a un modo volumétrico, o fluctuaciones resonantes de la laguna. Las ondas colapsan cerca del talud y del fondo del lago, induciendo circulación baroclínica y mezcla local.

Palabras clave: Lago Cráter Alchichica, Puebla, México, circulación de brisa de la montaña, generación de ondas internas, medidas hidrofísicas y meteorológicos, análisis espectral 3D.

Abstract

Hydrophysical measurements carried out in the deep tropical crater lake Alchichica, Mexico, showed the presence of intense internal waves with a one-day period, generated by the regular influence of a mountain breeze. The diurnal waves effectively generate semidiurnal internal waves that are close to the resonance oscillations of the lake. The internal waves brake close to the shoreline and into the lake's bottom, which generates baroclinic circulation and water masses mixing. According to the data obtained with a ADCP, two diurnal and two semidiurnal inclined waves propagate in the lake towards each other in depth and can form fluctuations of a vertical mode, if the depth of the lake is a multiple of one-half the vertical wavelength. This multiplicity applies to both the diurnal and semidiurnal waves. The simultaneous existence of horizontal and vertical modes corresponds to a volumetric mode, or resonant lake oscillation. The waves collapse near the shore slopes and the lake's bottom, inducing baroclinic circulation and local mixing.

Keywords: Crater Lake Alchichica, Puebla, Mexico, mountain breeze circulation, internal waves generation, hydrophysical and meteorological measurements, spectral 3D analysis.

A. Filonov
I. Tereshchenko
C. Monzón
Universidad de Guadalajara
Blvd. Marcelino García Barragán 1421
Esq. Calzada Olímpica, 44430
Guadalajara, Jalisco, México
*Corresponding author: afilonov@prodigy.net.mx
irina.tereschenko@cucei.udg.mx
rector.cucei@cucei.udg.mx

J. Alcocer
Proyecto de Investigación en Limnología Tropical
FES Iztacala
Universidad Nacional Autónoma de México
Av. de los Barrios No. 1, Los Reyes Iztacala
54090, Tlalnepantla
Estado de México, México
jalcocer@unam.mx

Introduction

Internal oscillations in density stratified lakes depend on the lake shape, the bottom relief and the wind force which causes these oscillations. In large lakes the sporadic wind force creates nonlinear asymmetric internal waves which propagate in lake (Farmer, 1978). In circular lakes, the pulsating wind forces internal seiches with a horizontal modal structure (MacIntyre and Flynn, 1999; Csanady, 1973). Above the sloping bottom internal Kelvin waves or the Poincaré waves can be formed (Antenucci et al., 2000; Saggio, Imberger 1998). The periodic wind generates internal waves that give rise to nonlinear harmonics and a wide spectrum of internal waves (Monismith, 1985; MacIntyre and Flynn, 1999). The presence of internal waves has been reported in Lake Alchichica (Filonov and Alcocer, 2002).

Though wind-forced motions in stratified lakes near sea level have been previously studied and modeled (Monismith, 1985; Imberger, 1985), there have been few investigations of lakes in volcanic craters located in high altitude tropical zones. Research of the physical processes associated with mountain breezes has been discussed in relation to Santa Maria del Oro (Serrano et al., 2002), volcanic Mexican lake situated at a height of 1500 m above sea level.

The objective of the present study was to provide physical experimental evidence on the causes and dynamics of the internal waves generated in Lake Alchichica by mountain breezes.

Study area

Lake Alchichica is a typical saline crater lake of the Mexican plateau, with circular shape, steep coastal slopes, more than 1.5 km diameter and 60 m depth (Figure 1a). Alchichica is one of the deepest natural lake in Mexico. It is located at an elevation of 2350 m above sea level. Its coordinates are 19° 24.7'N and 97° 24.0'W. Alchichica has an area of 2.3 km^2 with a volume of 94,214,000 m^3 and an average depth of 40.9 m (Filonov et al., 2006). The water has a salinity of 8.5 g/L and a pH 8.7-9.2, dominated by sodium-magnesium and chloride-bicarbonate ions. Water salinity varies little with depth. Annual air temperature fluctuates from −5.5 to 30 °C with a mean value of 14.4 °C (Filonov and Alcocer, 2002). An arid climate, with an annual precipitation regime of less than 500 mm and an annual evaporation rate of 1690 mm characterizes the area. Alchichica is warm-monomictic (monomictic lakes are lakes that mix from top to bottom during one mixing period each year). Mixing takes place from late December to early March, during the cold, dry season, and it remains stratified throughout the rest of the year (from late March to early December) during the warm, rainy season (Alcocer et al. 2000). The lake's diameter is less than the internal Rossby radius (7.3 km), so the influence of the Earth's rotation is negligible.

Hydrographic and meteorological measurements

The experiment at the lake was carried out from May 8 till May 11, 2004. Temperature fluctuations were measured by three mooring instruments (Figure 1). Buoy 1 was equipped with a temperature meter TDS-85 (made by UABC, Mexico) at horizon 8 m, with a measuring precision of 0.02°C. The buoy 2 was equipped with a conductivity-temperature-depth (CTD) meter SBE-16 (made by Sea-Bird Electronics) at horizon 12.5. The buoy 3 was equipped with a chain of Waterpro thermistors (Onset Computers Corp., Massachusetts, USA) deployed at depths of 1, 5, 10, 15, 20 and 25 m with a 0.2°C resolution. On this mooring temperature was measured hourly during 3 month (from March 24 to May 20, 2002).

Five temperature surveys were made on a line between moorings, approximately at 30 degree angle from the average wind direction (Figure 1). Each survey lasted about one hour. During a survey a CTD profiler SBE-19 fell manually from the boat with a speed of about 1 m/s and a 0.5 seconds sampling rate. A Global Position System (GPS) fixed the coordinates of the sounding points.

An Acoustic Doppler Current Profiler (600 kHz ADCP, RD-Instruments) was placed at the bottom. During 2.6 days, it measured the vertical profile of three current speed components with a vertical resolution of 1 m (Figure 1). The sampling rate was 0.5 minutes. The speed's time series were smoothed out with an interval 2.5 hrs.

Meteorological measurements were hourly conducted on the lake from January 2003 to December 2004, using Davis GroWeather automatic weather station mounted at a height of 4 m on the east coast of the lake.

The acquired data were analyzed using unified standard methods and spectral analysis techniques (Jenkins and Watts, 1968). To calculate two-dimensional spectra for temperature, wind and water current fluctuations, we followed the methods described in Konyaev (1990).
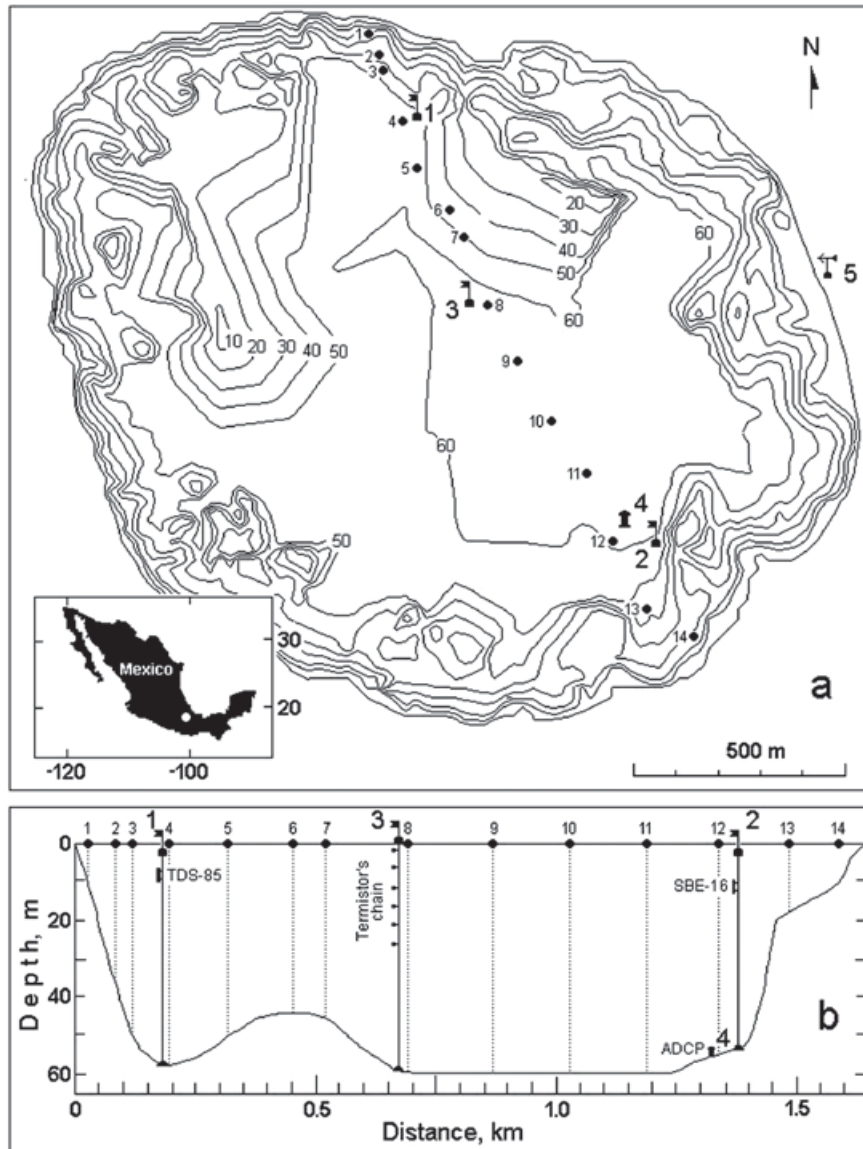
Figure 1. a) The bottom's relief and the instruments' position in lake. The large numbers show the position of buoys 1, 2 and 3; the ADCP (4) and the meteorological station (5). Circles with small numbers show the casts' position during the fourth survey 10.05.2004 from 14:14 until 15:02. b) The bottom profile on the line of CTD casts and the position of devices in the water column.

For calculation of vertical deviations of the water layers on data of temperature sections the following algorithm was used (Filonov and Konyaev, 2003): all vertical temperature-pressure profiles $T_j(p_j)$ are interpolated onto a single depth grid $T_j(z)$ and the mean temperature profile is computed as: $T(z) = \dfrac{1}{J}\sum_j T_j(z)$ where $j = 1{:}J$ is the profile index. The mean profile $T_j(z)$ describes the unperturbed position of water layers. The inverse functions $z_j(T)$ and $z(T)$ exist if the original profiles $T_j(z)$ and the mean profile $T(z)$ are monotone functions as it is in our case.

Vertical deviations of water layers from the unperturbed position are defined as $\Delta h_j(z) = z(T) - z_j(T)$. Next, temperature is replaced with depth by means of the mean profile $z(T)$ to give the relationship between deviation and depth $\Delta h_j(z)$. The layers' position is then obtained as $h_j(z) = z - \Delta h_j(z)$.

Each sounding consists of two temperature profiles $T_{dj}(z)$ and $T_{uj}(z)$, which correspond to the descending and ascending track of the profiler respectively. The difference between these profiles $dh_j(T) = z_{uj}(T) - z_{dj}(T)$ is accounted for by rapid (small-scale) disturbances of water layers. Temperature T is then replaced with

depth z with the use of the mean profile $z(T)$ to give the $dh_j(z)$ difference. It is then normalized by $\Delta t_j(z)$, which is the time interval between the observations made on downward and upward sounding profiles: $w_j(z) = dh_j(z)/\Delta t_j(z)$. The normalized difference has the units of velocity. However, this vertical velocity is accounted for not only by the vertical motion of layers but by their horizontal advection as well.

The geographical coordinates are transformed to along-leg coordinate x, which is assigned to each profile. In this way, three vertical-cross sections are generated: the layers' position $h(x, z)$, their deviation $\Delta h_j(x, z)$ and vertical velocity $w(x, z)$.

Results

Mountain breeze circulation

Analysis of a two-year series of meteorological observations at the lake showed that the presence of mountain winds is relatively constant from day to day in the area of the lake. Lake Alchichica lies in a volcanic crater in the mouth of a wide mountain valley that extends north to south with slopes as high as 300-500 m. To the north, there is an extensive saline plain spanning nearly 200 km^2. These topographic features provide suitable conditions for local atmospheric circulation between the mountain and the saline valley over the entire length of the lake.

During the day, temperature differences between the saline valley and the main zone create a reverse pressure gradient. As a result, the wind is directed upwards along the main

slopes from the north. The daily course of the wind over the lake dictates daily fluctuations in the air temperature and atmospheric pressure (Figure 2 a, b).

From 22:00 until 13:00 hours, the weak wind above the lake does not exceed 1 m/s. Its speed grows quickly during the afternoon and reaches an average hourly speed of 5-6 m/s with pulses up to 10-12 m/s at approximately 17:00 hours (see in the upper right corner of the. As of 22:00 hours, the wind begins to rapidly return back to nocturnal normal values. The wind's direction throughout the day varies insignificantly and remains within the N-NNO range, and presents a non-daily clockwise rotation, typical for a sea breeze or for a breeze on such large Mexican lakes such as Chapala (Filonov, 2002).

Stratification

Long-term measurement of the thermistor chain in the center of the lake (mooring 3) showed that due to the considerable water transparency (euphotic zone 14-38 m) and the action of wind and internal waves, daily solar warming penetrates to a depth of about 10 m. The total heat influx is small as the rapid increase in temperature of the top layer in the first half of the day is offset by a similarly swift downturn in the second half of the day. Wide variability in daily air temperature is important for heat absorption and emission in a high-mountain tropical plateau. Wind waves on the lake are small (length 5-7 m and height less than 0.5 m) and they create a mixing that does not likely penetrate deeper than a few meters. At midday, the surface temperature decreases slightly with the onset of the breeze.
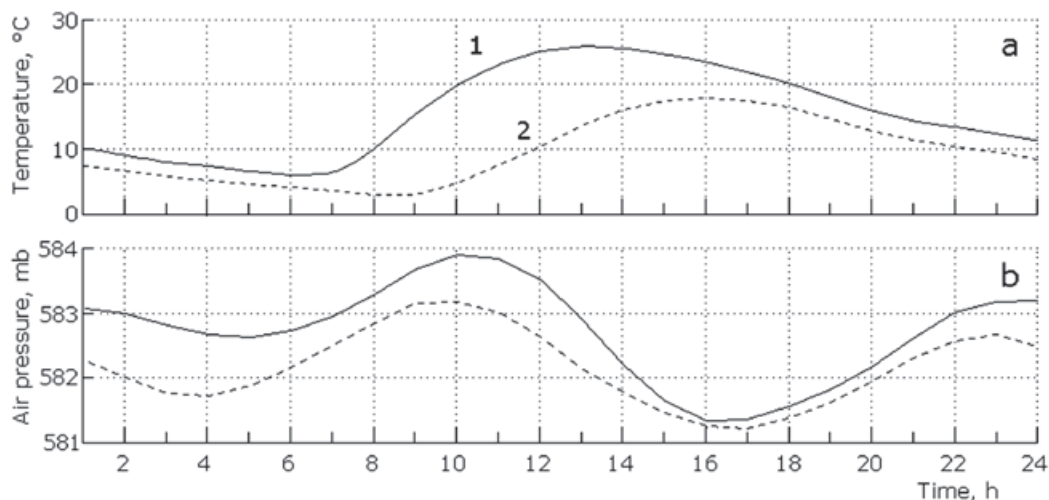
Figure 2. a) Hourly average fluctuation of air temperature, b) atmospheric pressure for the dry (1) and wet (2) seasons in a year.

During our experiment the density stratification of the lake was defined by the temperature decrease with depth from 19.5°C on the surface to up to 14.7°C near the bottom. Salinity decreased insignificantly from 7.58 psu at the surface to 7.52 psu on the bottom (Figure 3). Thus, vertical change in water density is completely determined by temperature. The thermocline with the maximal buoyancy frequency $N(z) = [(g/\rho) \cdot (\partial \rho / \partial z)]^{1/2}$ of 20 cycle/h, settles down between horizons 10 and 18 m. The buoyancy frequency in the deep layers is decreased to 1 cycle/h.
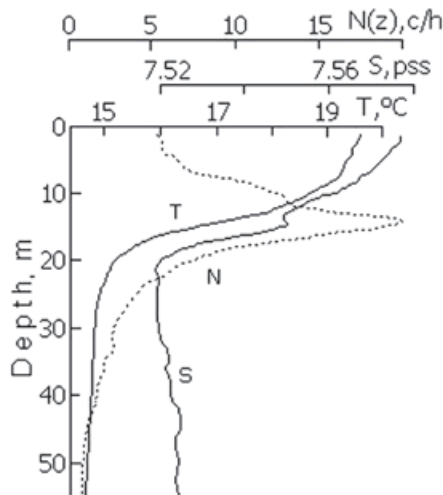
Figure 3. a) Mean vertical profiles of temperature, salinity and buoyancy frequency (data from five repetitive cuts, just 48 casts).

Temperature fluctuations in two separate points (moorings 1 and 2)

Despite the difference in depth of the devices, the average temperature measured by both of them was identical and equal to 18.9°C. Hence, on average, under action of the wind, the thermocline is tilted. In the lake's northern part (mooring 1) the thermocline is raised with respect to the southern part (mooring 2) around 4.5 m. The towing of the temperature gauge on a line between moorings has shown, during the maximal wind speed (after midday), that the water temperature at a depth of 0.2 m increases monotonously from 19.3°C near mooring 1 to up to 20.2°C near mooring 2.

The fluctuations in the water layers at the moorings have large amplitude and complex form with the predominance of diurnal and semidiurnal oscillations. There are high short bursts and groups of bursts with a height of up to 3 m (Figure 4). On the basis of the temperature fluctuations at each mooring and the average temperature profile, the vertical water layer deviations were determined at the depths where the thermographs were deployed. The structure of the deviation spectra was similar at the two moorings (Figure 5). The greatest peak is on the semidiurnal frequency. Another peak of almost the same height is on the diurnal frequency.

From here and subsequently, the spectrum is calculated as the module of a Fourier transformation without squares it. Thus, spectral
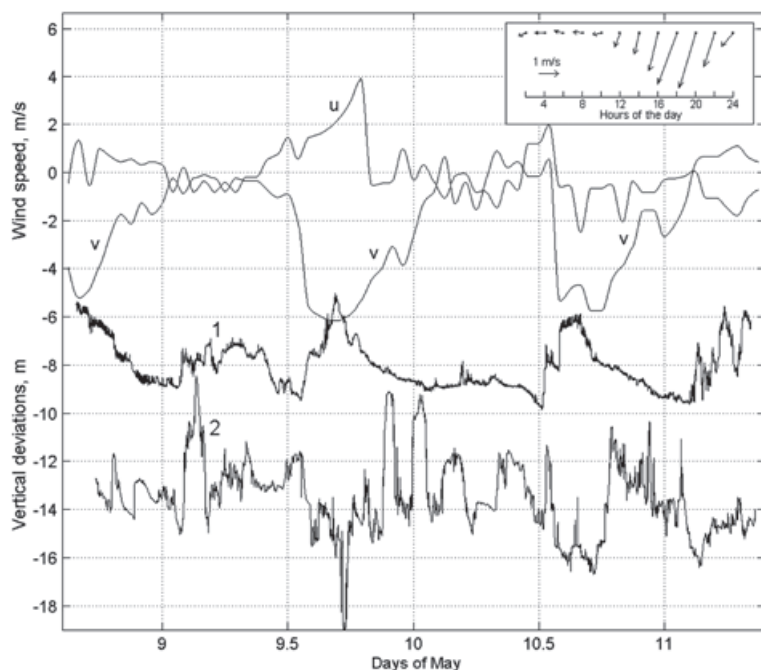
Figure 4. Horizontal wind speed components and vertical deviations of water layers at mooring 1 (horizon 8 m) and mooring 2 (horizon 12.5 m). The numbers of the curves correspond to the buoys 1 and 2. Daily average wind velocity from January to May 2002 in Lake Alchichica is presented in the rectangle in the superior right corner.

density in the spectrum peaks is numerically equal to the amplitude of fluctuations on the appropriate frequencies, and it is possible to present the axis of spectral density in the same units in which the time series is measured (Figure 5).

The diurnal oscillations alone are dominant in the correlation function between vertical deviations of water layers under the buoys and the v-component (northern component) of the wind. The correlation between vertical deviations and the u-component (eastern component) of the wind is relatively small. Hence, the diurnal internal waves are created by the wind, which direction coincides with the axis v.

As shown by the correlation analysis, the oscillations on the two buoys are in an opposite phase as it occurs in oscillations with horizontal mode. It is possible to assume that between the two moorings only half of the diurnal wavelength settles down (first horizontal mode with antinodes of vertical deviations and nodes of horizontal orbital speed at opposite sides of the lake).

Oscillations of water layers on a line survey

Five temperature surveys were made on a line between moorings. They were performed every day in the middle of the day. The survey's data processing consisted of a number of procedures:

- Elimination of inversions in temperature and salinity profiles;
- Interpolation of the data in a uniform scale of depth;
- Calculation of mean vertical profiles of temperature, salinity, density and buoyancy frequency;
- WKB - normalization of the temperature profiles (Filonov and Lavin, 2003);
- Transition from temperature to pressure profiles by means of an average temperature profile;
- Calculation of pressure deviations (vertical deviations of the water layers).

The detailed description of these procedures can be found in (Filonov and Konyaev, 2003).

Vertical deviations of the water layers form the two-dimensional field on a depth-horizontal plane. This field has periodicity, which precisely comes to light by means of a two-dimensional (vertical and horizontal wave numbers) deviations' spectrum (Figure 6). The maximum positive deviation on one end of the survey is accompanied by the maximum negative deviation on the other end.

The spectrum contains two basic peaks with different vertical wave number. The estimations of the horizontal wavelengths spectrum present two peaks at 1.3 and 1.5 km for survey 3 and at 1.1 and 1.8 km in average for all four surveys. The systematic difference in the measured wavelengths could arise as a result of the Doppler's effect at the survey. The difference of the measured horizontal wave numbers, when the diurnal or semidiurnal waves ($f = 1$ or 2 cycle/day) move towards each other and the boat speed of $V = 1$ km/h, is equal to $\Delta kx = 2f / V = 0.08$ or 0.16 cycle/km, that is close to the observable shift (Figure 6). Hence, the waves move horizontally towards each other and form a horizontal mode of oscillations.
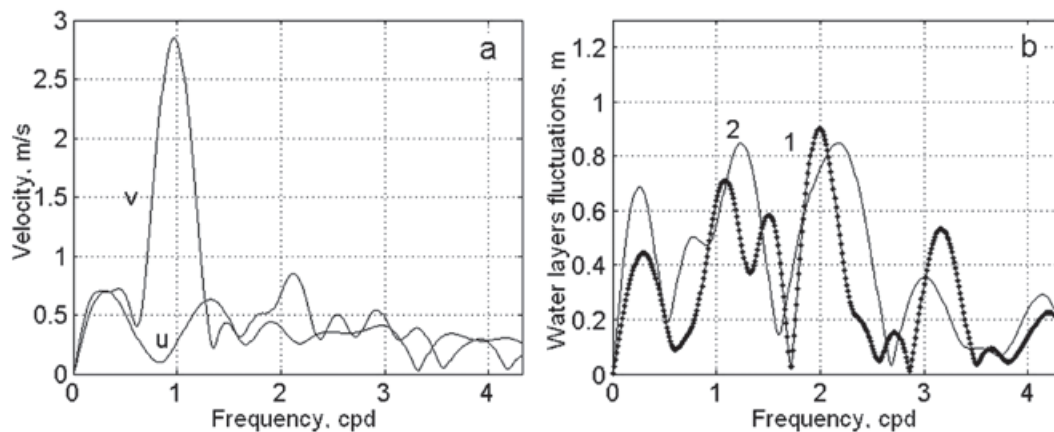
Figure 5. Spectra of the wind speed components (a) and water layers fluctuations near buoy 1 and 2 (b). The spectral density of the peaks is numerically equal to the oscillations' amplitude with the appropriate frequency.
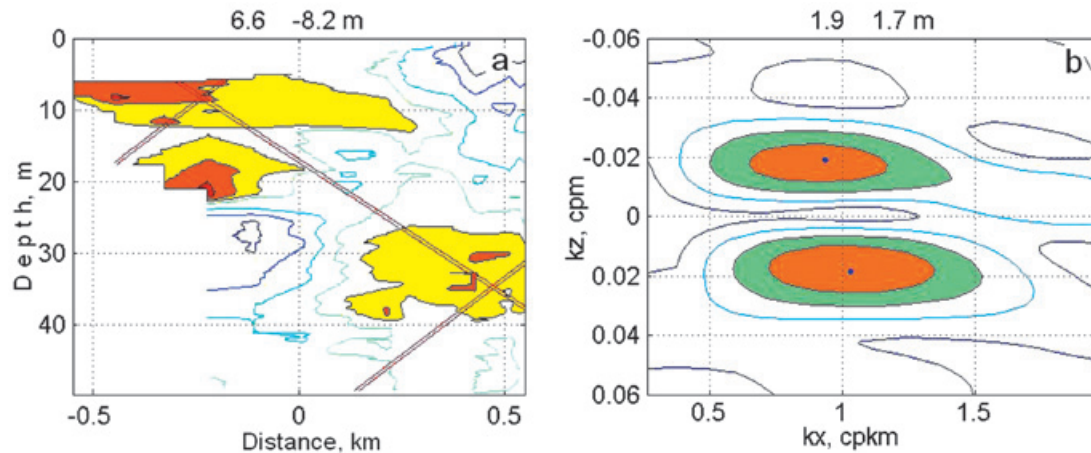
Figure 6. Deviations of water layers on the data of fourth survey (a) and two-dimensional spectra of these deviations (b). The axis x is directed from mooring 1 to 3. The straight lines show crests of two waves corresponding to the basic peaks of the spectra (b). Above the figures the maximum and minimum deviations (a) and the amplitude of the basic fluctuations (b) are showed. Isolines on Figure (a) are plotted with a 0.3 step from a maximum. Here, the levels above 0.3 are shaded. Isolines on Figure (b) Isolines are plotted with a 0.2 step from a maximum; the levels above 0.6 are shaded.

In the ocean there is usually a vertical mode of internal waves formed as a result of the reflection of waves from the bottom and the surface. In our case, a horizontal mode can be formed by reflection from the sloping shores, whose inclination considerably exceeds the inclination of the internal waves.

Current speed

The speeds' field is transformed to depth-constant buoyancy frequency (WKB-normalization) maintaining the thickness of the observed water layer. After the WKB-normalization, the internal waves' beams and crests become rectilinear, and the basic spectrum peaks become more compact (Filonov and Lavin, 2003).

The normalized field is subjected to further analysis. Previously, the average values of the current speed are removed from the current's time series components on each horizon. The field of the horizontal u-component of the speed vector on a depth-time plane contains a characteristic interference structure (the u-component is directed towards the east, v - towards the north) (Figure 7a). The crest's inclination determines the vertical phase speed of the diurnal and semidiurnal waves, which is equal to 0.055 and 0.075 cm/s. Tilting diurnal wave crests on the vertical-horizontal plane by the temperature recording is 2.3 degrees, so that the horizontal diurnal wave phase velocity is 1.4 cm/s.

In a spectrum of the u-component there are two peaks with a diurnal frequency and two with semidiurnal frequency (Figure 7b). Each pair of peaks corresponds to two inclined waves on a depth-time plane. The waves propagate in opposite directions on depth. More intensive waves propagate downwards (group movement), less intensive - upwards. Oscillations of the v-component of the speed are significantly less intensive, so the orbital movements in the waves occur on the strongly extended orbits on a west-east direction.

Trajectories of beams

It is convenient to treat the inclined wave in the terms of beams, or characteristics. The beam's angle of inclination is defined by the buoyancy frequency $N(z)$, the inertial frequency $F = 0.66$ cycle/day and the wave frequency f: $\alpha(z) = arctg(f^2 - F^2)/(N(z)^2)f^2)^{1/2}$. The trajectory of a beam comes out by integrating on depth $x(z) = x_0 \pm \int_0^z ctg(\alpha(z))\, dz$, where x_0 defines the beam's location on the x axis. The crests and troughs of a wave extend along the beam; the group velocity is directed along the beam.

Taking a vertical section of the lake, on a line from west to east, two characteristics for the diurnal and semidiurnal waves were calculated (Figure 8). Two and a half vertical lengths of a diurnal wave and one length of a semidiurnal wave fit from the surface of the lake to the bottom. Steep side slopes and a practically flat bottom create conditions for the arising of resonance for internal waves.
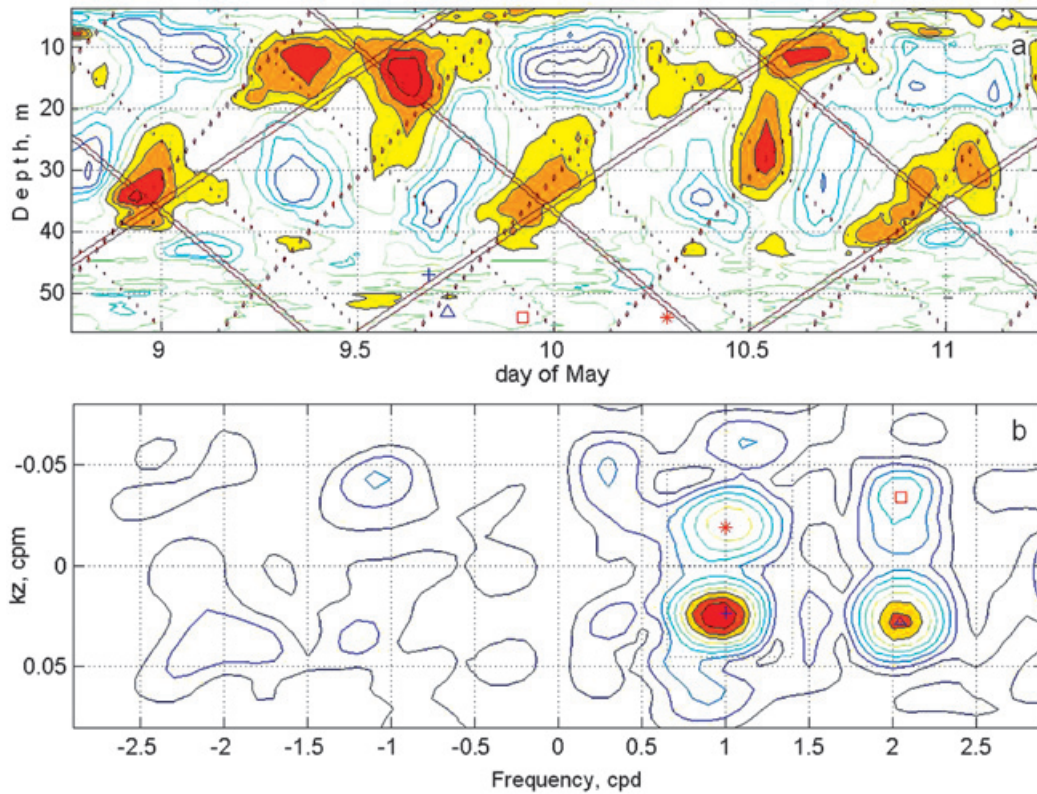
Figure 7. a) A u-component of current speed after WKB-normalization and crests of diurnal and semidiurnal waves propagate in opposite directions on depth (inclined lines). Isolines are plotted with a step 0.2 from a maximum, the positive deviations are shaded. b) The spectra of the u-component (positive semi axis of frequency) and v-component of the speed (negative semi axis). Isolines are plotted with a step 0.1 from a maximum; the levels above 0.7 are shaded. The waves moving up marked by symbols ✳□ and by symbols +△ - moving down.
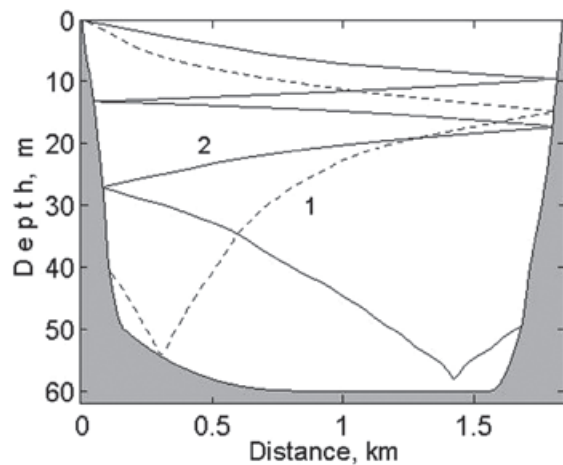
Figure 8. The characteristics beam of diurnal (1) and semidiurnal (2) internal waves.

Discussion

The mountain breeze, which blows with diurnal periodicity, serves as the causing force and as the source of energy for all movements in the lake. In the afternoon the wind drives warm water on the surface to one of the lake's edges. The movements in a thin top layer of the lake serve as a wave generator, creating an internal wave with a diurnal period.

On the data obtain with the mooring instruments, vertical fluctuations of temperature at opposite edges of the lake are in an opposite phase, so two waves form horizontal mode with antinodes of vertical fluctuations at opposite edges of lake (Figure 7). The waves' horizontal length is approximately equal to twice the lake's diameter.

From the ADCP's data, we found that both diurnal and semidiurnal oscillations are formed by two inclined waves (four waves in all). Pair of inclined waves moves towards each other, on depth. On the temperature survey data (taking into account the Doppler Effect) only two inclined internal waves move towards each other on a horizontal plane.

It is possible that diurnal and semidiurnal waves are not determined by the survey because they might have a different orientation relative to the survey line.

Diurnal oscillations are forced ones; their horizontal wavelength is imposed by the lake's diameter. Semidiurnal oscillations arise originally as a result of nonlinear distortions of large diurnal oscillations. However, the amplitude of the semidiurnal oscillations ranges up and even exceeds the amplitude of the diurnal ones. This can be a result of the proximity between semidiurnal oscillations and resonance ones in the lake.

Conclusion

Solar warming creates and supports steady density stratification in the lake. The daily change in temperature in the top water layer is very large, but the daytime heat influx is compensated, to a great extent, by its loss at night. The stratification interferes with a vertical exchange inside the lake. In the afternoon, the wind drives warm water on the lake surface, causing an inclination of the thermocline. Water surge on the surface is created by friction forces. The mountain breeze blows over Lake Alchichica with diurnal periodicity and generates diurnal internal waves with large amplitude. The second harmonic of the diurnal oscillations arises due to nonlinear distortions of the diurnal oscillations and reaches large amplitude presumably because semidiurnal frequency is close to the lake's resonance one. The internal waves partially break especially near the coastal slopes in the thermocline's area, providing local mixing of the lake's waters.

The water volume of the lake Alchichica looks like a vertical cylinder that allows the occurrence of both horizontal and vertical modes of internal waves and, as a result, cavity resonator for the waves. As far as we know the cavity resonance of internal waves in a natural basin was first observed. The generation mechanism of semidiurnal internal waves by forcing of the diurnal frequency is new for natural hydrophysical objects. It seems likely that the discovered effects are rare for the natural basins as their water volumes have irregular forms. In this regard the interesting exceptions may be among the volcanic lakes of Mexico.

Acknowledgements

References

Alcocer J., Lugo A., Escobar E., Sanchez M.R., Vilaclara G., 2000, Water column stratification and its implications in the tropical warm monomictic Lake Alchichica, Puebla, Mexico. *Verh. Internat. Verein. Limnol.*, 27, 3166-3169.

Antenucci J., Imberger J., Saggio A., 2000, Seasonal Evolution of the Basin-Scale Internal Wave Field in a Stratified Lake. *Limn. Oceanogr.*, 45, 1621-1638.

Imberger J., 1985, The diurnal mixed layer. *Limn. Oceanogr.*, 30, 737-770.

Farmer D.M., 1978, Observations of long nonlinear internal waves in a lake. *J. Physical Oceanography*, 8, 63-73.

Emery W.J., Thomson R.E., 1997, Data analysis methods in physical oceanography, Pergamon, 634 pp.

Filonov A.E., 2002, On the Dynamical Response of Lake Chapala, Mexico to Lake Breeze Forcing, *Hidrobiología*, 467, 141-157.

Filonov A.E., Konyaev K.V., 2003, Nonlinear internal waves near Mexico's central Pacific coast, p.p. 257-274. In O.U. Velasco Fuentes, J. Sheinbaum and J. Ochoa [eds.], Nonlinear processes in geophysical fluid dynamics. Kluwer Academic Publishers, 376 pp.

Filonov A.E., Lavin M.F., 2003, Internal tides in the Northern Gulf of California. *J. Geophys. Res.,* 108, 2156-2202.

Filonov A., Tereshchenko I., Alcocer J., 2006, Dynamic response to mountain breeze circulation in Alchichica, a crater lake in Mexico. *Geophys. Res. Lett.*, 33, L07404,:10.1029/2006GL025901,

Jenkins G.M., Watts D.G., 1968, Spectral analysis and its applications. Holden-Day, 525 pp.

Konyaev K.V., 1990, Spectral Analysis of Physical Oceanographic Data. A.A. BALKEMA, Rotterdam, 200 pp.

Konyaev K.V., Sabinin K.D, 1992, Waves inside the Ocean. Gidrometeoizdat, St-Peterburg, 199, 272 pp.

MacIntyre S., Flynn K.M., 1999, Boundary Mixing and Nutrient Fluxes in Mono Lake, California, Limnology and Oceanography. 44, 512-529.

Monismith S.G, 1985, Wind-forced motions in stratified lakes and their effect on mixing-layer shear, *Limn. Oceanogr.*, 30, 771-783.

Saggio A., Imberger J., 1998, Internal Wave Weather in a Stratified Lake. *Limn. Oceanogr*, 43, 1780-1795.

Serrano D., Filonov A., Tereshchenko I., 2002, Dynamics response to valley breeze circulation in Santa Maria del Oro, a volcanic lake in Mexico. *Geophys. Res. Lett.*, 29, 27-1, 27-4.

Csanady G.T., 1973, Transverse Internal Seiches in Large Oblong Lakes and Marginal Seas. *J. Physical Oceanography*, 3, 4, 439-447.

Thorpe S.A., 1998, Some Dynamical Effects of Internal Waves and the Sloping Sides of Lakes, in Physical Processes in Lakes and Oceans. Coastal and Estuarine Studies, 54, 441-460.

Forward modeling of gravitational fields on hybrid multi-threaded cluster

Carlos Couder-Castañeda*, José Carlos Ortiz-Alemán, Mauricio Gabriel Orozco-del-Castillo and Mauricio Nava-Flores

Resumen

La solución analítica de las componentes del tensor gravimétrico, utilizando la ecuación del potencial gravitacional para un ensamble volumétrico compuesto de prismas de densidad constante, requiere un alto costo computacional. Esto se debe a que el potencial gravitacional de cada uno de estos prismas tiene que ser calculado para todos los puntos de una malla de observación previamente definida, lo cual resulta en una carga computacional de gran escala. En este trabajo introducimos un diseño híbrido y su implementación paralela basada en OpenMP y MPI, para el cálculo de las componentes vectoriales del campo gravimétrico (G_x, G_y, G_z) y las componentes del tensor gravimétrico (G_{xx}, G_{xy}, G_{xz}, G_{yy}, G_{yz}, G_{zz}). El rendimiento obtenido conlleva a óptimas relaciones del speed-up, ya que el tiempo de cómputo es drásticamente reducido. La técnica de paralelización aplicada consiste en descomponer el problema en grupos de prismas y utilizar diferentes espacios de memoria por núcleo de procesamiento, con el fin de evitar los problemas de cuello de botella cuando se accesa a la memoria compartida de un nodo del cluster, que se producen generalmente cuando varios hilos de ejecución acceden a la misma región en OpenMP. Debido a que OpenMP solo puede utilizarse en sistemas de memoria compartida es necesario utilizar MPI para la distribución del cálculo entre los nodos del cluster, dando como resultado un código híbrido OpenMP+MPI altamente eficiente con un speed-up prácticamente perfecto. Adicionalmente los resultados numéricos fueron validados con respecto a su contraparte secuencial.

Palabras clave: gravedad, gradiometría, OpenMP, MPI, hyper-threading, clusters.

Abstract

The analytic solution of the gravimetric tensor components, making use of the gravitational potential equation for a three-dimensional volumetric assembly composed of unit prisms of constant density, demands a high computational cost. This is due to the gravitational potential of each one of these prisms must be calculated for all of the points of a previously defined observation grid, which turns out in a large scale computational cost. In this work we introduce a hybrid design and its parallel implementation, based on OpenMP and MPI, for the calculation of the vectorial components of the gravimetric field and the components of the gravimetric tensor. Since the computing time is drastically reduced, the obtained performance leads close to optimal speed-up ratios. The applied parallelization technique consists of decomposing the problem into groups of prisms and using different memory allocations per processing core to avoid bottleneck issues when accessing the main memory in one cluster node, which are generally produced when using too many execution threads over the same region in OpenMP. Due OpenMP can be only used on shared memory systems is necessary to use MPI for the calculation distribution among cluster nodes, giving as a result a hybrid code (OpenMP+MPI) highly efficient and with a nearly perfect speed-up. Additionally the numerical results were validated with respect to its sequential counterpart.

Keywords: gravity, gradiometry, OpenMP, MPI, hyper-threading, clusters.

C. Couder-Castañeda*
J. C. Ortiz-Alemán
M. Gabriel Orozco-del-Castillo
Mexican Petroleum Institute
Eje Central Lázaro Cárdenas, 152
San Bartolo Atepehuacan, Gustavo A. Madero
07730, Ciudad de México
*Corresponding author: ccouder@esfm.ipn.mx

M. Nava Flores
División de Ingeniería en Ciencias de la Tierra
Facultad de Ingeniería
Universidad Nacional Autónoma de México
Ciudad Universitaria
Delegación Coyoacán, 04510
México D.F., México

Introduction

The shared memory architecture is becoming more common every day in the high-performance computing market. With the hardware technology advances allowing us to have a great number of cores with access to the same memory locations, nowadays it is not that expensive to have systems with forty or sixty cores using shared memory. OpenMP is now a standard for symmetric multiprocessing systems (SMP) (even can be used transparently in the Xeon Phi architecture (Calvin *et al.*, 2013)) sustained by a combination of function and compiler directives, a standard for the symmetric multiprocessing (SMP) systems (Dagum and Menon, 1998; Curtis-Maury *et al.*, 2008). OpenMP has proven to be a powerful tool for SMP due to several reasons: it is highly portable; it allows fine and medium granularity, each thread can access to the same global memory; and has their own private memory, and it also has a greater level of abstraction than MPI model (Brunst and Mohr, 2008).

MPI is a library supported on the Same Program Multiple Data (SPMD) model and on the message passing model, with an explicit control of the parallelism. The processes can only read and write in their respective local memories and the data in these memories is transferred through calls to functions or procedures which implement the message passing model. Among the principal characteristics of MPI are that it can run in architectures of shared and distributed memory, is convenient for medium to coarse granularity and that employment is widely extended, making it extremely portable among platforms (Krpic *et al.*, 2012).

Using a hybrid programming model we can take advantage of the benefits of two programming models OpenMP and MPI. MPI is normally used to control the parallelism among cluster nodes, while OpenMP is applied in the creation of threads of fine granularity tasks within each node. Most applications developed in hybrid model involves a hierarchical model: MPI is for the higher level and OpenMP for the lower one (Smith, 2000).

One of the potential benefits of using hybrid model programming consists of getting rid of the barrier of scaling that each model has. Generally, in MPI the scaling is limited by the communications cost, because an application is affected by the overload of communication when the number of processes is increased. In OpenMP the performance of an application is affected by cache coherence problems and access to shared memory

which may lead to bottleneck issues between the execution threads when trying to access memory. By mixing these methodologies of parallel programming (OpenMP and MPI), we can obtain a more diverse granularity of the application and therefore a better performance than by using each one on its own.

There are different applications which use this programming paradigm: OpenMP with MPI. For example, in the solution of sparse linear systems (Mitin *et al.*, 2012), in graph-coloring algorithms (Sariyuce *et al.*, 2012), in some models of fluid dynamics (Amritkar *et al.*, 2012; Couder-Castañeda, 2009) and finite element methods (Boehmer *et al.*, 2012), in the simulation of turbulent fluids (Jagannathan and Donzis, 2012), even in the simulation of combustion chambers (Környei, 2012) and the implementation of neural networks (Gonzalez *et al.*, 2012). As can be observed, there are numerous computational implementations using OpenMP with MPI, nevertheless, this type of design is supported on a natural decomposition of the domain (Carrillo-Ledesma *et al.*, 2013), based on data. For our particular problem, each one of the processing units accesses all of the computational domain points.

In Figure 1 is depicted a domain decomposition, where each task (process or thread) is given some data subset on which to work. This domain decomposition is commonly used for example in finite differences problems where computational domains divided disjointly among the different tasks.

On the other hand, in the direct conformation of gravimetric data, an initial model for the source body is constructed from geological-geophysical information. The anomaly of such model is calculated and compared to the observed anomaly, after which the parameters are adapted to improve the adjustment between them. These three steps that arrange the model properties — *anomalies calculation, comparison* and *adjustment* — are repeated up to the observed and calculated anomalies are similar enough.

A mass volume can be approximated by a set of rectangular prisms; if chosen sufficiently small, each prism can be considered to have a constant density. Because of the superposition principle, the gravitational anomaly of a body can be approximated at anypoint by summing the effects of all the prisms over that point. Even though this methodology appears simple (by reducing the size of the prisms to better adjust the source body),

Figure 1. The domain decomposition based on data for an OpenMP+MPI application.
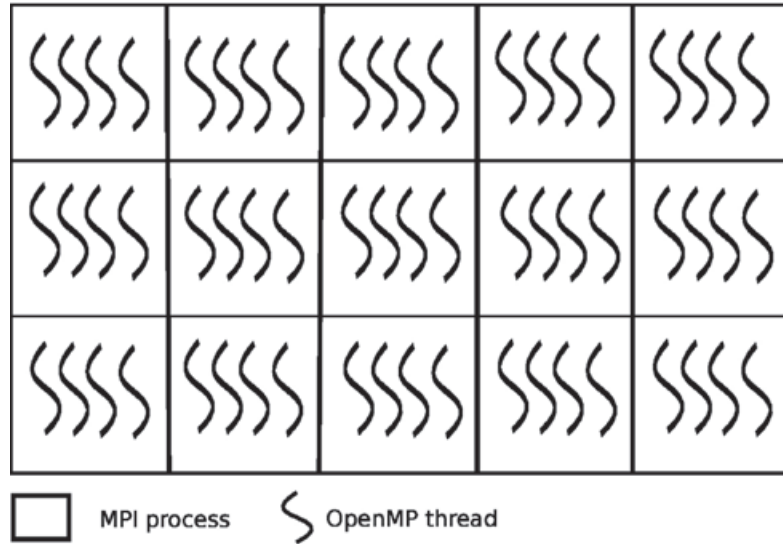
computing time is considerably increased. There are other approaching methods of the gravitational anomaly that can simplify the required computation (mass points or tesseroids approximations), however, they may complicate the construction of the geological model (Heck and Seitz, 2007).

Application design

The application consists of calculating the gravimetric anomaly produced by a rectangular prismatic body with constant density with respect to a group of observation points (see Figure 2). The set of prisms is known as an ensemble of prisms, which is not necessarily regular. A set of irregular prisms can be configured as long as the prisms are not superimposed. Because the gravitational field complies with the superposition principle with respect to the observation points, if f is the calculated response at a point (x, y), then the observed response at the point $f(x, y)$ is given by:

$$f(x,y) = \sum_{k=1}^{M} G(\rho_k, x, y) \qquad (1)$$

where M is the number of total prisms and ρ is the density of the prism.

It is well known that the function that calculates the anomaly for a given prism from an observation point is written as follows (Nagy *et al.*, 2000):

$$g = f(x_l, y_l, z_l, x_r, y_r, z_r, x_p, y_p, z_p, \rho) \quad (2)$$

where (x_l, y_l, z_l) is the top left vertex of the prism, (x_r, y_r, z_r) is the bottom right prism and (x_p, y_p, z_p) is the observation point and ρ the density, as shown in Figure 3.
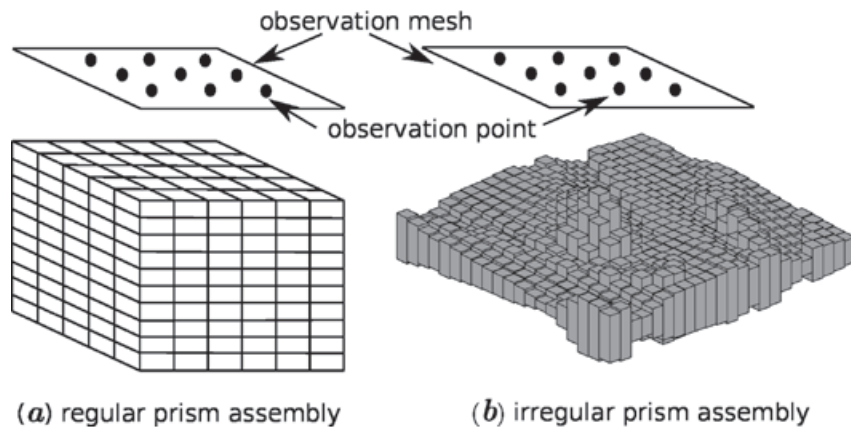

Figure 2. Decomposition of the calculation of M prisms with respect to the observation grid: (a) regular prism assembly, (b) irregular prism assembly.

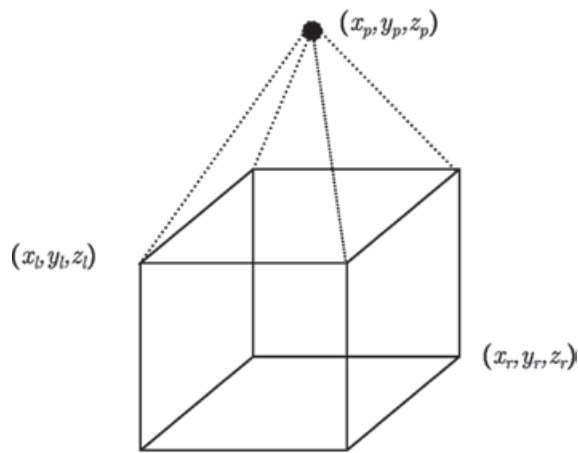(a) regular prism assembly (b) irregular prism assembly

Figure 3. Calculation of a prism with respect to a point of observation.

The aforementioned is a large scale problem since, for example, a synthetic problem conformed by a set of prisms of $300 \times 300 \times 150 = 13,500,000$ elements, against an observation grid of $100 \times 100 = 10,000$ points, results in the calculation of $135,000,000,000$ integrals or differentials to solve the entire problem. The formulations we used are included in appendix A.

Computing time reduction in a numerical simulation is of great importance to diminish research costs. A simulation which lasts a week is likely to be costly, not only because the machine time is expensive, but also because it prohibits the quick acquisition of results to make modifications and predictions.

In many projects to be parallelized, several times the serial algorithm does not show a natural decomposition which allows easily porting it to a parallel environment, or the trivial decomposition does not yield good performance results. For such reasons it is convenient to use a hybrid programming methodology, as the one developed and presented in this paper. This methodology provides an adequate programming design to obtain a superior performance.

To develop a parallel program it is fundamental to search for the finest granularity, as in the methodology proposed by Foster (Foster, 1995). In this case it is possible to parallelize by prisms or by observation points. One of the requirements of the design is that it must be scalable, therefore the use of hybrid systems is quite appropriate; these systems are the most commonly used nowadays. Following Foster's methodology, it is necessary to begin with the finest granularity, in this case

corresponds to OpenMP because it is in the lowest level. Subsequently the implementation follows with MPI, due to its coarse granularity.

Implementation in OpenMP

We started our design with OpenMP because it handles shared memory and it is also the finest granularity. First we partitioned the domain into prisms, and for each prism we parallelized the calculation by observation points, as shown in Figure 4.

This parallelization by observation points is trivial and does not offer a great design challenge, since we simply partition the calculation with respect to the observation grid for each prism (see the pseudo-code 1). However, this scheme has several drawbacks. One of them is that the performance is not optimal since the number of prisms is much greater than the number of observation points. In other words, this partitioning is efficient as long as there are not too many threads working upon the observation grid, thus avoiding a bottleneck issue as a consequence of the threads works in the same memory allocation. Maybe the worst drawback lies in the fact that the parallel environment is created and closed, i.e. for each prism, a function which parallely calculates the anomalies is executed, but such environment is closed once the execution is over, and reopened for the following prism, which results in an unnecessary overload and therefore decreases the performance.

Listing 1. Parallelization by observation points

```
For each prism from 1 to M
!$OMP PARRALLEL DO COLLAPSE(2)
        For each j from 1 to Ny
            For each i from 1 to Nx
            G(i,j)=Gz(parameters)+G(i,j)
            End For
        End For
!$OMP END PARALLEL DO
End For
```

Listing 2. Parallelization by observation points

```
!$OMP PARRALLEL DO
For each prism from 1 to M
        For each j from 1 to Ny
            For each i from 1 to Nx
            G(i,j)=Gz(parameters)+G(Thread,
            i,j)
            End For
        End For
End For
!$OMP END PARALLEL DO
```
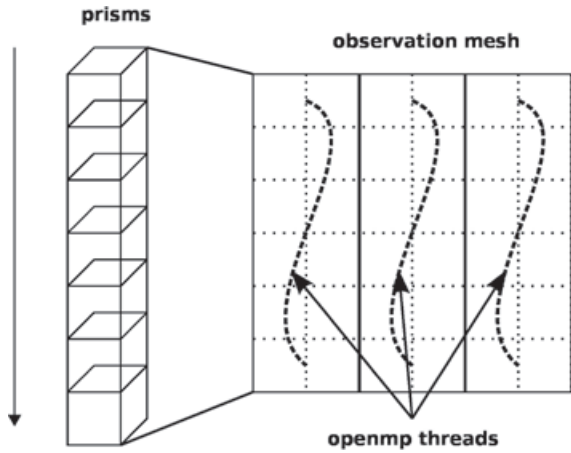
Figure 4. Partitioning by observation points.

The other parallelization option is to use prisms i.e., making the threads divide the work per number of prisms (see pseudo-code 2). To avoid the coherence problems of the cache it is necessary to create a different memory space for each execution thread, because it is not feasible to create a single memory space for an unique observation grid, shared by all the threads.

As observed in Figure 6, it is required to create an observation grid for each execution thread to avoid memory consistency problems. Bottleneck memory access issues are avoided since every thread writes in a different direction of the memory space. If only one grid were to be used, there would be access problems to the shared grid, which would create numerical inconsistencies.

One of the characteristics of OpenMP is that the computing is distributed in an implicit

manner, therefore the partitioning of the M prisms, which composes the problem, is done automatically using a balancing algorithm included in OpenMP. In this case the decision is left to the compiler, which is optimum 99% of the cases (Zhang *et al.*, 2004).

OpenMP+MPI Implementation

One of the advantages of the prism parallelization is that it is easier to implement in MPI, producing tasks of coarse granularity using the same design previously applied in OpenMP. Having the observation grid partitioned would result in a more complicated and less efficient design using MPI. Since the parallelization in MPI is explicit, we need to manually distribute the number of prisms through a modular expression. If M is the number of prisms to calculate and p is the MPI process number (numbered from 0 to $p-1$), then for each process p we define the beginning and end of the prisms to be processed by p as p_{start} and p_{end}, respectively. We define the integer s as the quotient of the number of prisms M between the total number of processes p_n, and
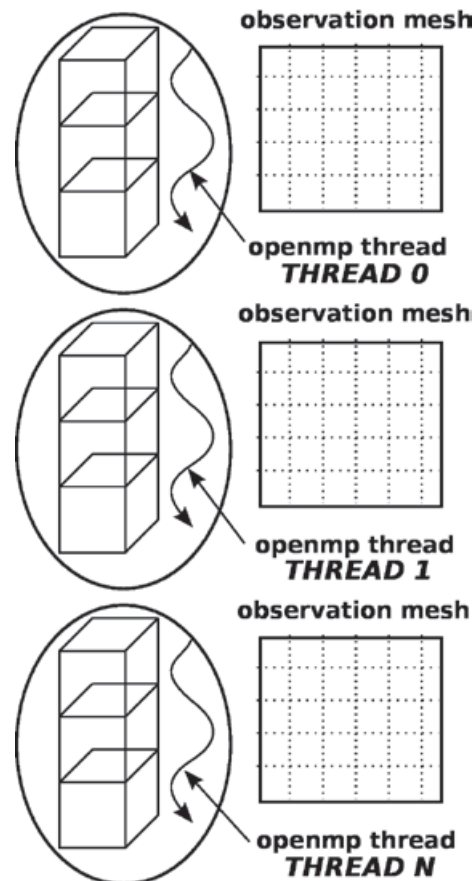
Figure 6. Partitioning by prisms.

Figure 5. Parallel region behavior: (a) pseudo-code (1), (b) pseudo-code (2).

r as the remainder, the procedure to determine p_{start} and p_{end} proceed as follows:

$$s = M/p_n, \qquad (3)$$

$$r = \mathrm{mod}(M/p_n). \qquad (4)$$

Therefore

$$p_{start} = p \times s + 1 \qquad (5)$$

and

$$p_{end} = (p + 1) \times s. \qquad (6)$$

If $r \neq 0$ and $p < r$, then we adjust as:

$$p_{start} = p_{start} + p \qquad (7)$$

and

$$p_{end} = p_{end} + (p + 1). \qquad (8)$$

If $r \neq 0$ and $p \geq r$, then:

$$p_{start} = p_{start} + r \qquad (9)$$

and

$$p_{end} = p_{end} + r. \qquad (10)$$

This way we can distribute the number of prisms M over p_n processes in a balanced manner; once this distribution is made, we can use the OpenMP implementation in each node. In other words, we occupy MPI to distribute the number of prisms in each node, and at the same time in each node we employ OpenMP to reduce the number of MPI processes, reducing communication time.

In consequence, the application is partitioned by the number of prisms M, both in OpenMP as in MPI. Another option is to parallelize by prisms in MPI and by observation points in OpenMP. Even though this is a viable option, it is not very scalable due the drawback discussed in the previous subsection.

Basically the design consists of allocating an observation grid per execution thread and a global observation grid in the master thread per computing node, subsequently the reduction of the sum of the grids per thread is done and stored in the global grid contained in the master thread, and finally at the end of the parallel calculation, every master thread will add their grid values to update the master thread of the master node using a MPI reduction method (see Figure 7).

It is necessary to mention that the implementation of the code was made with the FORTRAN 2003 specification, using as development tool the Intel Cluster Toolkit version 2013 of Intel Corporation.

Performance experiments

For the synthetic experiment we used a case composed by a cube of $700 \times 700 \times 50$ prisms, with 7 contrasting spheres of variable density (see Figure 8). The spheres were conformed by 251,946 prisms and an observation grid of $150 \times 100 = 15,000$ points, to an elevation of 100 m. Therefore, the number of calls to a procedure required, to calculate the vector/tensor component of the gravity are 3,779,190,000; this classifies the experiment into a high-performance computing problem.

We tested the parallelized code by observation points versus the version by prisms using OpenMP. The first parallel scheme is technically easier to implement because for each one of the prisms the calculation of the cycles corresponding to the tracking of the observation grid is parallelized. The second scheme has a more complex implementation because it requires different space memory allocations. The performance experiments that calculate the components of the gravimetric
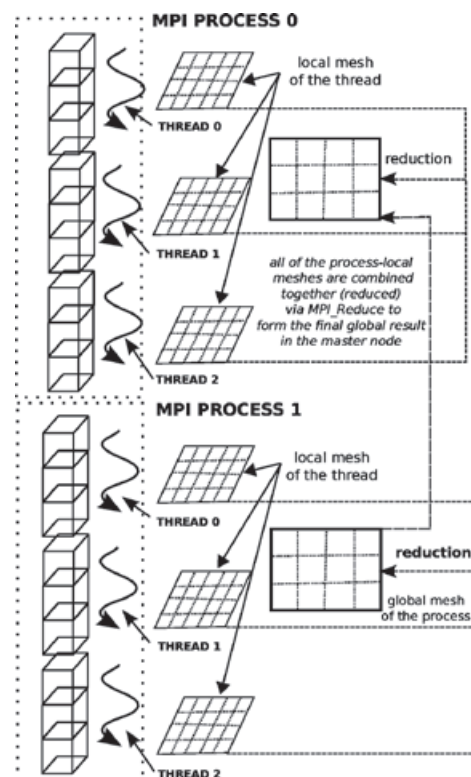
Figure 7. OpenMP+MPI design.
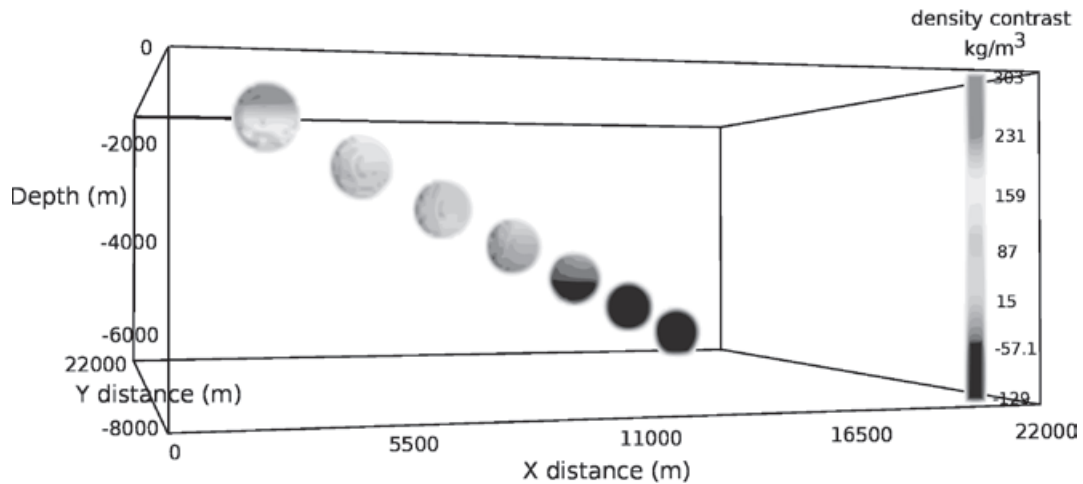
Figure 8. Synthetic problem setup with 7 spheres of variable density contrast (not scaled). Ensemble size of 22 km x 22km x 8km, 251,946 prisms conform the spheres.

tensor G_{xx}, G_{yy}, G_{zz}, G_{xy}, G_{xz}, G_{yz} using both versions were carried out in the server described below. We did not include the performance analysis for the vectorial components G_x, G_y and G_z, since its behavior is very similar.

The characteristics of the server where the tests took place with OpenMP are as follows:

- 4 Xeon Intel (R) Xeon (R) E7-4850 Processors
- 10 processing cores per processor
- Hyperthreading Technology deactivated
- 512 GB of RAM memory
- Red Hat 6.3 as operating system

To interfere as least as possible with the processes of the operating system, we used 35 of the 40 cores available in the server. Initially

we can say that the prisms implementation and with independent memory per core was 3.22X faster than its counterpart of observation points. Therefore, while the observation points version uses 757 s, the version partitioned by prisms only consumes 235 s.

The comparison of the computing times per thread in the partition by prisms against the partition by observation points is shown in Figure 9.

In Figure 9 it can be seen that the performance behavior is kept stable in both types of partitioning; however, by prisms the best reduction in time is obtained. To prove that the partitioning by prisms keeps reduction time practically linear, we graphed the *speed-up* of the performance by prisms.
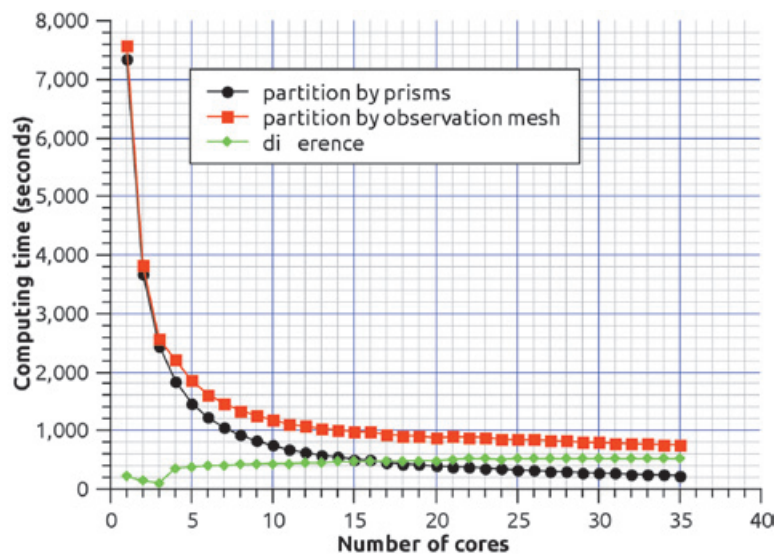
Figure 9. Comparison between execution time used between the partition by prisms against the partition by observation points (one thread per core).

For the *speed-up* shown in Figure 10, we considered a serial fraction of 5% ($f = 0.05$). In this fraction the necessary reductions to sum the grid points for each core are contemplated, the total result of the anomaly is calculated as:

$$O_f(i,j) = \sum_{t=1}^{N_t} O_t(i,j) \qquad (11)$$

where, for each (i, j) O_f is the final observation, O_t is the calculated grid by core t and N_t is the total number of cores. Therefore, we considered that 95% of the code is parallel, and according to Gustafson's law, the maximum *textitspeed-up* that can be obtained with 35 processing units, in this case cores, is 35 + (1-35) × (0.05) = 33.30. The experimentally obtained

speed-up result was 31.31, which represents an absolute difference of 1.99 and a relative difference of 0.06, which shows the efficiency of the implementation.

Another indicator which must be contemplated is the efficiency E, defined as:

$$E = \frac{S(n)}{n} \times 100\% \qquad (12)$$

where $S(n)$ is the obtained *speed-up* with n tasks, and indicates how busy the processors or cores are during execution. Figure 11 shows that the efficiency by prisms is high since on average every processing core is kept busy 94% of the time. The efficiency E also indicates
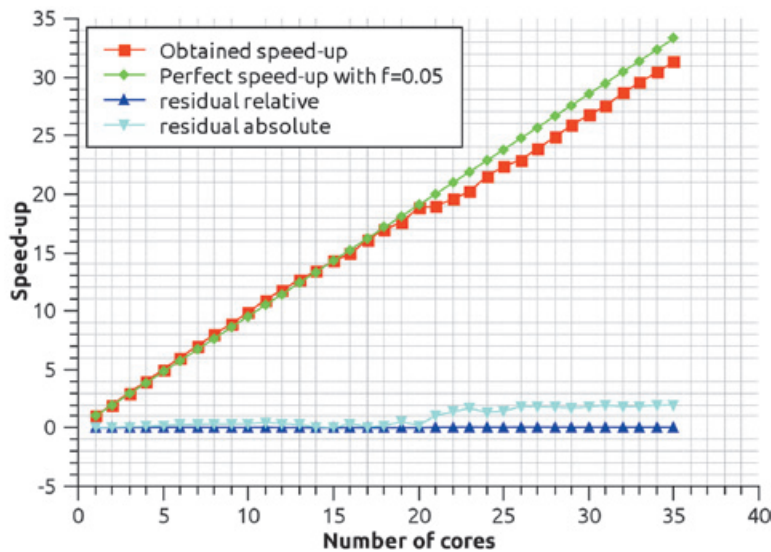
Figure 10. *Speed-up* of the partitioning by prisms (one thread per core).
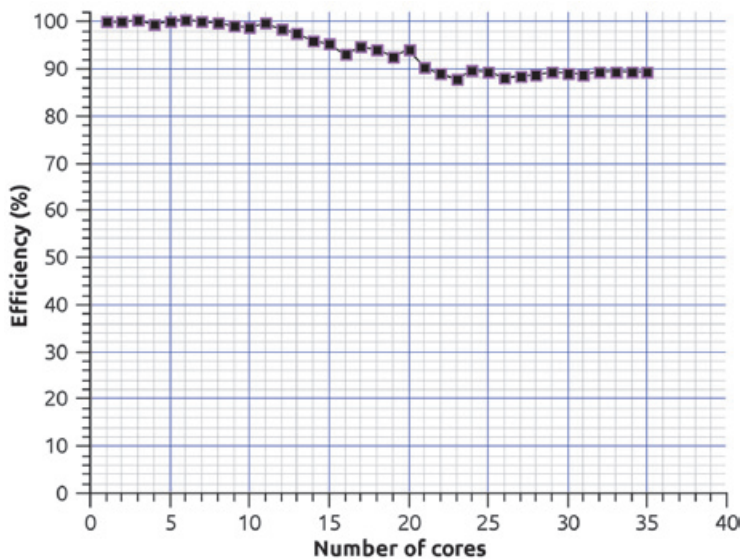
Figure 11. Efficiency of the partitioning by prisms.

that the partitioning by prisms is scalable, which means that we can increase the number of processors to improve time reduction while not losing efficiency in the use of many cores. The scalability must be contemplated as a good design of the parallel program since it allows scaling the algorithm, so we could expect when the number of processing units is increasing the performance is not affected.

The design using OpenMP is limited to architectures of machines of shared memory, therefore we are now making experiments using a hybrid machine commonly known as *cluster*, mixing OpenMP+MPI with the methodology described in subsection 2.2.

The characteristics of the cluster where the numerical experiments were carried out are as follows:

- Node: Intel(R) Xeon(R) model X5550 processors with four physical cores processor.
- 44 processing nodes
- Hyperthreading Technology enabled
- 40 GB of RAM memory per node
- Red Hat 6.3 as operating system
- InfiniBand 300Gbps

We started by evaluating the performance of each cluster node, as opposed to the experiments done with the 40 cores server, where hyperthreading technology (HT) was disabled. In this case HT is enabled, so each node reports the handling of 8 execution threads instead of 4, but we only have 4 physical floating point units (FPUs). Since our program is computationally intensive, we have to find out if we benefit from the use of HT; some studies have reported the use of HT in numerical applications can modify the performance by 30% (Curtis-Maury *et al.*, 2008).

The behavior obtained using one node containing 1 processor with four real cores with HT enabled/disabled can be exposed by an analysis of the computing time graph, shown in Figure 12, the problems analyzed is setup with 13,997 prism conforming a sphere with a mesh of 150 × 100 observations points.

As can be observed, the best run-time performance that we can obtain from the processor in HT mode is not produced with 4 execution threads, the best performance is obtained with 8 threads, but the time is not doubly improved. This occurs since two threads share the same FPU and the HT technology is designed to quickly switch between threads, and therefore there is not a double improvement in time but the performance gain is approximately 30%, which means that the two threads make better use of the FPU,therefore is necessary to create two threads per core to obtain the maximum performance when the HT is enabled. When the HT is disabled we have an asymptotic behavior after 4 threads but did not reach the performance obtained using the HT mode.
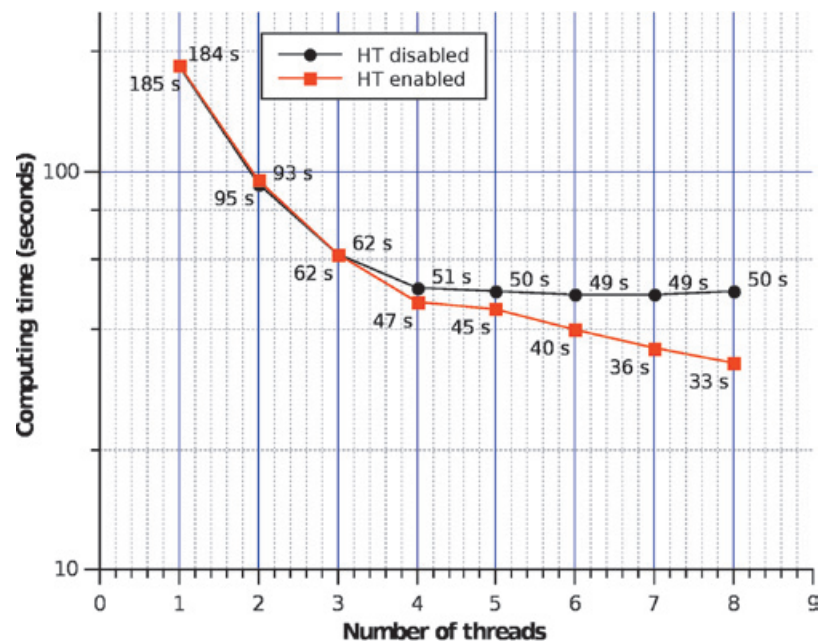
Figure 12. Computing time using only one node with HT enabled/disabled, calculating a problem of 13,997 prisms with 10,000 observation points.

In Figure 13 it can be observed that when HT technology is enabled we obtain a linear *speed-up* up to 4 execution threads; this is obvious since there are only 4 physical FPUs. Nevertheless, with the HT we can have a better use of the FPUs improving the *speed-up* up to 5.60, this is, 1.6 more processing units. With the HT disabled, a similar performance is observed up to 4 threads, although this performance is below the one with the HT enabled. For more than 4 threads, the performance with the HT disabled begins to decrease.

The efficiency corresponding to the *speed-up* shown in Figure 13 is graphed in Figure 14; notice how HT is able to increase the efficiency of some intensive floating point applications up to 30% when the number of threads equals the number of physical cores. Of course, the best efficiency is obtained with 4 threads because we have 4 FPUs, nevertheless we can get a better performance creating 4 threads more using the additional virtual processors created by the HT.
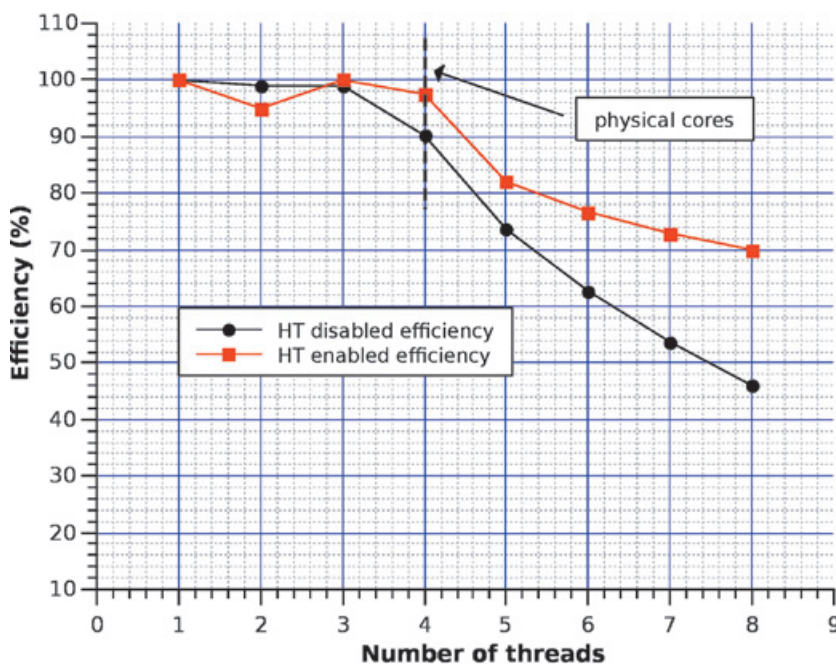
Figure 14. Efficiency using only one node with 4 cores with the HT enabled/disabled for the problem of 13,997 prisms.

To analyze the performance in a node with the original problem (shown in Figure 8), we added a processor in the second socket to one of the nodes. In other words, we created a node with eight real cores to compare it against a node with four real cores with HT enabled. The results of execution time are shown in Figure 15.

It must be taken in consideration our cluster nodes are composed of a single processor with HT enabled, we only added another processor in the second socket to a node for experimental purposes. To have a better perspective of the

performance, we determined the *speed-up* through both node configurations we showed in Figure 16. A nearly perfect *speed-up* can be observed for the node with 8 real cores, but a increase of 1.8 processing units for the node with 4 real cores with HT enabled. Evidently, if we enable HT in the machine with 8 real cores we would have 16 reported processors, and to get its maximum performance we would have to create 16 threads. However, the experimentation with 8 real cores was only for comparisonpurposes, since the cluster configuration is made of one node with 4 real

Figure 15. Eight real cores with HT disabled vs four real cores with HT enabled for the problem setup in the Figure 8.
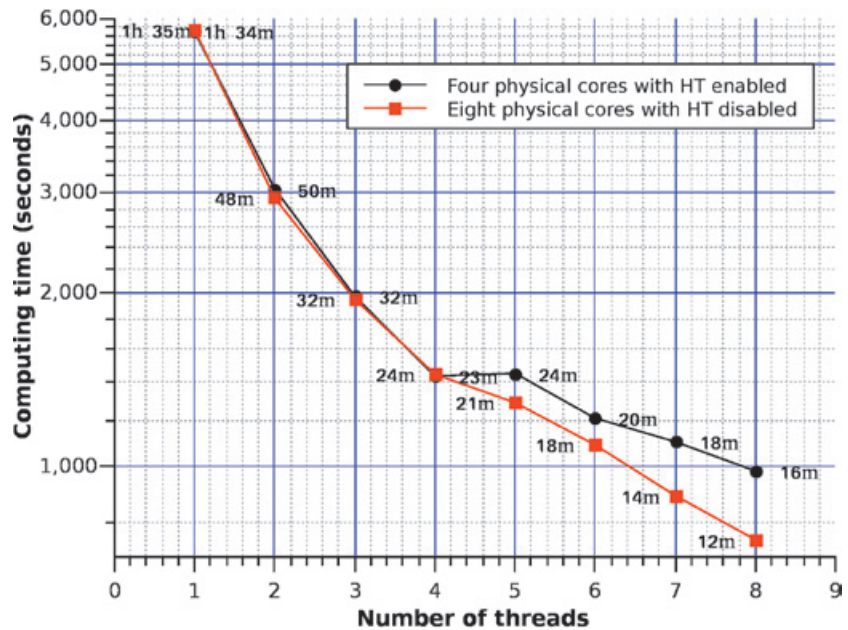
Figure 16. Eight real cores with the HT disabled vs four real cores with HT enabled for the problem setup in the Figure 8.
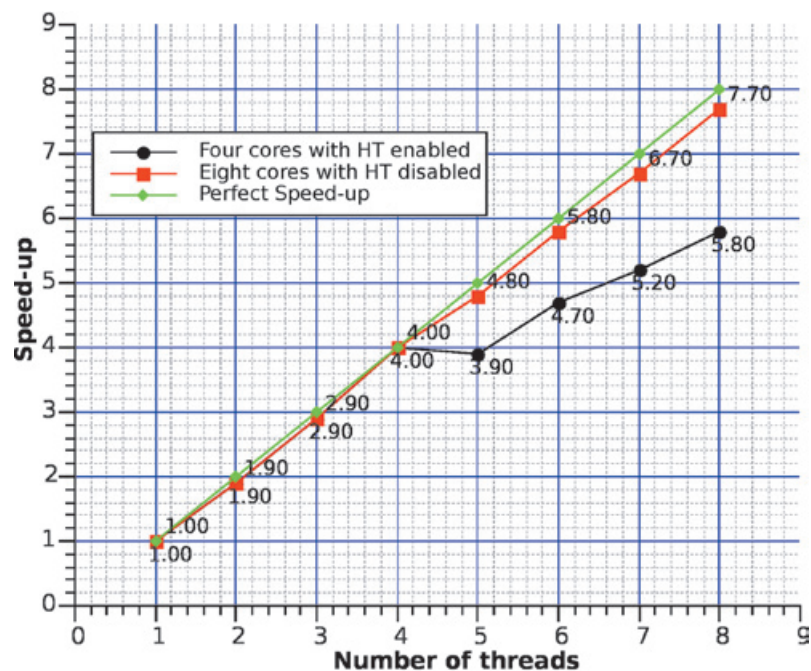
cores with HT enabled. It can also be observed that each node of the cluster reduces the time by a factor of 5,8X against the serial version.

Once it is known that the best node performance is achieved with 8 execution threads for a node with 4 real cores with HT enabled and with the partition by prisms, we can consider each node as a processing unit and distribute the computing with MPI, obtaining a code with a hybrid programming model.

The *speed-up* results using 25 cluster nodes are displayed in Figure 17; a serial fraction of 5% ($f = 0.05$) is considered since in MPI there needs to be reductions in the sum for each node. The results show that a nearly perfect *speed-up* is obtained up to 22 nodes. From this point on, the speed-up starts declining because the application performance is affected by the communication time between nodes. In other words, the granularity of the tasks begins to decrease for this problem of 249,946 prisms
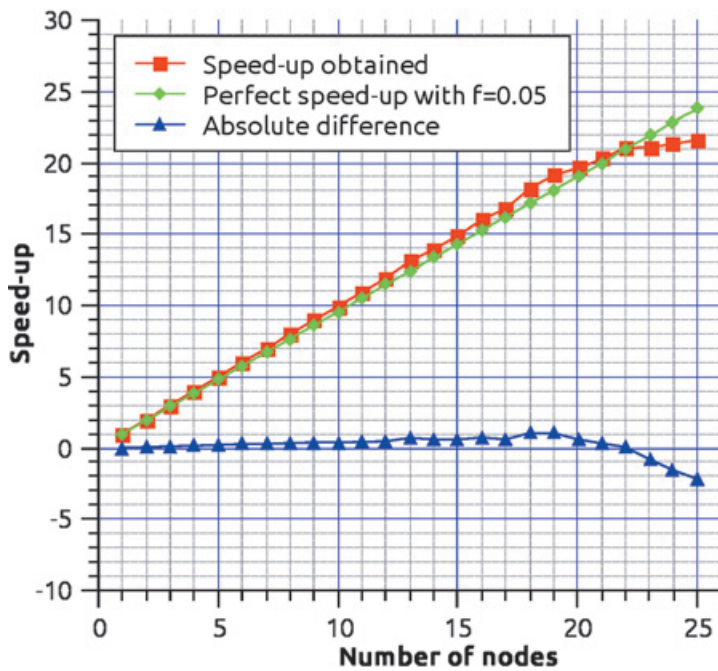
Figure 17. *Speed-up* obtained using 25 cluster nodes.
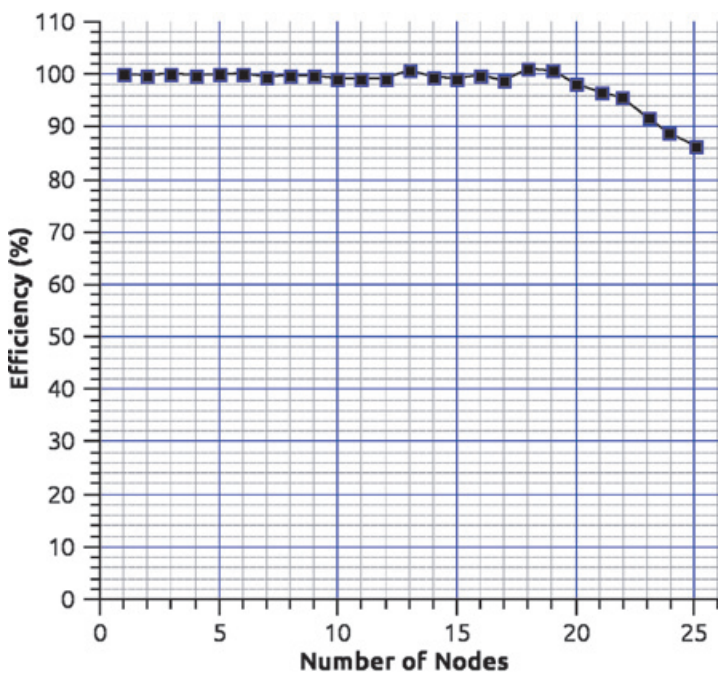
Figure 18. Cluster eficiency using 25 nodes.

for 30 nodes. This implies that by increasing the granularity of the problem (increasing the number of prisms), the *speed-up* is also increased until it becomes stable, to decrease again later on.

The efficiency graph related with the *speed-up* of Figure 16 is shown in Figure 18. Notice how the efficiency is below 90% after node 23. If we consider that we have an increase in speed 5.8 times per node (from Figure 15) with respect to the serial version, then the optimum speed factor for this cluster (for a problem of 251,946 prisms) is approximately 5.8 × 22 = 127.6X, i.e. 127 times faster than the serial version. Obviously, as previously stated, if we increase the granularity (number of prisms), the efficiency increases as well. In fact, we reduce the computation time of the spheres problem from 1 h 34 m 56 s to 34 s

Comparison with similar programs

To provide a better perspective of the obtained performance with the parallel implementation of our code, we compared against an open source code called *tesseroids* (Uieda *et al*., 2011), which can be downloaded from http://dx.doi.org/10.6084/m9.figshare.786514. We chose the problem of 13,997 prisms which form an sphere against 10,000 observation points, since *tesseroids* is not distributed (can not be executed on a cluster) and can only accelerate the computation in shared memory machines. The execution times are shown using the bar chart in Figure 19, where it can be observed that with HT disabled we have

a speed improvement of 2.14X and with HT enabled of 2.51X with respect to *tesseroids*. This performance improvement is due to our program design takes a better advantage of the processor technology and keeps the cores occupied to the maximum by using a prisms parallelization scheme based on different memory allocations. This can be observed in the CPU history graph shown in the Figure 20.

Numerical code validation

The main challenge of the parallel programming is to decompose the program into components which can be simultaneously executed to reduce computing time. The decomposition level is highly influenced by the type of architecture of the parallel machine. In this case the design was made with a hybrid programming strategy to get the maximum out of the architecture. Although the reduction of the execution time is the main objective of the parallel programming, the validation of the code is a topic that should be covered since inherent parallelism programming errors can occur.

To measure the error, we compared the previously validated sequential counterpart in the synthetic experiment with the analytical solution. We used the L2 norm error or RMS (Mickus and Hinojosa, 2001; Menke, 1989), defined as:

$$ \tag{13} $$
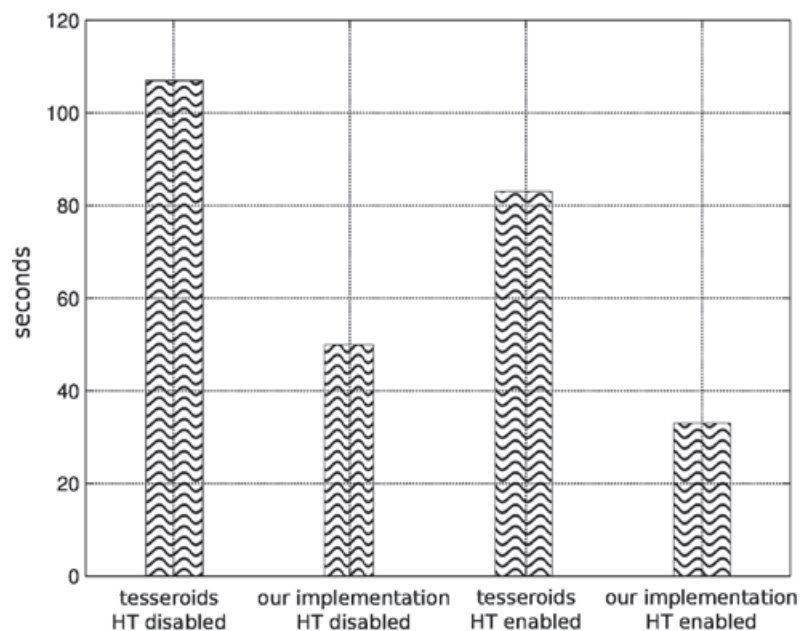
Figure 19. Computing time of our implementation vs tesseroids on one node.
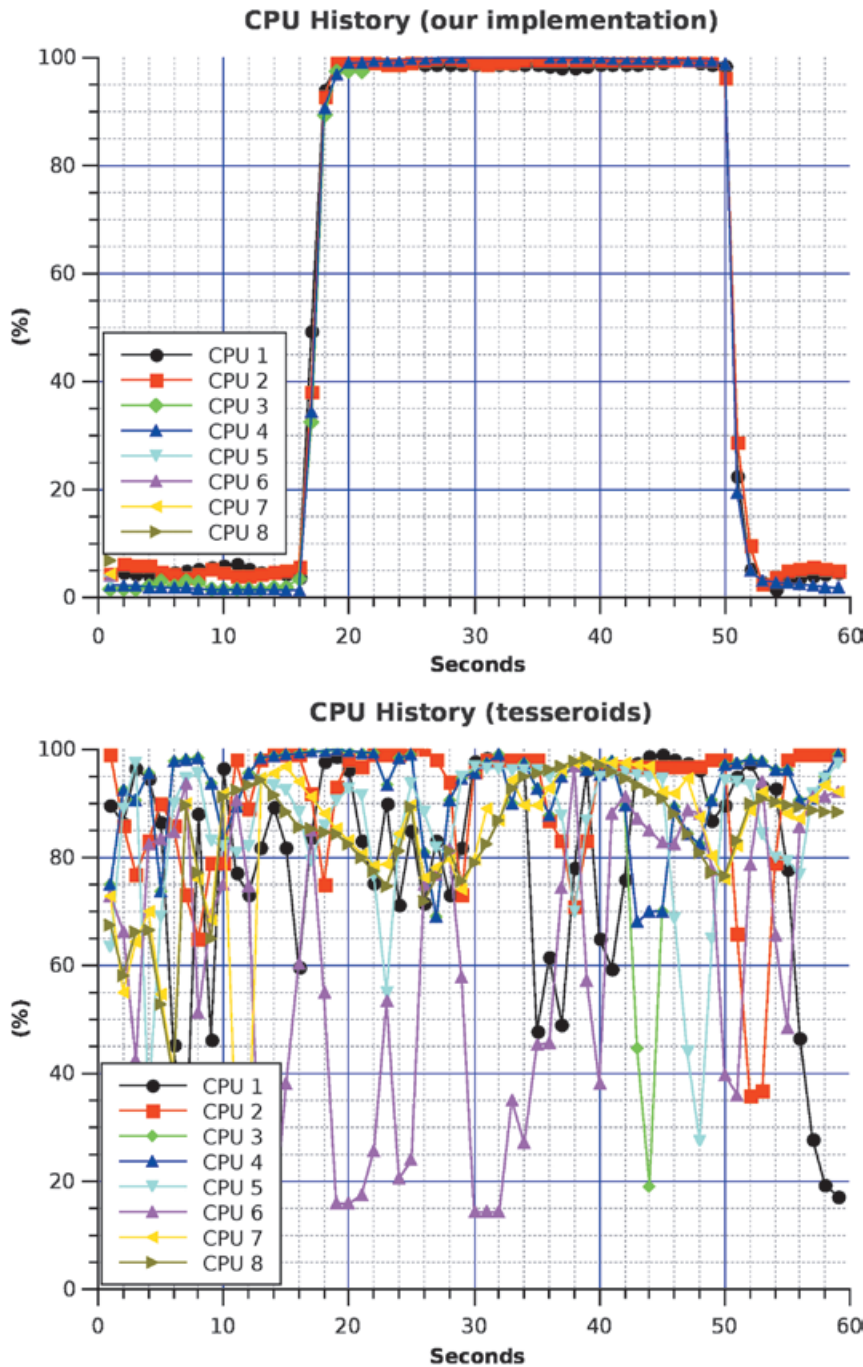
Figure 20. Behavior of the CPU utilization produced by our implementation vs tesseroids. The HT is enabled and note how the cores are used to maximum efficiency in our implementation compared with the partial use of tesseroids.

where $g^p_{i,j}$ is the tensor component, parallely computed, and $g^s_{i,j}$ is the serially calculated component.

In Table 1 the errors of the gravimetric tensor components are shown, parallely calculated with respect to the serial form.

From the errors obtained it can be noticed that there is no numerical difference, therefore the parallel version is correctly implemented.

Table 1. Errors of the tensor components with respect to its sequential counterpart.

Gravity gradient tensor components	Error L2
G_{xx}	6.3136e-12
G_{yy}	6.3054e-12
G_{zz}	2.8367e-12
G_{xy}	1.0244e-14
G_{xz}	1.5518e-14
G_{yz}	1.5581e-14
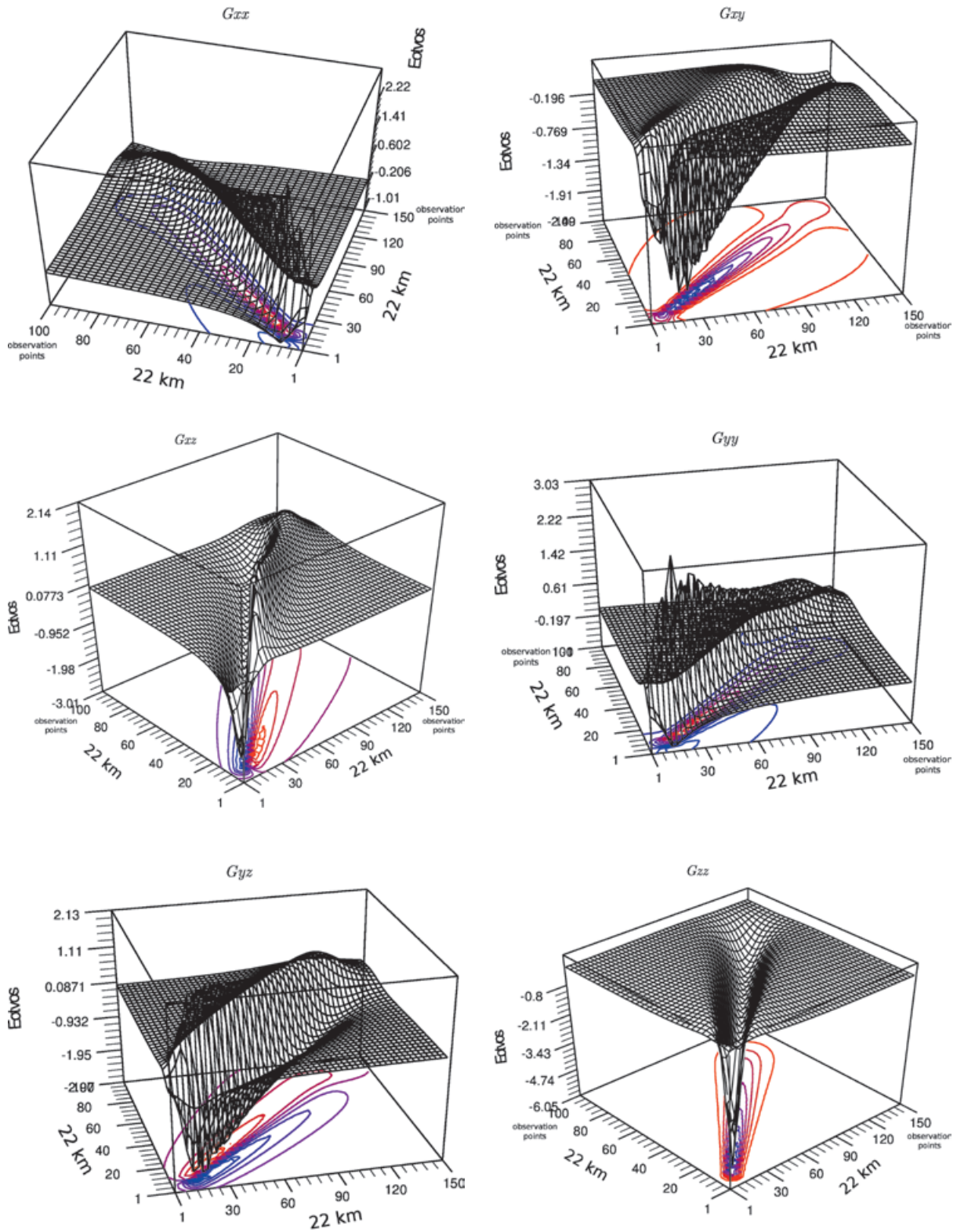
Figure 21. Behavior of the CPU utilization produced by our implementation vs tesseroids. The HT is enabled and note how the cores are used to maximum efficiency in our implementation compared with the partial use of tesseroids.

The surface graphs of the gravitational fields are shown in Figure 21. These graphs correspond to the components of the gravimetric tensor, calculated for the synthetic case studied in Figure 8.

Conclusions

A parallel design for the calculation of the vectorial and tensorial components of the gravity anomaly was implemented and validated using a hybrid methodology with OpenMP and MPI. The numerical experiments and the obtained indicators validate that the implementation is very efficient and that it also yields good results with respect to the numerical solution.

We show that using the simplest or most trivial parallelization form does not contribute to the attainment of the best performance or the greatest exploitation of the platform. For our case, even though the partitioning by prisms requires a greater investment in the design and implementation, it was the most advantageous with respect to performance.

The HT technology could improve some numerical intensive applications up to 30%, nevertheless, to get the best performance it is necessary to create two threads per core when the HT is enabled.

We also conclude that this design can serve as a benchmark for solving problems which require the parallelization of schemes where the decomposition of the domain is not trivial or is shared by the processing units, as is the case of the observation grid. Finally the correct exploitation of OpenMP and MPI, jointly, can become a fundamental tool for parallel programming in clusters.

Future work

As future work we pretend to implement the code in CUDA NVIDIA with TESLA technology and compare these results with the cluster performance results presented in this paper, as the measurement of the error introduced by CUDA in single and double precision. The implementation in CUDA is a work of interest since the reduction of the variable values in CUDA technology is very complicated when used in shared form, as is the case with the observation grid.

Appendix A. Calculation of gravitational quantities

The Earth's gravitational potential G is a scalar quantity, its shape can be constrained by its slope in the x, y and z directions, called the gravitational attraction G_x, G_y and G_z (gravity vector field). In this work, we have investigated how to parallelize the analytical calculation of the components of the gravity field vector and the gravity gradients represented by a nine component tensor, because of the symmetrical or irrotational attribute, the gravity gradient tensor is reduced to only six independent components: G_{xx}, (the vertical gravity gradient), and For the right rectangular prism model, the analytical formulae for the three components vectors and the six gravity gradient components, corresponding to the Eq. (2) are given by:

$$G_x = \gamma \rho \sum_{i=1}^{2} \sum_{j=1}^{2} \sum_{k=1}^{2} \mu_{ijk}$$

$$\times [y_j \ln(z_k + r_{ijk}) + z_k \ln(y_j + r_{ijk}) - x_i \arctan\frac{y_j z_k}{x_i r_{ijk}}]$$

$$G_y = -\gamma \rho \sum_{i=1}^{2} \sum_{j=1}^{2} \sum_{k=1}^{2} \mu_{ijk}$$

$$\times [z_k \ln(x_i + r_{ijk}) + x_i \ln(z_k + r_{ijk}) - y_j \arctan\frac{z_k x_i}{y_j r_{ijk}}]$$

$$G_z = -\gamma \rho \sum_{i=1}^{2} \sum_{j=1}^{2} \sum_{k=1}^{2} \mu_{ijk}$$

$$\times [z_k \ln(x_i + r_{ijk}) + x_i \ln(z_k + r_{ijk}) - y_j \arctan\frac{z_k x_i}{y_j r_{ijk}}]$$

$$G_{xx} = \gamma \rho \sum_{i=1}^{2} \sum_{j=1}^{2} \sum_{k=1}^{2} \mu_{ijk} \arctan\frac{y_j z_k}{x_i r_{ijk}}$$

$$G_{yy} = \gamma \rho \sum_{i=1}^{2} \sum_{j=1}^{2} \sum_{k=1}^{2} \mu_{ijk} \arctan\frac{x_i z_k}{y_j r_{ijk}}$$

$$G_{zz} = \gamma \rho \sum_{i=1}^{2} \sum_{j=1}^{2} \sum_{k=1}^{2} \mu_{ijk} \arctan\frac{x_i y_j}{z_k r_{ijk}}$$

$$G_{xy} = \gamma \rho \sum_{i=1}^{2} \sum_{j=1}^{2} \sum_{k=1}^{2} \mu_{ijk} \ln(z_k + r_{ijk})$$

$$G_{xz} = \gamma \rho \sum_{i=1}^{2} \sum_{j=1}^{2} \sum_{k=1}^{2} \mu_{ijk} \ln(y_k + r_{ijk})$$

$$G_{yz} = \gamma \rho \sum_{i=1}^{2} \sum_{j=1}^{2} \sum_{k=1}^{2} \mu_{ijk} \ln(x_i + r_{ijk})$$

Acknowledgment

References

Amritkar A., Tafti D., Liu R., Kufrin R., Chapman B., 2012, OpenMP parallelism for fluid and fluid-particulate systems. *Parallel Computing*, 38, 9, 501-517.

Boehmer S., Cramer T., Hafner M., Lange E., Bischof C., Hameyer K., 2012, Numerical simulation of electrical machines by means of a hybrid parallelisation using MPI and OpenMP for finite-element method. *Science, Measurement & Technology*, IET, 6, 5, 339-343.

Brunst H., Mohr B., 2008, Performance analysis of large-scale OpenMP and hybrid MPI/OpenMP applications with Vampir NG. In OpenMP Shared Memory Parallel Programming (pp. 5-14). Springer Berlin Heidelberg.

Calvin C., Ye F., Petiton S., 2013, October, The Exploration of Pervasive and Fine-Grained Parallel Model Applied on Intel Xeon Phi Coprocessor. In P2P, Parallel, Grid, Cloud and Internet Computing (3PGCIC), 2013 Eighth International Conference on (pp. 166-173). IEEE.

Carrillo-Ledesma A., Herrera I., de la Cruz L.M., 2013, Parallel algorithms for computational models of geophysical systems. *Geofísica Internacional*, 52, 3, 293-309.

Couder-Castañeda C., 2010. Simulation of supersonic flow in an ejector diffuser using the jpvm. *Journal of Applied Mathematic*s, 2009.

Curtis-Maury M., Ding X., Antonopoulos C.D., Nikolopoulos D.S., 2008, An evaluation of OpenMP on current and emerging multithreaded/multicore processors. In OpenMP Shared Memory Parallel Programming (pp. 133-144). Springer Berlin Heidelberg.

Dagum L., Menon R., 1998, OpenMP: an industry standard API for shared-memory programming. *Computational Science & Engineering*, IEEE, 5(1), 46-55.

Foster I., 1995, Designing and building parallel programs (pp. 83-135). Addison Wesley Publishing Company.

Gonzalez B., Donate J.P., Cortez P., Sánchez G., De Miguel A., 2012, May, Parallelization of an evolving Artificial Neural Networks system to Forecast Time Series using OPENMP and MPI. In Evolving and Adaptive Intelligent Systems (EAIS), 2012 IEEE Conference on (pp. 186-191). IEEE.

Heck B., Seitz K., 2007, A comparison of the tesseroid, prism and point-mass approaches for mass reductions in gravity field modelling. *Journal of Geodesy*, 81, 2, 121-136.

Jagannathan S., Donzis D.A., 2012, July, Massively parallel direct numerical simulations of forced compressible turbulence: a hybrid MPI/OpenMP approach. In Proceedings of the 1st Conference of the Extreme Science and Engineering Discovery Environment: Bridging from the eXtreme to the campus and beyond (p. 23). ACM.

Krpic Z., Martinovic G., Crnkovic I., 2012, May). Green HPC: MPI vs. OpenMP on a shared memory system. In MIPRO, 2012 Proceedings of the 35th International Convention (pp. 246-250). IEEE.

Kornyei L., 2012, May, Parallel implementation of a combustion chamber simulation with MPI-OpenMP hybrid techniques. In MIPRO, 2012 Proceedings of the 35th International Convention (pp. 356-361). IEEE.

Menke W., 2012, Geophysical data analysis: discrete inverse theory. Academic press.

Mickus K.L., Hinojosa J.H., 2001, The complete gravity gradient tensor derived from the vertical component of gravity: a Fourier transform technique. J*ournal of Applied Geophysics*, 46, 3, 159-174.

Mitin I., Kalinkin A., Laevsky Y., 2012, A parallel iterative solver for positive-definite systems with hybrid MPI–OpenMP parallelization for multi-core clusters. *Journal of Computational Science*, 3, 6, 463-468.

Nagy D., Papp G., Benedek J., 2000, The gravitational potential and its derivatives for the prism. Journal of Geodesy, 74(7-8), 552-560.

Sariyuce A.E., Saule E., Catalyurek U.V., 2012, May, Scalable hybrid implementation of graph coloring using mpi and openmp. In Parallel and Distributed Processing Symposium Workshops & PhD Forum (IPDPSW), 2012 IEEE 26th International (pp. 1744-1753). IEEE.

Smith L.A., 2000, Mixed mode MPI/OpenMP programming. *UK High-End Computing Technology Report*, 1-25.

Uieda L., Bomfim E., Braitenberg C., Molina E., 2011, July, Optimal forward calculation method of the Marussi tensor due to a geologic structure at GOCE height. In Proceedings of GOCE User Workshop 2011.

Zhang Y., Burcea M., Cheng V., Ho R., Voss M., 2004, September, An Adaptive OpenMP Loop Scheduler for Hyperthreaded SMPs. In ISCA PDCS (pp. 256-263).

Estimation of multiple density-depth parameters from gravity inversion: Application to detached hanging wall systems of strike limited listric fault morphologies

V. Chakravarthi* and M. Pramod Kumar

Resumen

Se desarrolló un algoritmo de inversión para estimar simultáneamente la geometría de plano de falla y los parámetros que pertenecen a cualquiera de las densidades o profundidades de múltiples formaciones geológicas, con el sistema de colgado en la pared, en un plano de fractura limitada de las anomalías de gravedad observadas. Se describen planos de falla de las estructuras mediante funciones polinómicas de grado arbitrario pero específico. La aplicabilidad del algoritmo se demostró tanto en las anomalías artificiales y reales de la gravedad de campo. En el ejemplo de síntesis se añadió ruido pseudoaleatorio a las anomalías de gravedad de la estructura antes de la inversión. En la inversión de anomalías de gravedad, producidos por una estructura sintética, se encontró que los parámetros estimados más o menos imitan los parámetros obtenidos, incluso en presencia de ruido aleatorio. Las densidades y profundidades estimadas de las formaciones de inversión independiente de anomalías de gravedad del mundo real desde el margen de la subcuenca Chintalpudi en la India se correlacionan bien con la información disponible de la perforación.

Palabras clave: morfología de fallas lístricas, falla finita, variaciones arbitrarias de densidad-densidad, anomalía de gravedad, inversión.

Abstract

An inversion algorithm is developed to simultaneously estimate the fault plane geometry and the parameters pertaining to either densities or depths of multiple geologic formations within the hanging wall system of a strike-limited listric fault from the observed gravity anomalies. Fault planes of the structures are described by polynomial functions of arbitrary but specific degree. The applicability of the algorithm is demonstrated on both synthetic and real field gravity anomalies. In the synthetic example, pseudorandom noise is added to the gravity anomalies of the structure prior to inversion. From the inversion of gravity anomalies produced by a synthetic structure it was found that the estimated parameters more or less mimic the true parameters even in the presence of random noise. The estimated densities and depths of the formations from independent inversion of real-world gravity anomalies from the margin of the Chintalpudi sub-basin in India correlate well with the available drilling information.

Key words: listric fault morphology, finite strike, arbitrary density-density variations, gravity anomaly, inversion.

V. Chakravarthi*
M. Pramod Kumar
Centre for Earth & Space Sciences
University of Hyderabad
Gachibowli, Hyderabad – 500 046 (A.P.)
India
*Corresponding author:vcvarthi@rediffmail.com

Introduction

Listric faults are curved normal faults in which the fault surface is concave upwards because the main detachment fracture follows a curved path rather than a planar path. Because of the non-planar nature of listric fault planes it is often difficult to estimate the amount of extension from surface geological observations of dip and throw of the faults (Mckenzie, 1978). On the other hand, the displaced rock masses on either side of such fault planes can create lateral contrasts in subsurface densities and accordingly generate detectable step-like gravity anomalies across the fault planes. These anomalies can be appropriately analyzed to quantify the fault morphology.

Although fault morphologies more often than not possess non-planar fault planes (Brady *et al.* 2000; Goussav *et al.* 2006; McKenzie and Jackson 2012), many existing algorithms assume planar surfaces for the fault planes to analyze the gravity anomalies. For example, Thanassoulas *et al.* (1987) developed a method and a computer program in Basic, Murthy and Krishnamacharyulu (1990) devised an algorithm and a relevant code in Fortran to estimate the parameters of fault structures from the observed gravity anomalies. Abdelrahman *et al.* (1989) proposed a method to determine the dip angle of a fault plane from the maximum positive and negative amplitudes of gravity anomalies, where the relative movement between two semi-infinite horizontal slabs was confined to a planar surface. Rao *et al.* (2003) used generalized inversion and single value decomposition techniques to analyze the gravity anomalies of fault structures. Abdelrahman *et al.* (2003) presented two approaches to determine the depth and amplitude coefficient, related to the density contrast and the thickness of a buried faulted slab using numerical horizontal derivative anomalies obtained from 2D gravity data. On the other hand, Stavrev and Reid (2010) used the concept of extended Euler homogeneity of potential fields to analyze the gravity anomalies of a thick faulted slab. Recently, Essa (2013) developed an algorithm that make use of numerical first horizontal derivatives computed from the observed gravity anomaly to estimate the depth and the dip angle of a buried fault structure, whereas Toushmalani (2013) proposed a technique using particle swarm optimization to interpret the anomalies.

The above 2D strategies find limited application when analyzing the gravity anomalies of listric fault morphologies because

i) the fault planes associated with these structures are often non-planar in nature, and ii) the density of the sedimentary load within the hanging wall is rarely uniform (Maxant 1980; Moral *et al.* 2000; Rybakov *et al.* 2000; Nagihara and Hall, 2001; Adriasyah and McMechan, 2002; Gómez-Ortiz 2005). Realizing the fact that the density of sedimentary rocks varies with depth, Rao (1985) used a quadratic density function, Sundararajan and Brahmam (1998) adopted a linear density function, and Chakravarthi and Sundararajan (2004) used a parabolic density function to analyze the gravity anomalies of fault structures, again treating the fault structures as 2D with fault planes as planar surfaces.

Martín-Atienza and García-Abdeslem (1999) developed a technique using a quadratic density function to compute the gravity anomalies of geologic sources bounded either laterally or vertically by continuous functions. Though this method can be used to simulate the geometries of listric fault sources to compute gravity anomalies, it is efficient only for 2D sources. Based on the fact that the fault structures on the continental regions often possess finite strike lengths (Peirce and Lipkov 1988), Chakravarthi (2011) developed an automatic inversion to interpret the gravity anomalies of 2.5D strike listric fault sources, where the fault planes are described by polynomial functions of arbitrary degree and the variation of density within the hanging wall by a parabolic density function. This technique is effective when the density contrast of sedimentary load within the hanging wall decreases monotonically with depth. On the other hand, Chakravarthi (2010) devised a strategy with a relevant code in Fortran to compute the gravity anomalies of strike limited listric fault morphologies, where the hanging wall was assumed to consist in several geologic formations of differing densities and thicknesses. To realize forward modeling, this method requires the coefficients of the polynomial (used to describe the fault plane geometry) and the parameters pertaining to both thickness and densities of formations within the hanging wall as part of input, which in reality are not known a priori. Therefore, a need exists to develop an appropriate algorithm to estimate these parameters from the observed gravity anomalies (inverse process).

In the present paper, we develop a gravity inversion technique using ridge regression to estimate the parameters of a listric fault structure from the observed gravity anomalies, where the structure is assumed as a 2.5D source with the detached hanging wall consists in several geologic formations; each one

possesses its own density and thickness. The forward modeling algorithm of Chakravarthi (2010) is used to compute the gravity response of a listric fault structure whereas the business logic of the present inversion estimates the unknown parameters based on the differences between the measured and model gravity anomalies. In this case, the unknown parameters to be estimated from a gravity profile are: depths or densities of formations (because the density and the volume of the source cannot be determined without prior information about one of them) and coefficients of a polynomial used to describe the fault plane as a function of depth. The validity and applicability of the technique are demonstrated with both synthetic and real field gravity anomalies. The estimated parameters are compared with the assumed parameters in case of synthetic example and with measured density-depth data in case of a real field example.

Gravity anomalies of strike limited listric fault sources

In a Cartesian co-ordinate system, let the z-axis be positive vertically downwards and the x-axis transverse to the strike of a listric fault source whose geometry is shown in Figure 1. The structure is located between the limits, z_T and z_B, along the z-axis and along the x-axis, the structure is bounded by a function, $\zeta(z)$, on the left and towards the right it is extending to infinity. Further, the structure is having a limited strike length of $2Y$ along the y-axis perpendicular to the xz plane. The detached hanging wall of the structure consists of several geological formations, N in number.

Further, each formation has its own density, ρ_i, $i = 1, 2, ..., N$. For such a structure, the gravity anomaly, $g_{mod}(x_j, z_j)$, at any point, $P(x_j, z_j)$, on the profile, CD, that runs along the x-axis and bisects the strike length, $2Y$, of the structure outside the source region is given by (Chakravarthi 2010),

$$g_{mod}(x_j, z_j) = 2G \sum_{k=1}^{N} \Delta\rho_k \int_{z_k}^{z_{k+1}} \left[\tan^{-1}\frac{Y}{(z-z_j)} - \tan^{-1}\frac{Y(\zeta(z)-x_j)}{(z-z_j)\sqrt{(\zeta(z)-x_j)^2+(z-z_j)^2+Y^2}} \right] dz,$$

(1)

where, G is the universal gravitational constant, $\Delta\rho_k$ is the density contrast of the kth formation, z_k and z_{k+1} represent the depths to the top and bottom bounding surfaces of the respective formation within the hanging wall. Further, the fault plane is described by a function, $\zeta(z) = \sum_{l=0}^{N1} f_l z^l$, where f_l represent the coefficients of the polynomial. It is convenient to solve equation (1) by means of a numerical method rather than an analytical method because the polynomial, $\zeta(z)$, may take any degree (Chakravarthi 2010). In case the profile runs at an offset, s, (such as the profile, C'D' in Figure 1) across the strike then the anomalous field at any point on the profile outside the source region can be calculated as in equation (1) but by substituting, $Y - s$ and $Y + s$ for Y (Chakravarthi, 2010). Also if the profile runs at an angle, α, with the x-axis then x_j in Eq. (1) needs to be replaced by $x_j \cos\alpha$ (Chakravarthi and Ramamma, 2013).
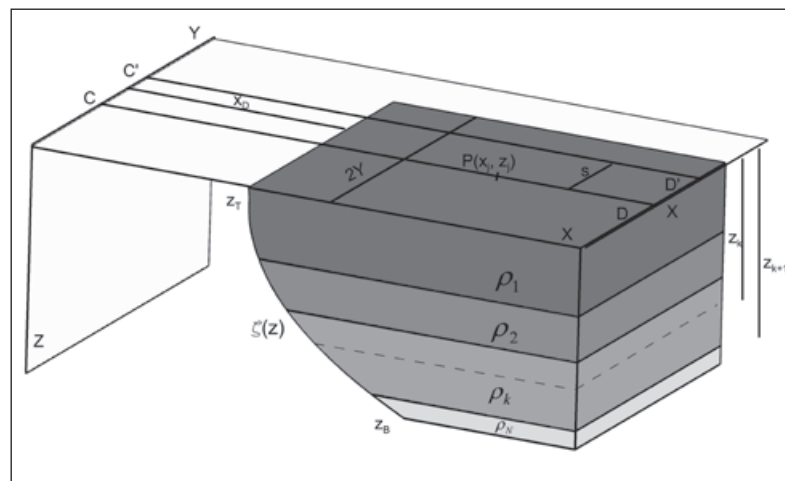

Figure 1. Schematic representation of a strike limited listric fault source. The detached downthrown block (hanging wall) is consisting of N horizontal formations with differing depths and densities. The limited strike length prevents the structure to represent as a 2D source.

Inversion of gravity anomalies

Inversion of gravity anomalies of listric fault sources is tantamount to a mathematical exercise of trying to fit the observed gravity anomalies to the anomaly expression and solve the unknown parameters within specified convergence criteria such that the inferred model is geologically acceptable. We propose two variants of inversion to analyze the gravity anomalies: i) densities and coefficients of the polynomial, $\zeta(z)$, are estimated while keeping the depths of the density interfaces intact, and ii) depths and coefficients of the polynomial are estimated while keeping the densities of the formations intact.

In either case, the interpretation starts by assigning approximate parameters of the structure (densities or depths of the formations) supplemented by drilling/other geophysical methods. To start with, the algorithm identifies the approximate location of the fault plane, x_D, (Figure 1) on the profile at a point at which the corresponding anomalous field reaches to one half the maximum anomaly (Chakravarthi 2011). Initially, this value is assigned to the constant term, f_0, of the polynomial, $\zeta(z)$, while the other coefficients are set to zero. These initial parameters of the structure are used to calculate the modeled gravity anomalies, $g_{mod}(x_j, z_j)$, using equation (1). Because the initial parameters are only approximate, the modeled gravity anomalies deviate from the observed anomalies. The difference between the observed anomalies, $g_{obs}(x_j, z_j)$, and the modeled anomalies, $g_{mod}(x_j, z_j)$, at any point, $P(x_j, z_j)$, on the profile can be expressed as a cumulative effect of a truncated Taylor's series expansion involving the partial derivatives of anomaly with respect to each unknown parameter and corresponding increment as

$$g_{obs}(x_j,z_j) - g_{mod}(x_j,z_j) = \sum_{k=1}^{N} \frac{\partial g_{mod}(x_j,z_j)}{\partial a_k} da_k + \sum_{m=0}^{N1} \frac{\partial g_{mod}(x_j,z_j)}{\partial f_m} df_m, \quad (2)$$

where, da_k are increments/decrements in the parameters pertaining to either densities or depths and df_m are the increments/decrements to the coefficients of the polynomial used to describe the fault plane.

Linear equations similar to equation (2) are constructed for each observation on the profile and $(N + N1 + 1)$ normal equations are formed and solved by minimizing the misfit, J, between the observed and modeled gravity anomalies defined by

$$\sum_{j=1}^{N_{obs}} \left[g_{obs}(x_j,z_j) - g_{mod}(x_j,z_j) \right]^2 \quad (3)$$

using ridge regression (Marquardt, 1970). Here, N_{obs} stands for the number of observations on the profile. The relevant system of normal equations can be expressed in a matrix form as

$$(A + \delta I) X = B, \quad (4)$$

where, A is nxn matrix whose elements $A_{nj'}$ are given by

$$A_{nj'} = \sum_{n=1}^{N+N1+1} \sum_{m=1}^{N_{obs}} \frac{\partial g_{mod}(x_m,z_m)}{\partial a_{j'}} \frac{\partial g_{mod}(x_m,z_m)}{\partial a_n}, \quad (5)$$

$$X = da_n, \quad (6)$$

$$B = \sum_{m=1}^{N_{obs}} \left[g_{obs}(x_m,z_m) - g_{mod}(x_m,z_m) \right] \frac{\partial g_{mod}(x_m,z_m)}{\partial a_{j'}}, \ j'=1,2,....,N+N1+1 \quad (7)$$

where, a_n, $n = 1, 2, ..., N + N1 + 1$ are the number of unknown parameters and da_n represents the corresponding improvements in the parameters. δ is the damping factor and I is a diagonal matrix containing the diagonal elements of the matrix A. The application of ridge regression is described by Chakravarthi and Sundararajan (2006). The partial derivatives required in Eq. (5) and Eq. (7) are evaluated numerically (Chakravarthi *et al.* 2001), which involves the calculation of the rate of change of the gravity anomaly with respect to each unknown parameter. The improvements, da_n, solved from Eq. (4) are used to update the existing parameters and the exercise repeats until i) the specified number of iterations completed or ii) the misfit becomes less than the predefined allowable error or iii) the damping factor, δ, assumes an unusually large value (Chakravarthi, 2003).

Examples

The applicability of the algorithm is demonstrated on both synthetic and real field gravity anomalies. In either case the measurement is made at $z_j = 0$ km.

Theoretical example

Figure 2a shows a set of noisy gravity anomalies produced by a synthetic listric fault model, whose geometry is shown in Figure 2b. The structure has a half strike length of 50 km (Figure 2b). The anomalies (shown as solid line in Figure 2a) are produced at zero offset

in the interval $x_j \in$ [0, 80 km]. In this case, the pseudorandom noise was Gaussian, with zero mean and a standard deviation of 0.14 mGal. The foot wall remains intact and undisturbed, whereas the detached hanging wall consists of four formations: massive basalt of 3.5 km thick at the top is followed successively by 1.5 km thick sediments, 3 km thick vesicular basalt and 2.0 km thick compacted sediments above the basement. The model densities of the formations are given in Table 1 and shown in Figure 2c. In the present case, a 6th degree polynomial with a set of seven arbitrarily chosen coefficients (Table 2) is used to describe the fault plane geometry (shown as solid line in blue in Figure 2b).

We have used two prong strategies to analyze the gravity anomalies as described in section 3. Initially, the densities of the formations and polynomial coefficients (to describe the fault plane geometry) are estimated from the noisy anomalies (shown in Figure 2a) while keeping the depths of density interfaces unchanged, and secondly the depths of the interfaces and coefficients of the polynomial are estimated keeping the densities intact. Further, in either case a 2nd degree polynomial is used (instead of a 6th degree) to describe the fault plane in the inversion to study its effect on the interpretation, if any.

Inversion of noisy anomalies to estimate densities and fault plane geometry

The noisy anomalies (Figure 2a) were subjected to inversion assuming an initial density of 2.0 g/cm³ for each of the subsurface formation (Table 1 and Figure 2c). The algorithm calculates the density contrast of each formation and uses them to compute the gravity effect of the structure. The approximate location of the fault plane identified by the algorithm is at 30.07 km on the profile. Initially, this value has been assigned to the first coefficient of the polynomial, f_0, whereas other coefficients are set to zero as described in the text. For such an inversion, the algorithm had performed 69 iterations before it got terminated as the misfit, J, fell below a predefined allowable error of 0.01 mGal. No significant improvements either in densities or coefficients of the polynomial are observed beyond the 69th iteration (Figure 3b).

Table 1. Assumed and estimated densities in case of synthetic example

Formation	Assumed density (g/cm³)	Initial density (g/cm³)	Estimated density (g/cm³)	Error (%)
Compact basalt	2.9	2.0	2.89	0.34
Sediments	2.4	2.0	2.44	1.67
Vesicular basalt	2.8	2.0	2.78	0.71
Compacted sediments	2.5	2.0	2.51	0.4

Table 2. Assumed and estimated coefficients of the polynomial, $\zeta(z)$, synthetic example

Coefficient	Assumed coefficients of the 6th degree polynomial	Estimated coefficients of the 2nd degree polynomial in case of density and fault plane inversion	Estimated coefficients of the 2nd degree polynomial in case of depth and fault plane inversion
f_0	30.01900944	30.036317825	30.029928207
f_1	0.09650391535	0.070503563	0.076575279
f_2	0.1845273787	0.106036872	0.110244833
f_3	-0.07319248817		
f_4	0.01707929702		
f_5	-0.001753613786		
f_6	7.009779208E-005		

Figure 2. (a) Observed and modeled noisy gravity anomalies, (b) four layered hanging wall system of a synthetic listric fault source with assumed and modeled fault planes described by 6th and 2nd degree polynomials, (c) assumed, initial and modeled densities. Depths of density interfaces are fixed during inversion.
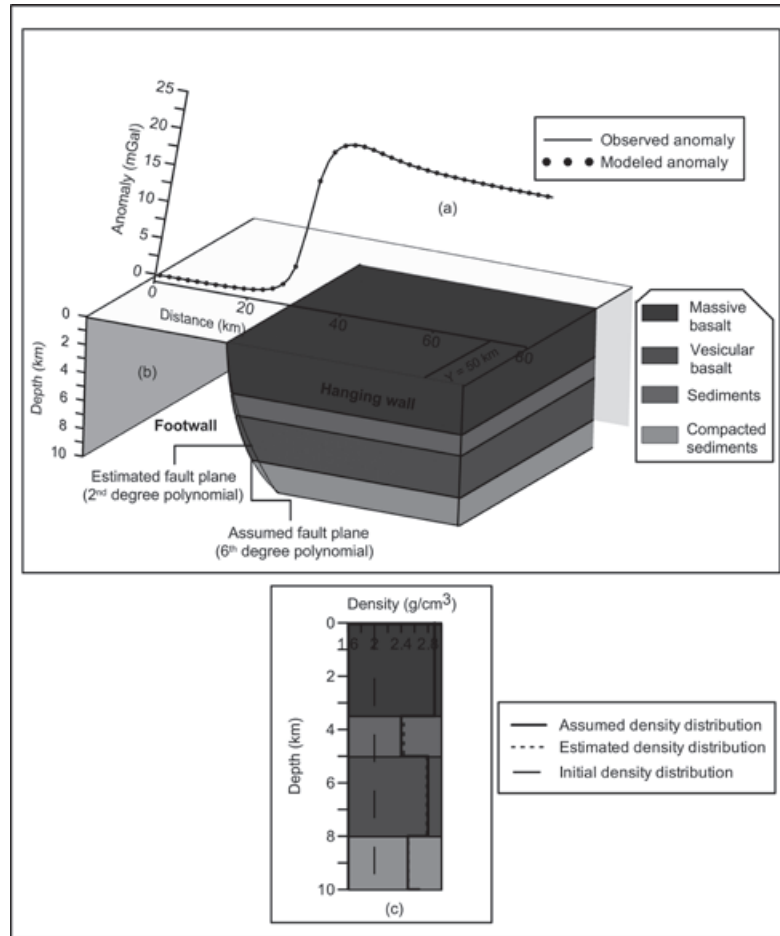
The modeled gravity anomalies (shown as a solid dots in Figure 2a) at the end of the 39th iteration closely fit the observed ones. A maximum error of 0.044 mGal between the observed and modeled gravity anomalies is observed exactly at the 36th km on the profile (Figure 3a). The value of J had reduced drastically from its initial value of 3550019 mGal^2 to 1.43 at the end of the 34th iteration and then to 0.001 at the end of the concluding iteration (Figure 3b). The estimated density parameters and coefficients of the 2nd degree polynomial from the inversion are given Table 1 and Table 2 and shown graphically in Figure 2c (dashed line) and 2b (solid line) respectively. The errors (%) between the assumed and estimated densities are given in Table 1. Further, the changes in each estimated parameter (densities and coefficients of the 2nd degree polynomial) against the iteration number are shown in Figure 3b.

It is to be noted from Figure 2b that the modeled fault plane by a 2nd degree polynomial marginally deviates from the assumed fault plane described by a 6th degree polynomial.

The estimated densities (Table 1 and Figure 2c) pertaining to two sedimentary pulses at different depths are marginally overestimated, whereas the densities of compact and vesicular basalts are slightly underestimated. Such an error between assumed and estimated densities is acceptable considering the presence of significant level of pseudorandom noise in the anomalies produced by the structure. Therefore, the fault plane whether it is described by a 2nd degree or a 6th degree does not appreciably affect the fault plane geometry and estimated densities of the structure.

Inversion of noisy anomalies to estimate depths and fault plane geometry

The inversion process is repeated to estimate the depths of the four concealed density interfaces and three coefficients of the polynomial by keeping the density parameters unchanged. In this case, the initial depths assigned to four density interfaces are given in Table 3 and shown in Figure 4c (dotted lines). The initial depths of the density interfaces are significantly different from the assumed/true

Figure 3. (a) Error analysis between the observed and modeled gravity anomalies, (b) Changes in misfit, coefficients of a 2nd degree polynomial, and densities of subsurface formations against the iteration number.

Table 3. Assumed and estimated depths to density interfaces, synthetic example.

Interface	Assumed depth (km)	Initial depth (km)	Estimated depth (km)	Error (%)
Compact basalt/sediments	3.5	1.5	3.44	1.71
Sediments/ Vesicular basalt	5.0	3	4.8	4.0
Vesicular basalt/compact sediments	8.0	5	7.6	5.0
Compact sediments/basement	10.0	8	9.57	4.3
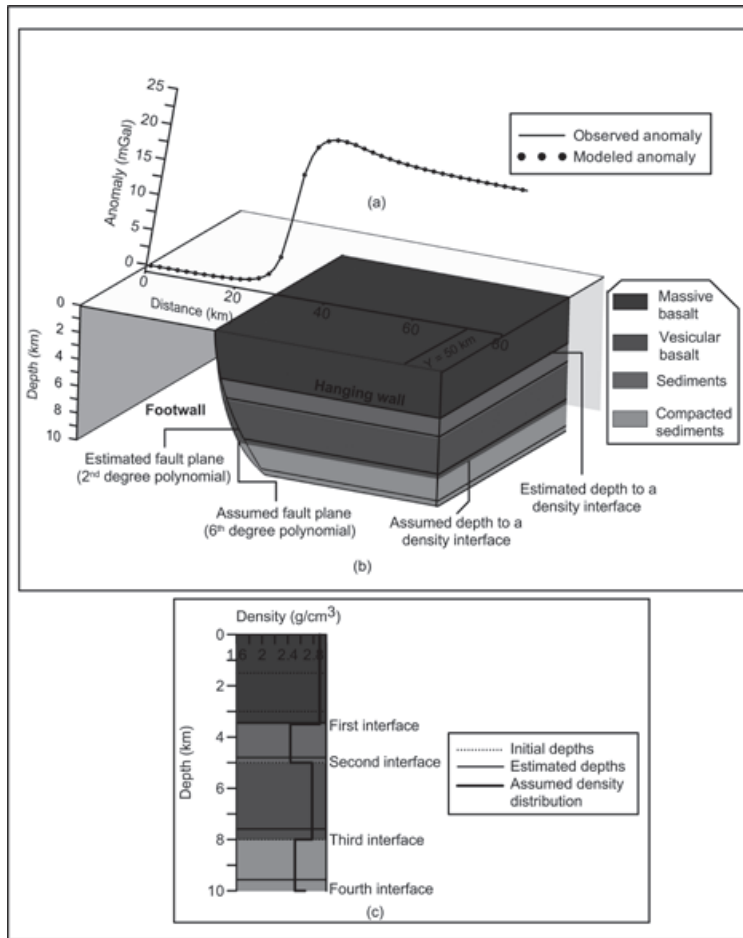
Figure 4. (a) Observed and modeled noisy gravity anomalies, (b) four layered hanging wall system of synthetic listric fault source with assumed and modeled fault planes described by 6th and 2nd degree polynomials, (c) assumed and estimated depths to density interfaces. Densities of the formations (shown as step line) are remain unchanged during inversion.

model parameters. As in the previous case, the approximate location of the fault plane identified by the algorithm at 30.07 km was assigned to the first coefficient of the polynomial, f_0, whereas the other coefficients were set to zero. For such an inversion, the algorithm took 45 iterations before it got terminated. The misfit, J, had reduced from its initial value of 45565.3 mGal^2 for the starting model to 0.7 at the end of 19th iteration and then slowly to 0.004 mGal at the end of the 45th iteration (Figure 5a). No appreciable changes in estimated depths and coefficients of the polynomial are found beyond the concluding iteration (Figure 5b).

The fit between the observed (solid line in black in Figure 4a) and modeled gravity anomalies at the end of the 45th iteration (solid dots in Figure 4a) is satisfactory. The estimated depths to the four density interfaces are given in Table 3 and shown graphically in Figures 4b and 4c (solid lines). The estimated coefficients of the 2nd degree polynomial to describe the fault plane are given in Table 2 and shown in Figure 4b. By and large, the modeled fault plane (simulated by a 2nd degree polynomial)

closely mimics the assumed one described by a 6th degree polynomial (Figure 4b). In this case, a maximum error of -0.022 mGal between the observed and modeled gravity anomalies is observed at the 40th km on the profile (Figure 5a). The changes in the modeled parameters (depths to density interfaces and coefficients of the 2nd degree polynomial) against the iteration number are shown in Figure 5b.

It is to be noted from Table 3 and Figure 4c that the estimated depths to the four density interfaces are marginally underestimated, with a maximum error of 5% found at the interface between vesicular and compact sediments. However, such an error between the assumed and estimated parameters is acceptable considering the presence of significant level of noise in the anomaly of the structure.

In short, the fault plane whether it is described by a 2nd degree or a 6th degree does not appreciably affect the estimated densities or depths of the formations within the hanging wall of the structure. However, the choice of a 2nd degree polynomial in the inversion would
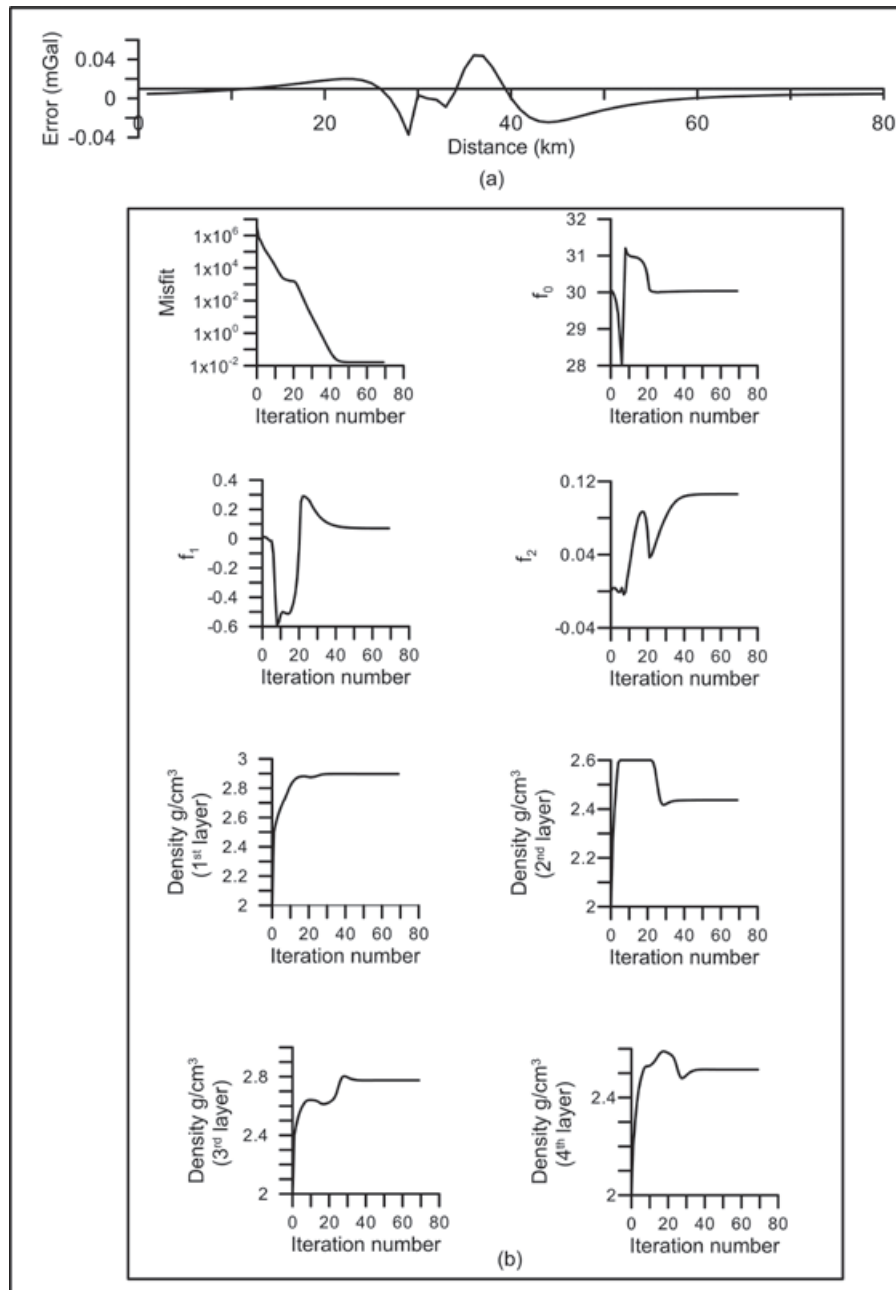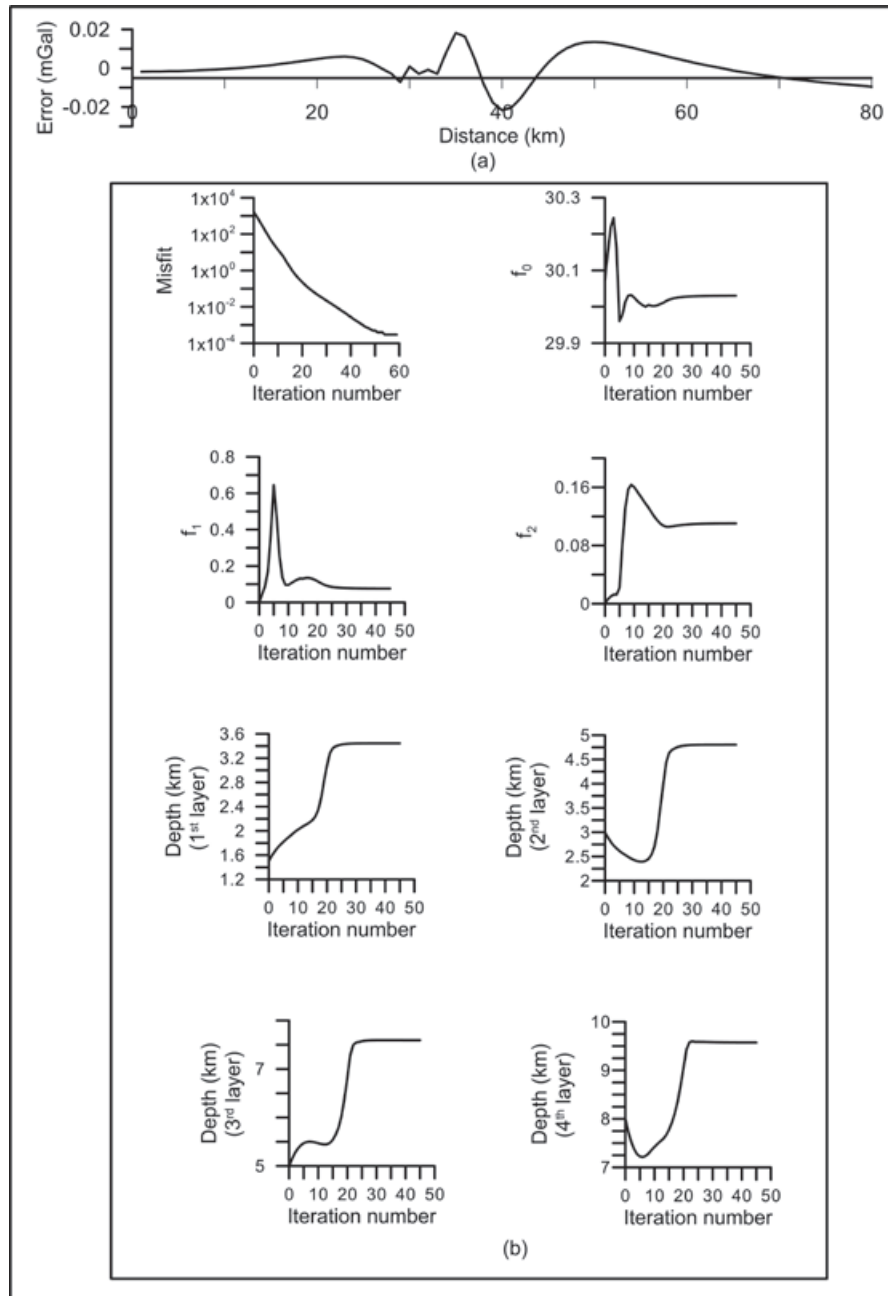
Figure 5. (a) Error analysis between the observed and modeled gravity anomalies, (b) changes in misfit, coefficients of a [2nd] degree polynomial, and depths of various density interfaces against the iteration number.

lead to slightly underestimate the amount of extension across normal fault when the anomalies are analyzed to estimate the depths of the density interfaces.

Field example

The proposed inversion technique is applied to analyze the gravity anomalies observed across the Aswaraopet master fault of the Chintalpudi sub-basin in India. The interpreted results are compared with previously reported information derived from seismic refraction studies (Kaila *et al.*, 1990).

The Chintalpudi sub-basin represents the southeasterly continuation of the Pranhita–Godavari valley. Archaean gneisses (mean density 2.67 g/cm³) form the basement for the Gondwana sequence within the sub-basin

and towards the east the basin margin is associated with the well-known Aswaraopet master fault, which is exposed at the surface and strikes NNW–SSE over a length of 20 km (Figure 6a). Kaila *et al.* (1990) have carried out Deep Seismic Sounding (DSS) investigations along a profile across the basin connecting Kallur and Polavaram (Figure 6a). The Oil and Natural Gas Corporation Ltd. (ONGC), India drilled a borehole (Figure 6a and 6c) within the basin and encountered Archaean basement at a depth of 2.935 km (Agarwal, 1995). The density contrast-depth data measured from this borehole is shown in Figure 6b (Chakravarthi, 2003). The gravity anomaly of the basin (Figure 6c) was analyzed by Chakravarthi and Sundararajan (2007) for its basement structure using a 3D inversion.

For the present study, the gravity anomalies of the basin along a profile, EE', (Figure 6a and 6c) across the Aswaraopet master fault have been analyzed using the present algorithm. This profile also forms part of the DSS profile (Figure 6a). The observed gravity anomaly along the selected profile is shown as solid

dots in Figure 7a. As in the case of synthetic example, we subject the anomaly for inversion in two ways. In either case, the fault plane is described with a 2nd degree polynomial in the inversion. The initial/approximate parameters pertaining to densities (in case of inversion performed for estimating densities and polynomial coefficients) and depths (in case of inversion performed for estimating depths and polynomial coefficients) are given in Table 4 and Table 6 and shown in Figure 7c and Figure 9c (dotted lines) respectively. Although the measured density-depth data of the basin is available, we presume different values for the parameters in the inversion to study whether the estimated parameters after the inversion mimic the measured ones or not. One can notice from Figure 7c and Figure 9c that the assumed initial parameters are significantly different from the measured quantities. The algorithm had identified the approximate location of the fault plane at 2.13 km in each case. Initially, this value was assigned to the first coefficient, f_0, of the polynomial in either case whereas the other coefficients were set to zero.
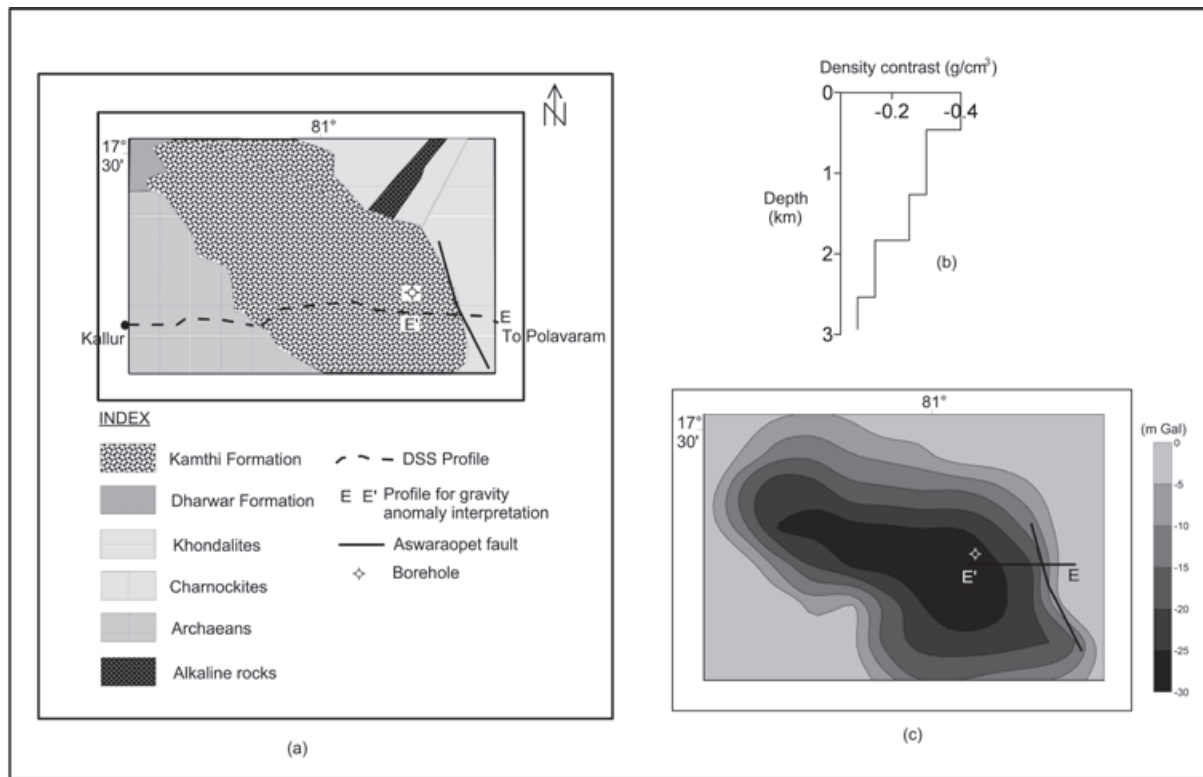
Figure 6. a) Geology of the Chintalpudi sub-basin, India (modified after Kaila *et al.* 1990), (b) measured density contrast-depth data (Chakravarthi, 2003), (c) gravity anomaly map of the Chintalpudi sub-basin, India (after Chakravarthi and Sundararajan, 2007).

Table 4. Measured and estimated densities, Chintalpudi subbasin, India.

Formation	Measured density (g/cm³)	Initial density (g/cm³)	Estimated density (g/cm³)	Error (%)
1	2.27	2.0	2.279	0.396
2	2.37	2.0	2.380	0.422
3	2.42	2.0	2.410	0.410
4	2.52	2.0	2.517	0.119
5	2.57	2.0	2.562	0.311

Table 5. Estimated coefficients of the polynomial, $\zeta(z)$, Chintalpudi subbasin, India.

Coefficient	Estimated coefficients of the 2nd degree polynomial in case of densities and fault plane inversion	Estimated coefficients of the 2nd degree polynomial in case of depths and fault plane inversion
f_0	1.606	1.564
f_1	-0.149	0.143
f_2	0.719	0.506

Table 6. Measured and estimated depths to density interfaces, Chintalpudi subbasin, India.

Formation	Measured depth (km)	Initial depth (km)	Estimated depth (km)	Error (%)
1	0.46	0.2	0.43	6.5
2	1.265	0.9	1.10	13.0
3	1.835	1.2	1.87	1.9
4	2.54	2	2.33	8.3
5	2.935	2.5	3.01	2.5

The algorithm had performed 74 and 14 iterations in each case before terminating. The estimated parameters remained more or less unchanged beyond respective concluding iterations (Figure 8b and Figure 10b). The modeled gravity anomalies are shown in Figure 7a and Figure 9a as solid lines. The fit between the observed and modeled gravity anomalies in either case is satisfactory (Figure 7a and Figure 9a). A maximum error of 0.58 mGal between the observed and modeled gravity anomalies is observed at 6.3 km on the profile (Figure 8a) when the inversion is performed to estimate the densities and fault plane geometry. On the other hand, a maximum error of 0.64 mGal is observed at the 10th km (Figure 10a) when the anomalies are inverted for depths and fault plane geometry. The estimated density and depth parameters subsequent to respective inversions are given in Table 4 and Table 6 and shown in Figure 7c and Figure 9c respectively. The errors (%) between the estimated and measured parameters in each case are also given in Tables 5 and 6. When the anomalies are subjected for inversion to estimate densities and the fault plane geometry, the modeled densities of the first and second formations are slightly overestimated (~0.4%) while others marginally underestimated (Table 4 and Figure 7c). When the inversion was performed for estimating both depths and fault plane geometry simultaneously, the modeled depths of the first, second and fourth density interfaces are modestly underestimated whereas the third and fifth density interfaces are slightly overestimated (Table 6 and Figure 9c). The changes in the estimated parameters with the iteration number in each case are shown in Fig. 8b and Figure 10b respectively.

The modeled fault plane of the structure in each case from the estimated coefficients of the 2nd degree polynomial (Table 5) is shown graphically in Figure 7b and Figure 9b. The

Figure 7. (a) Observed and modeled gravity anomalies, (b) inferred fault plane geometry of the Aswaraopet master fault, Chintalpudi subbasin, India, (c) assumed, initial and modeled densities. Depths of density interfaces are fixed during inversion.

Table 7. Coefficients of the 5th degree polynomial, $\zeta(z)$, used to describe the geometry of the Aswaraopet fault plane derived from DSS studies (after Kaila *et al.*, 1990).

f_0	1.852063529
f_1	-0.6020069478
f_2	-0.6020069478
f_3	0.516508814
f_4	-1.085574722
f_5	0.25061682

estimated location of the fault plane in either case from gravity modeling closely matches with the one mapped from geological studies. Furthermore, the inferred structure of the basin across the Aswaraopet fault from DSS studies (after Kaila *et al.* 1990) is also shown in Figure 9b for comparison. The theoretical gravity response of this structure is shown as a dashed line in Figure 9a along with the observed anomaly. In this case, a 5th degree polynomial with a set of six coefficients (Table 7) completely defines the geometry of the fault plane inferred from DSS studies. The forward modeling algorithm of Chakravarthi (2010b) is used to calculate the gravity anomalies of the structure (derived from seismic data interpretation) using the measured density-depth data (Figure 6b) of the basin. It can be seen from Figure 9a that the modeled gravity anomalies of the structure from present inversion closely mimic the observed ones, whereas the gravity response of the seismically derived structure (Kaila *et al.*, 1990) does not. In addition, the large gradient (4.5 mGal/km) in the observed anomaly between 0 and 6th km across the fault plane does not agree well with the interpretation model of Kaila *et al.* (1990), whereas it agrees reasonably well with the present gravity inversion result.

Figure 8. (a) Error analysis between the observed and modeled gravity anomalies across the Aswaraopet master fault, Chintalpudi subbasin, India, (b) Changes in misfit, coefficients of a 2nd degree polynomial, and densities of subsurface formations against the iteration number.

The structure inferred from DSS investigations (Figure 9b) shows high angle dip for the fault plane from the surface to a depth of about 0.6 km, then moderately varying dips up to 1.7 km beyond which it transforms again into a high angle normal fault. The present interpretation reveals that the fault plane (Figure 7b and Figure 9b), which dips at high angle near the surface, shows similar dips up to a depth of 1.7 km beyond which it shows moderate dips. Further, the error (4.6%) between the measured and estimated thickness of the basin from DSS studies near the existing deep borehole is relatively more than the one estimated (2.55%) from the present inversion.
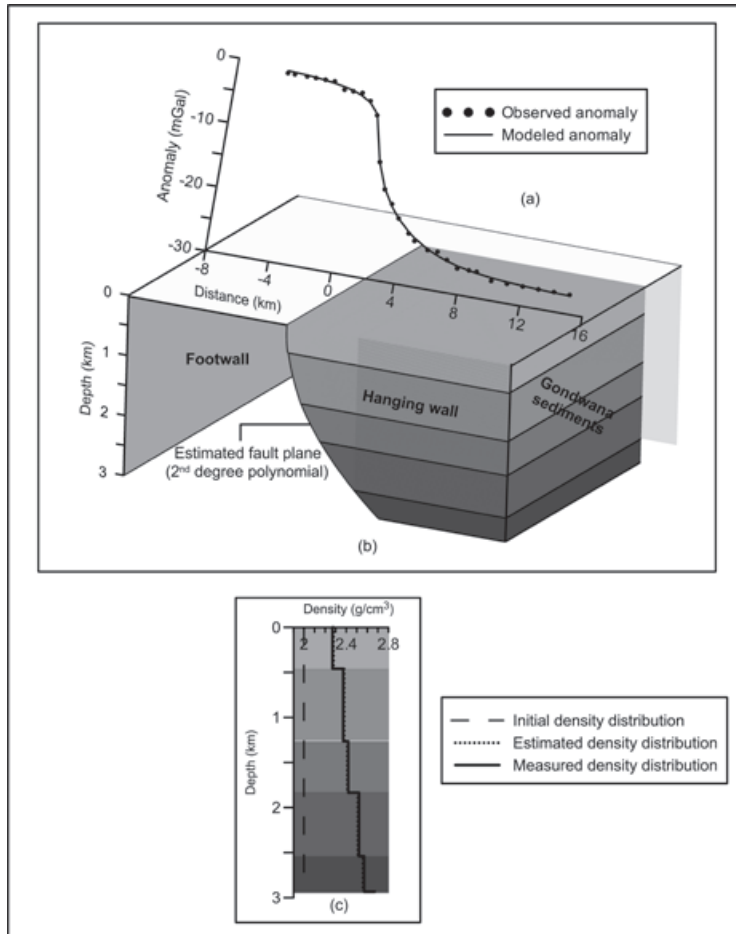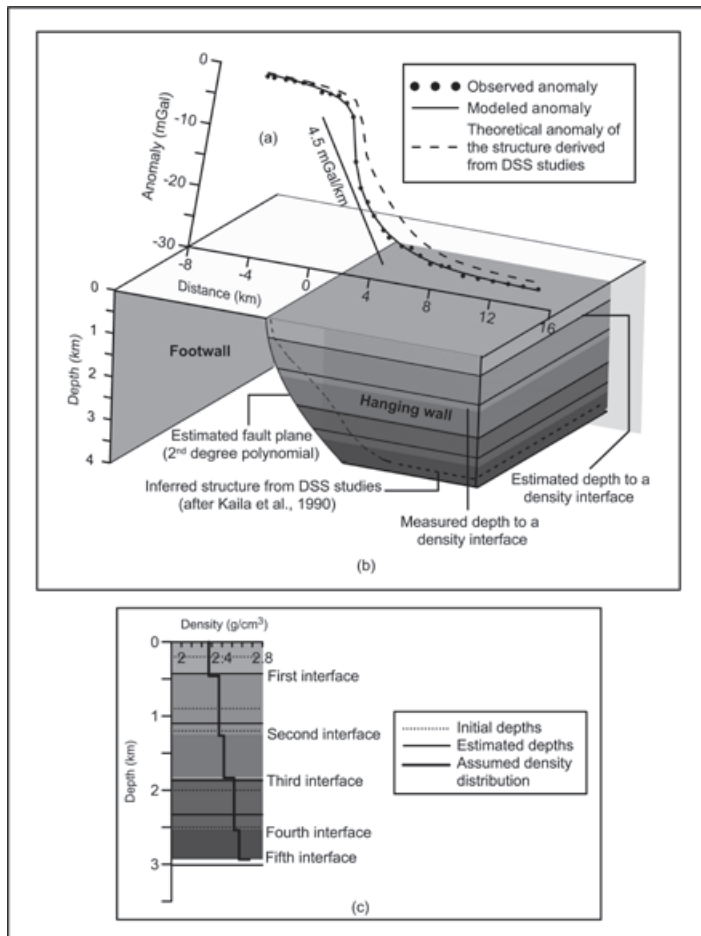
Figure 9. (a) Observed and modeled gravity anomalies, (b) inferred fault plane geometry of the Aswaraopet master fault, Chintalpudi subbasin, India. Anomalies are analyzed to estimate the depths of density interfaces.

Conclusions

A gravity inversion technique using ridge regression is presented to analyze the gravity anomalies of strike-limited listric fault sources, where the detached hanging wall of the structure consists in several geologic formations; each one possessing its own density and thickness. The fault plane is described with a polynomial function of arbitrary but specific degree. This algorithm simultaneously estimates the geometry of a fault plane and the parameters pertaining to either densities or depths of various subsurface formations from the observed gravity anomalies. The advantage of the algorithm is that it can be used to analyze the gravity anomalies of the structure even when the profile along which the interpretation is intended fails to bisect the fault plane.

The algorithm is applied to both synthetic and real field gravity anomalies. In case of synthetic example; significant level of pseudorandom noise was added to the gravity anomalies produced by a structure, whose

fault plane was described with a 6th degree polynomial. To study the effect of the choice of the degree polynomial in the interpretation, the noisy anomalies were inverted presuming a 2nd degree polynomial for the fault plane. The noisy anomalies were then analyzed to estimate i) the densities and fault plane geometry, keeping the depths of density interfaces unchanged, and ii) depths and fault plane geometry, keeping densities intact. In either case, the estimated parameters pertaining either to densities or depths closely mimic the assumed parameters. However, the choice of the lower order polynomial (such as a 2nd degree) would lead to marginally underestimate the amount extension across the normal fault, when inversion is performed to estimate the fault plane geometry and depths of density interfaces.

The observed gravity anomalies across the Aswaraopet master fault from the eastern margin of the Chintalpudi subbasin in India are analyzed by the proposed technique and found that the estimated parameters (densities
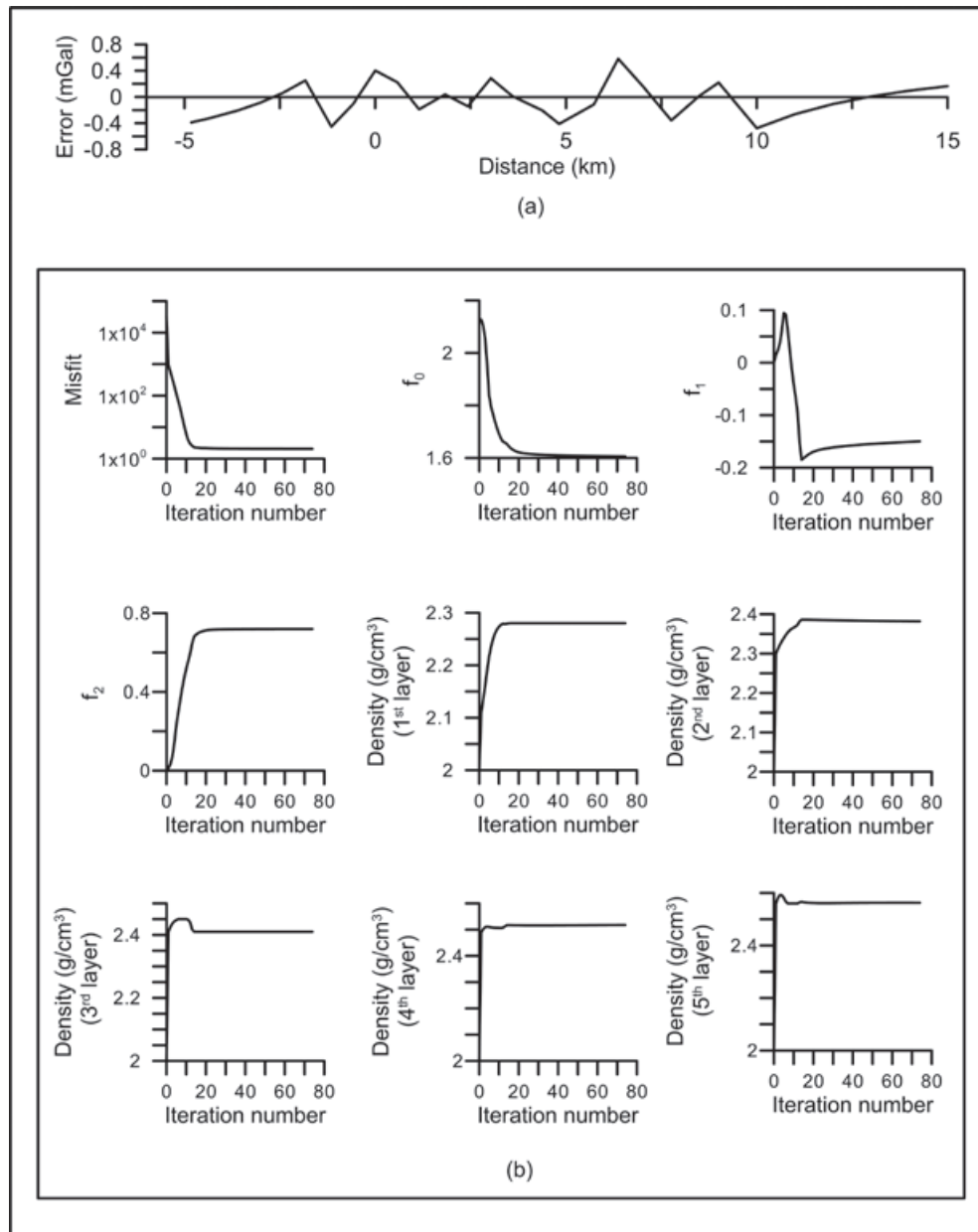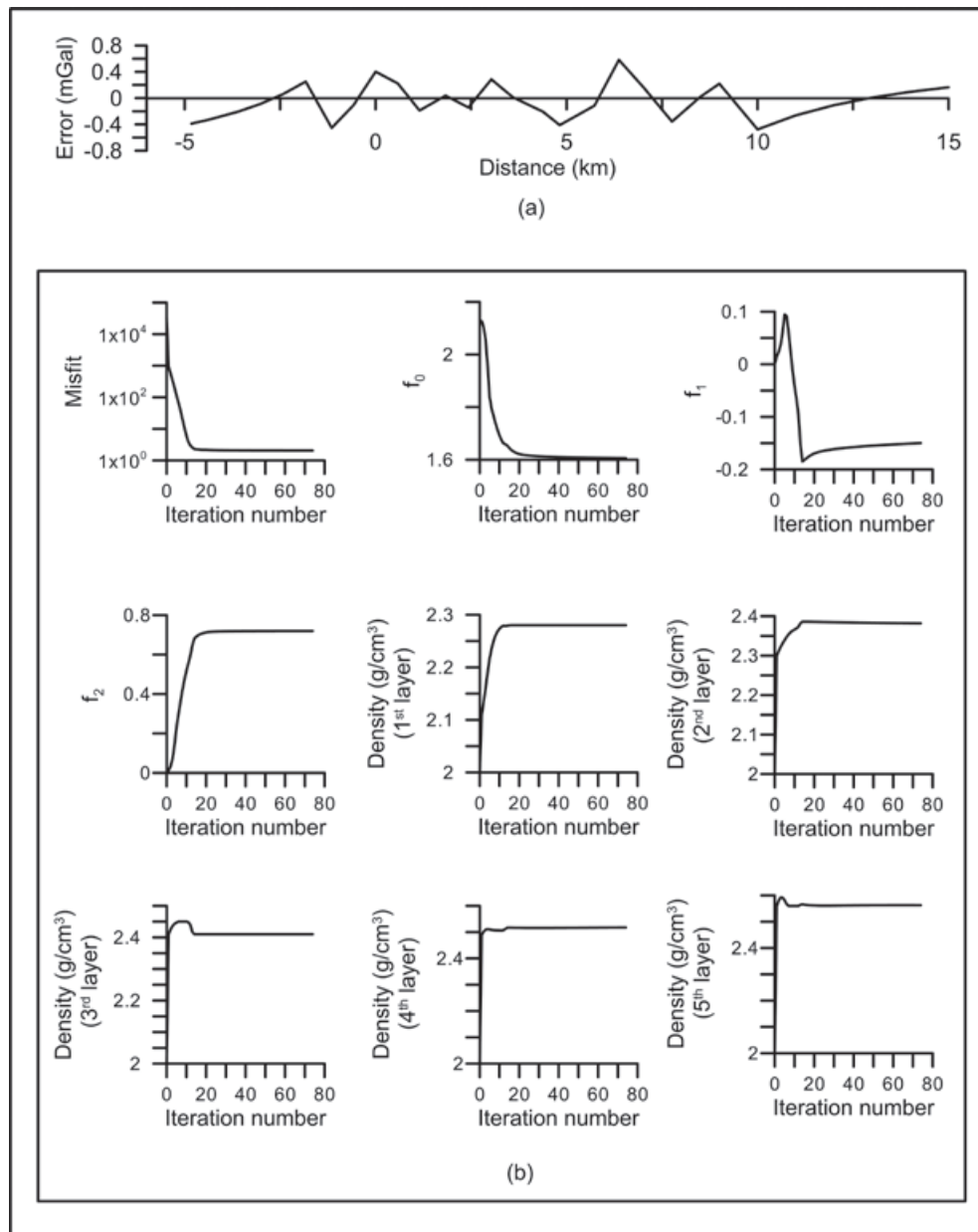
Figure 10. (a) Error analysis between the observed and modeled gravity anomalies across the Aswaraopet master fault, Chintalpudi subbasin, India, (b) changes in misfit, coefficients of a 2nd degree polynomial, and depths to various density interfaces against the iteration number.

and thicknesses of subsurface formations within the hanging wall) from independent gravity inversion reasonably coincide with the measured ones. On the other hand, the calculated gravity response of the structure derived from seismic data interpretation (Kaila *et al.* 1990) using the measured density-depth data significantly deviates from the observed anomaly. Further, the large gradient in the observed gravity anomaly over the fault plane is better explained by the gravity inversion

model rather than the one reported from seismic data interpretation (Kaila *et al.*, 1990).

However, the proposed inversion technique presumes that the detached hanging wall of listric fault morphology consists in several geologic formations with each one bounded on top and bottom by flat surfaces, which in reality may or not be valid. Therefore, the inversion technique is more effective when the assumptions are relatively valid.

References

Agarwal B.P., 1995, Hydrocarbon prospects of the Pranhita-Godavari graben, India. *Proceedings of Petrotech.* 95, 115–121.

Abdelrahman E.M., Bayoumi A.I., El-Araby H. M., 1989, Dip angle determination of fault planes from gravity data. *Pure and Applied Geophysics,* 130, 4, 735-742.

Abdelrahman E.M., El-Araby H.M., El-Araby T.M., Abo-Ezz E.R., 2003, A least-squares derivatives analysis of gravity anomalies due to faulted thin slabs. *Geophysics*, 68, 535-543.

Adriasyah A., McMechan A.G., 2002, Analysis and interpretation of seismic data from thin reservoirs: Northwest Java basin, Indonesia. *Geophysics,* 67, 14-26.

Brady R., Wernicke B., Fryxell J., 2000, Kinematic evolution of a large-offset continental normal fault system; South Virgin Mountains, Nevada. *Geological Society of America Bulletin* 112, 1375-1397.

Chakravarthi V., Ramamma B., (2013), Gravity anomaly modeling of multiple geological sources having different strike lengths and arbitrary density contrast variations. *Near Surface Geophysics,* 11*,* 4, 363-370.

Chakravarthi V., 2011, Automatic gravity optimization of 2.5D strike listric fault sources with analytically defined fault planes and depth-dependent density. *Geophysics,* 76, I21-I31.

Chakravarthi V., 2010, Gravity anomalies of strike limited listric fault sources with analytically defined fault planes and arbitrary density contrast variations with depth. *Near Surface Geophysics,* 8, 279-286.

Chakravarthi V., 2003, Digitally implemented method for automatic optimization of gravity fields obtained from three-dimensional density interfaces using depth dependent density. *United States Patent,* 6,615,139.

Chakravarthi V., Sundararajan N., 2007, 3D gravity inversion of basement relief – A depth dependent density approach. *Geophysics,* 72, I 23- I 32.

Chakravarthi V., Sundararajan N., 2006, Gravity anomalies of multiple prismatic structures with varying density - A Marquardt inversion. *Pure and Applied Geophysics,* 163, 229-242.

Chakravarthi V., Sundararajan N., 2004, Ridge regression algorithm for gravity inversion of fault structures with variable density. *Geophysics,* 69, 1394–1404.

Chakravarthi V., Singh S.B., Ashok Babu G., 2001, INVER2DBASE - A program to compute basement depths of density interfaces above which the density contrast varies with depth. *Computers & Geosciences,* 27, 1127–1133.

Essa K.S., 2013, Gravity interpretation of dipping faults using the variance analysis method. *Journal Geophysics and Engineering,* 10, 015003.

Goussev S., Charters R., Peirce J., 2006, Mackenzie Delta: A case of one residual gravity anomaly and 16 dry exploration wells. 2006 CSPG/CSEG/CWLS Joint Conference, 15–18 May, Calgary, Canada, Expanded Abstracts, 435–439.

Gómez-Ortiz D., Tejero-López R., Babín-Vich R., Rivas-Ponce A., 2005, Crustal density structure in the Spanish Central System derived from gravity data analysis (Central Spain). *Tectonophysics*, 403, 131–149.

Kaila K. L., Murthy P. R. K., Rao V. K., Venkateswarlu N., 1990, Deep seismic sounding in the Godavari Graben and Godavari (Coastal) Basin, India. *Tectonophysics,* 173, 307-317.

Marquardt D. W., 1970, Generalized inverses, ridge regression, biased linear estimation, and nonlinear estimation. *Technometrics*, 12, 591-612.

Martín-Atienza B., García-Abdeslem J., 1999, 2-D gravity modeling with analytically defined geometry and quadratic polynomial density functions. *Geophysics,* 64, 1730–1734.

Maxant J., 1980, Variation of density with rock type, depth, and formation in the Western

Canada basin from density logs. *Geophysics,* 45, 1061–1076.

McKenzie D., 1978, Some remarks on the development of sedimentary basins. *Earth and Planetary Science Letters*, 40, 25-32.

McKenzie D., Jackson J., 2012, Tsunami earthquake generation by the release of gravitational potential energy. *Earth and Planetary Science Letters,* 345-348, 1-8.

Moral C. R., Gómez Ortiz D., Tejero R., 2000, Spectral analysis and gravity modelling of the Almazán basin (Central Spain). *Journal of the Geological Society of Spain,* 13, 131-142.

Murthy I.V.R., Krishnamacharyulu S.K.G., 1990, Automatic inversion of gravity anomalies of faults. *Computers & Geosciences,* 4, 539–548.

Nagihara S., Hall S.A., 2001, Three-dimensional gravity inversion using simulated annealing: constraints on the diapiric roots of allochthonous salt structures. *Geophysics,* 66, 1438-1449.

Peirce J.W., Lipkov L., 1988, Structural interpretation of the Rukwa rift, Tanzania. *Geophysics,* 53, 824–836.

Rao D.B., 1985, Analysis of gravity anomalies over an inclined fault with quadratic density function. *Pure and Applied Geophysics,* 123, 250-260.

Rao M. M. M., Murthy T.V.R., Murthy K.S.R., Vasudeva R.Y., 2003, Application of natural generalized inverse technique in reconstruction of gravity anomalies due to a fault. *Indian Journal of Pure and Applied Mathematics,* 34, 31-47.

Rybakov M., Goldshmidt V., Fleischer L., Ben-Gai Y., 2000, 3-D gravity and magnetic interpretation for the Haifa Bay area (Israel). *Journal of Applied Geophysics,* 44, 353–367.

Stavrev P., Reid A., 2010, Euler deconvolution of gravity anomalies from thick contact/fault structures with extended negative structural index. *Geophysics,* 75, I51-I58.

Sundararajan N., Ramabrahmam G., 1998, Spectral analysis of gravity anomalies caused by slab-like structures: A Hartley transform technique. *Journal of Applied Geophysics,* 39, 53–61.

Thanassoulas C., Tselentis G.A., Dimitriadis K., 1987, Gravity inversion of a fault by Marquardt's method. *Computers & Geosciences,* 13, 399–404.

Toushmalani R., 2013, Gravity inversion of a fault by particle swarm optimization. SpringerPlus, 2:315.

Evaluation of local groundwater vulnerability based on DRASTIC index method in Lahore, Pakistan

Akhtar Malik Muhammad, Tang Zhonghua*, Ammar Salman Dawood and Bailey Earl

Resumen

La evaluación de la vulnerabilidad de las aguas subterráneas muestra una extrema sensibilidad a los contaminantes antropogénicos in situ. A partir de una evaluación dicotómica (inter alia) de las características geológicas e hidrológicas fue posible determinar la vulnerabilidad de un acuífero. Se precisó que la capacidad de carga natural del acuífero puede verse seriamente comprometida con determinadas actividades humanas. La estructura y el material de la composición física de los acuíferos muestra resistencia al transporte de contaminantes desde la superficie hasta la capa freática. En la actualidad, se han planteado numerosos métodos para evaluar la vulnerabilidad del acuífero. El modelo DRASTIC utiliza algoritmos informáticos y datos hidrogeológicos dentro de un entorno de Sistema de Información Geográfica (GIS, por sus siglas en inglés) para calcular la vulnerabilidad.

El grado de vulnerabilidad de cada parámetro puede evaluarse mediante el cálculo del análisis de sensibilidad del índice DRASTIC, utilizando GIS, y muestra la contribución de cada uno de estos parámetros. El GIS se utilizó para la elaboración del mapa, el cual muestra una alta zona de riesgo del 28,8%, zonas moderadamente vulnerables del 46,3% y zonas de riesgo del 10,4%. Dentro del área de estudio, las regiones centrales mostraron una baja vulnerabilidad debido a la densidad de asentamientos humanos y el bajo nivel de agua. Sin embargo, las tierras de tipo pastos y áreas agrícolas registraron un alto riesgo.

El desarrollo ambiental y socioeconómico de Lahore depende de los políticos y los desarrolladores, y de capacidad de utilizar la información de manera efectiva para la toma de decisiones. El mapa de vulnerabilidad de las aguas subterráneas proporciona una base y está enfocada a la protección del acuífero de contaminantes. Además, el uso del suelo y las actividades de desarrollo pueden ser reportados por las variables de asignación, lo que demuestra que las zonas industriales y agrícolas son altamente vulnerables comparados con las zonas de asentamiento.

Palabras clave: Aquífero, modelo DRASTIC, GIS, aguas subterráneas, Lahore, vulnerabilidad.

A. Malik Muhammad
T. Zhonghua*
A. Salman Dawood
School of Environmental Studies
China University of Geosciences
Wuhan 388 Lumo Lu, Wuhan 430074
Hubei Province, China PRC
*Corresponding author: zhhtang@cug.edu.cn
Email: drmmakhtar@cug.edu.cn
        ammar@cug.edu.cn

B. Earl
School of Resource
China University of Geosciences
Wuhan 388 Lumo Lu, Wuhan 430074
Hubei Province, China PRC
Email: earlplanner@hotmail.com

A. Malik Muhammad, T. Zhonghua, A. Salman Dawood and B. Earl

Abstract

Groundwater vulnerability assessment shows an extreme sensitivity to *in situ* anthropogenic pollutants. A dichotomous assessment of geological and hydrological *(inter alia)* characteristics makes it possible to determine the vulnerability of an aquifer. The natural carrying capacity of aquifer can be severely compromised by human activities. The physical structure and material composition of aquifers shows resistance to contaminants transport from surface to water-table. Currently, numerous methods have been posited evaluating aquifer's vulnerability. Similarly the DRASTIC model utilizes computer algorithms and hydro-geological data within a Geographical Information System (GIS) environment to compute aquifer vulnerability. The degree of vulnerability for each parameter can be evaluated by computing sensitivity analysis of DRASTIC index using GIS, showing the contribution of each parameter to vulnerability sensitivity. The GIS was used to developed map which showed high risk area of 28.8% and moderately vulnerable areas of 46.3% while areas of no risk were 10.4%. Central regions within the study area showed low vulnerability due to dense human settlement and low water level. However, pasture type lands and agricultural areas recorded high risk.

Lahore's environmental and socio-economic development is dependent on policy makers and planner's ability to use information effectively for decision making. The resultant groundwater vulnerability map provides a basis for this aimed at protecting the aquifer from pollutants. Additionally, land use and development activities can be informed by mapping variables, showing that industrial and agriculture areas are highly vulnerable as compare to settlement areas.

Key words: aquifer, DRASTIC model, GIS, groundwater, Lahore, vulnerability.

Introduction

In Pakistan, groundwater, is potable in its natural form and accounts for approximately ninety seven percent of total rural water supply, while nationally, accounting for fifty three percent of potable water (Solley, 1988). Groundwater is considered an important supply source for portable water, due to its relatively low susceptibility to pollution, inter alia, in comparison to surface water (United State Environmental Protection Agency, 1985). Unlike surface water that requires various pretreatment methods for domestic use, groundwater, in many cases, required little or no treatment, depending on the level of contamination. Unfortunately, both human settlement development (demographic dynamics, ignorance, improper watershed and waste management, advanced agricultural production and industrial activities etc) and physical conditions within the geological setting of most groundwater resources, threaten to compromise its quality and quantity. This relationship between groundwater quality and quantity and human settlement activities is further explored by (Baalousha, 2010), who associated contamination conditions with socioeconomic development. Public health and safety are threatened by groundwater and surface water contamination due to increases pressures from settlement development, in particular urbanisation and indiscriminate rural agricultural practices; hence, quality monitoring and conservation is essential (Baalousha, 2010).

The geological sensitivity of groundwater aquifer is defined as the possibility of percolation and diffusion of contaminants from the surface, due to run-off, into the groundwater system (Evans and Myers, 1990). One of the approaches most widely used to protect groundwater quality consists of assessing and mapping the levels of contamination to which it is susceptible. This approach is relatively old, since its first application date back to the 1970s (Albinet and Margat, 1970). The accompanying mapping exercise is undertaken on factors related to the physical environment: soil, unsaturated zone, and topology of the aquifer. Conventional methods (i.e. DRASTIC model (Aller, 1987) or the GOD model (Foster, 1987), AVI and SINTACS etc) are able to distinguish varying degrees of vulnerability at regional scales where different lithologies exist (Vias, et al., 2005). However, the most popular of these is the DRASTIC, which is an acronym of seven hydro-geological parameters which helps in defining groundwater regime and its vulnerability towards pollution. The parameters are; depth to aquifer (D), recharge (R), aquifer media (A), soil type (S), topography (T), vadose zone (I), and hydraulic conductivity (C).

The resulting thematic maps of each parameter are generated within a GIS environment. Similarly, combining DRASTIC and GIS is an efficient methods to assess groundwater vulnerability, while simultaneously assisting with its management (Babiker, et al., 2005). Each parameter in the DRASTIC model has been assigned different weight and rating

value ranging from 1 to 10 based on its relative contribution to groundwater pollution. Initially developed by the US Environmental Protection Agency (USEPA) by Aller (Aller, 1987), the DRASTIC approach has now got several regional applications (Al-Zabet, 2002, Baalousha, 2006, Jamrah, et al., 2008, Merchant, 1994).

Some applications modified the DRASTIC method by adding different parameters (Secunda, et al., 1998, Wang, 2007) such as land use index, lineaments, aquifer thickness, and impact of contaminant. Still others, (Panagopoulos, et al., 2006, Secunda, Collin and Melloul, 1998), added more parameters or replacing some parameters to produce good results, such as land use index or aquifer thickness. A computer software (i.e. AHP-DRASTIC) developed by Thirumalaivasan et al., (2003) derive ratings and weights of modified DRASTIC model parameters (Thirumalaivasan, et al., 2003). Hui introduced an OREADIC model during a study in the Yinchuan Plain of China, which contains characteristics of DRASTIC model (Qian, et al., 2011). The GA-Ridge (genetic algorithm) model was developed and applied to determine the most effective hydro-geological factors influencing aquifer vulnerability(Ahn, et al., 2011). Map scales less than 1:50,000 can be assessed by using Overlay and index methods and statistical methods; however larger map scales are used in methods based on simulation models. Intrinsic aquifer vulnerability can be assessed using overlay and index methods and statistical methods. However process-based simulation models are popular for assessing specific vulnerability (Bazimenyera and Zhonghua, 2008). Parameters can be applied in Index and Overlay methods to assess groundwater vulnerability (Samake, et al., 2011).

The current paper, investigated groundwater vulnerability by modifying the DRASTIC model using GIS on the unconfined aquifer at Lahore City in Pakistan. Lahore is a totally groundwater dependent city. Therefore, it is important to identify vulnerable and expected contaminants infiltration areas. Sensitivity analysis is calculated to evaluate the model parameters. Four categories of groundwater vulnerable zones of contamination were identified. While the substantive aim of this study was to prepare groundwater vulnerability map, the more general objectives was to use the maps to assist with making informed decision on groundwater resources management, identifying and classifying contaminants and their sources, identify and classifying the intrinsic properties of the aquifer that aids in groundwater quality maintenance and identifying other factors contributing to groundwater contamination and degradation. These objectives and aim will eventually assist in decision at both the policy and planning levels to boost quality and quantity standards. As the second largest city of Pakistan, Lahore is adversely affected by uncontrolled urbanisation. Thus, it is necessary to identify the effects of these various developments on the city's groundwater resources, and find solution to reduce the stress on the aquifer.

Study area

Lahore City is located between 31^0-15' and 31^0-42' north latitude, 74^0-01' and 74^0-39' east latitude. Having an altitude ranging from 208m to 213m ASL, it is located on the alluvial plain of the left bank of Ravi River. Lahore is bordered northerly and westerly by the district of Sheikhupura, easterly by India (international border) and southerly by Kasur district (Figure 1). With a population of over 6.5million inhabitants in 2007, it is the Provincial Metropolis and the largest urban district of Punjab. It is also the second largest urban centre of Pakistan and considered to be the 24th largest city in the world.

Lahore is characterised by large seasonal variations in temperature and rainfall. Mean annual temperature is approximately 24^0C, ranging from 34^0C in June to 12^0C in January. Average annual rainfall is close to 575mm, varying from 300 to 1200mm (Pakistan Meteorological Department).

Approximately seventy five percent of the annual total rainfall occurs from June to September, contributing approximately 40mm to groundwater recharge in a normal year (NESPAK, 1993:Ref (Gabriel and Khan, 2010)). The annual potential evapotranspiration rate is 1750mm which greatly exceeds the rainfall, making irrigation for agriculture essential to supplement rainfall (NESPAK, 1993:Ref (Gabriel and Khan, 2010)). Daily relative humidity is higher in winter than in summer months. May and June are very hot and dry bringing frequent dust storms. Towards the end of June or beginning of July, the monsoon season starts, which is characterized by torrential rainfall and stifling humidity.

Analysis of urban demographic dynamics shows that Lahore in being metropolised to rival Punjab Province, which grew at a faster rate than the overall increase in population of the country. Therefore, water demand is increasing with urbanisation trends. Water and Sanitation Agency (WASA) has installed 316
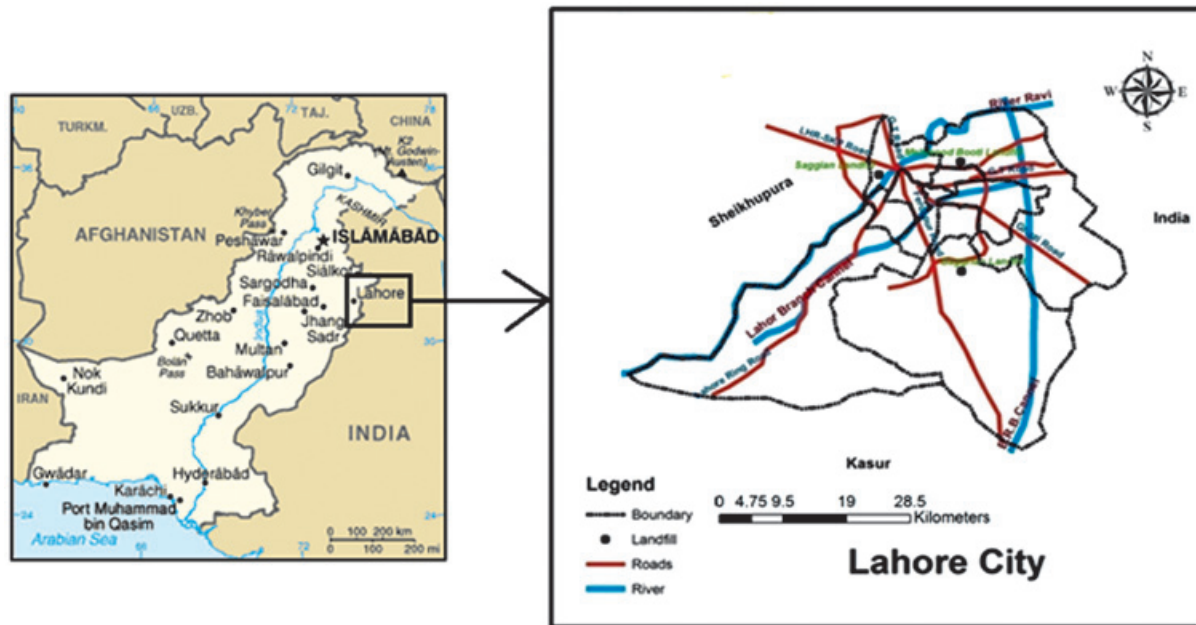
Figure 1. Regional and local location of the study area.

tube wells of varying capacity in Lahore, which operate on an average of 16 - 18 hrs/day. These wells inject water directly into the main water supply system. Consequently, WASA is supplying 15.26 m³/s (290mgd) of water to 4, 31,336 connections. (Gabriel and Khan, 2010).

Geology and hydro-geological characteristics of Lahore aquifer:

The Lahore aquifer, the source of the city's groundwater, is a part of the greater Rechana Doab traversed by the Indus River. The study area is sandwiched between River Ravi and Ravi Chenab. The aquifer is composed additionally of unconsolidated alluvial complex formed by the contemporaneous filling of a subsiding trough resulting in a huge sedimentary complex of more than 400m (1300ft) in thick. Understanding the occurrence and movement of groundwater requires studying specific parts of the aquifer and also the larger contiguous aquifer constituted by the Indus River System. Although not a homogeneous and isotropic aquifer, the fine formations encountered at various depths have localized effect and do not impede the regional movement of groundwater water (NESPAK, 1993:Ref Gabriel and Khan, 2010).

The River Ravi is the main source of recharge to Lahore aquifer. Groundwater flows from a North to South direction with velocity of 1 to 1.5cm/day (Schnoor, 1996), with water level varying from 14m to 43m and dropping

to 0.84m annually, due to increasing city population more water exploitation to fulfill ever increasing water demand in Lahore city (WASA, Lahore). Increasing urban and rural abstractions, for industrial, residential and agricultural uses respectively have caused decline in groundwater levels, especially within urban areas. From 1960-1987, groundwater levels have declined in parts of Lahore city by up to 15m (NESPAK, 1993:Ref Gabriel and Khan, 2010). The flow of the River Ravi is highly variable from 10 to 3000 m³/sec some times during the year.

Clay loam increases gradually with distance from riverbed (Khan, et al., 1990). There are significant changes in lithologies. The chief constituent minerals are quartz, muscovite, biotite and chlorite, in association with small percentages of heavy minerals (Greenman, et al., 1967).

Pollution sources in Lahore:

The high vulnerability of the aquifer to pollution defines the urgency for study to determine the type and nature of pollution. The Hudiara Drain is a major source of pollution for River Ravi. The heavily silted River Ravi, entering Pakistan from India, presently contributed over 47% of total municipal and industrial pollution load discharged into all the rivers in Pakistan. This silt is diluted with agriculture runoff mixing with some industrial pollutants in Pakistan (Sami, 2001).
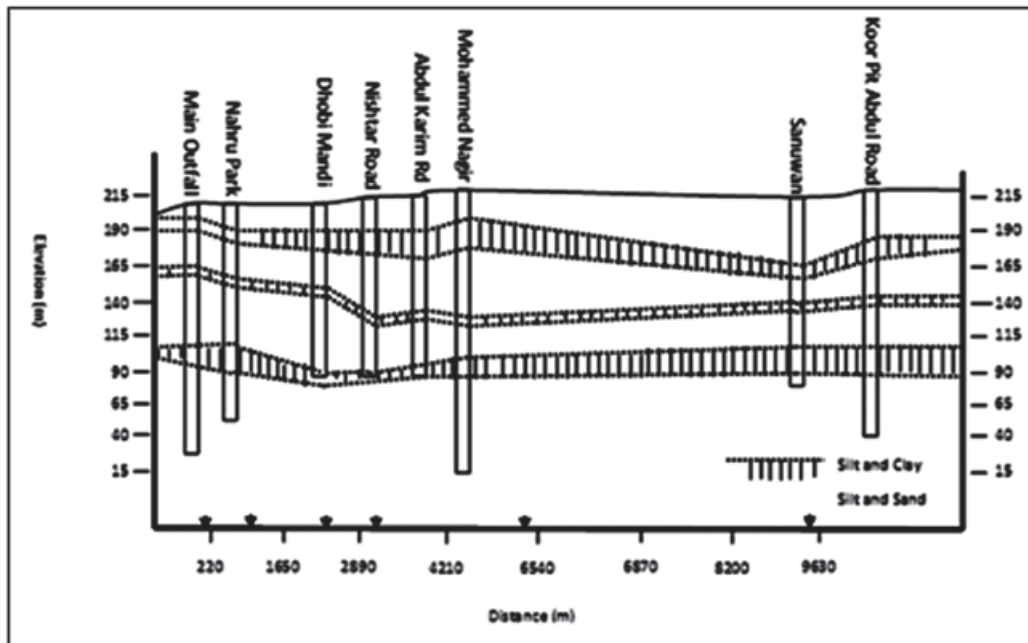
Figure 2. Geological structure of the Lahore aquifer (Source: Niaz, 2005).

Leakage and infiltration from irrigation canals results in a rise in the water table in Lahore. The popular practice of heavy and indiscriminate use of fertilizers and pesticides by farmers, presents a significant source of underground water pollution, as these and other agrochemicals leach from the surface soil (Lapworth, et al., 2006).

Approximately 5,700tonns of solid waste is generated daily in Lahore City from different sources, with up to 67% being organic waste. This is equivalent to a generation rate of 0.84kg/capita/day (Batool and Ch, 2009). Improper disposal from the many sources such as household, commercial activities, industrial, medical waste and animal waste are creating environmental health hazards for citizens (Shimura, et al., 2001) With particular reference to Lahore, ground water is suspected to be polluted (Ahmed, 2010) due to untreated waste water and the three dumping sites located in different parts of city. These landfill sites are informal and unplanned and have no system for leachate collection. Thus they contaminate groundwater. The presence of high levels of fecal coliform in urban underground water, suggests widespread use of improper sewage facilities (Bishop, et al., 1998). Lack of sufficient legislation and enforcement mechanisms in developing countries contributes to contamination and pollution of natural resources (Ghanbari, et al., 2011).

Study methodology

Development of the DRASTIC parameters

Aller (1987) was among the first to develop this groundwater tool in 1987. DRASTIC is an empirical groundwater model that estimates groundwater vulnerability within aquifer systems based on in situ hydro-geological information (Aller, 1987). Parameters vary with study area's geology, hydro-geology, and on data availability, analysis accuracy and development of vulnerability map by using GIS. Each hydro-geological parameter is assigned a weighting, from one to ten (Shamsuddin, 2000), according to its ability to affect groundwater. Each of the seven layers possess the ability contribute towards groundwater vulnerability evaluation (Prasad, et al., 2010). The weighting of the parameters ascribe; 1 - lowest pollution potential to 10- highest pollution potential (Table 1). Land surface, unsaturated zones and saturated zones; are three variables considered in development of DRASTIC model (Naser Ebadati 2012). The system consists of two parts: designation of mapable units and superimposing relative numerical rating system (Padagett, 1994).

The DRASTIC Index was computed by summing the weighted factors of each subdivision of the area. The DRASTIC Index is considered highly authentic and accurate when there is need for comprehensive data

Table 1. Weights given to each DRASTIC Parameter (Aller, 1987).

Parameters	DRASTC Weight
D - Depth to groundwater water: Deep water tables consider safer from pollutants then shallow water tables.	5
R - Annual Recharge: high recharge rate indicates more contamination infiltrate towards groundwater water.	4
A - Aquifer media: the aquifer media determines chances resistance against contaminant transport	3
S - Soil media: the soil media exposes pollutants moving time from surface to water table	2
T - Topography: a high slope results in rapid runoff, which indicates less chance to infiltrate contamination into ground.	1
I - Impact of the vadose zone: the vadose zone thickness and matrix are affect contamination intensity and transport timing	5
C - Hydraulic Conductivity: the hydraulic conductivity of the aquifer indicates the quantity of water percolating through the aquifer	3

for hydro-geological investigations (Gogu and Dassargues, 2000, Martínez-Bastida, 2010, Massone, 2010).

The DRASTIC Index was calculated by applying linear combination of all variables with the help of equation 1. Large value for DI indicates high vulnerability of groundwater to deterioration;

$$DI = \Sigma_{j=1}^{7} \ Rj.Wj$$

or

$$DI = DrDw + RrRw + ArAw + SrSw + TrTw + IrIw + CrCw \qquad (1)$$

Where D, R, A, S, T, I, and C are the parameters and r and w are the corresponding rating and weights, respectively.

A GIS database is then establishes to input data from various sources (e.g. remote sensing). The database can be used to store, manipulate and analyse data in various scales and formats ((Rahman, 2008, Sener, et al., 2009). After database creation, layers wise data was register with common coordinates system then thematic maps as well as vulnerability map develop (Voudouris, et al., 2010).

DRASTIC model parameters

Water table data is a significant data source for input in the model to assess groundwater vulnerability. The distance of water from surface to groundwater indicates level of protection and pollutants movement (Hasiniaina F, 2010). The groundwater depth indicates thickness of materials and thus the distance the pollutants need to travel (and disseminate) before it make contact with and become a part of groundwater system (Hentati, 2011). Swallow groundwater due to unconfined aquifer has high chances of being pollutant in comparison to deep aquifer. As the level of confinement reduces, contamination transportation chances will be enhance to the aquifer. Aquifer's water depth can be calculated by the following formula. DTTA (Hasiniaina F, 2010).

$$DTTA (Aquifer's\ water\ depth) = Groundwater\ elevation - Top\ of\ the\ Aquifer\ elevation \qquad (2)$$

The recharge water has the ability to carry contaminants to the water table within the aquifer; hence a large recharge value corresponds to a high potential for groundwater pollution. For net recharge, the pollution potential of an area with confined aquifer is less than that of an unconfined one, because of the

presence of a confining layer. The computation of recharge value in an aquifer is a complicated process which make it harder to ascertain (Khan, 2003). Rainfall is a significant factor which transport leachate and other surface pollutants by infiltration (Voudouris, Kazakis, Polemio and Kareklas, 2010). The values for recharge amount were generated using the estimation formula that Piscopo established in 2001 and that Al-Adamat et al applied in 2003 for their study of the Azraq basin, Jordan;

$$\text{Recharge value} = \text{Slope (\%)} + \text{Rainfall} + \text{Soil permeability} \quad (3)$$

The aquifer media ranking map was developed from an interpolation of the lithology of each borehole. Ratings of each medium represent defined characteristics of each zone. Grain size of soil (texture) can affect the infiltration rate (Voudouris, Kazakis, Polemio and Kareklas, 2010). The sand and gravel constituent of the aquifer media has a rating of 8, which is adjusted base on zone characteristics.

Soil media is considered the first line of defence against groundwater contamination. Soil collects most pollutants types due to intimate contact with human settlement (Bazimenyera et al., 2008). The nature of soil porosity and permeability are two factors, which can control infiltration process (Prasad et al., 2010). Fluid movement, decomposition process, evaporation and other chemical changes are realised on soil media. Soil permeability value and media thickness can also play significance roles in contaminant transportation.

Topography of the underlying aquifer is considered to have the lowest impact factor on vulnerability. Fluid run off capacity will increase with high slop gradient, while low slop equates to more time for infiltration (Naser Ebadati 2012). This permits high infiltration of polluted water, which enhance contaminants migration to aquifer (Bai, et al., 2011) Thus the area has a slow run-off and high percolation.

The vadose zone (VZ), have no water during the dry or summer season, however it is the most unsaturated layer above the water table, forming a significant part in measuring pollution potential (Voudouris et al., 2010). This situation is reversed in the rainy season, where the VZ is saturated. Various chemical reactions, such as biodegradation, filtration and diffusion processes take place in VZ. Saturated zones have great resistance against contamination transportation from surface

to groundwater as compare to unsaturated zones (Gogu and Dassargues, 2000). This is a natural filtration and purification system of groundwater giving it low resistance and high susceptible to decay.

The Hydraulic Conductivity of an aquifer refers to its ability to transmit water. A high conductivity indicate high vulnerability while low conductivity means high resistance against contamination transportation (Rahman, 2008). A major flaw of the DRASTIC model (Voudouris et al., 2010), is its difficulty in calculating an accurate value for Hydraulic Conductivity. The C factor has control over groundwater flow; which have a close relationship with pollutants movement throughout the water table. The hydraulic conductivity can be calculated on the availability of transmissivity and aquifer thickness, based on following formula;

$$T = K*b \quad (4)$$

Where; T= transmissivity, K= hydraulic conductivity and b=aquifer thickness

Aquifer vulnerability assessment

Chung and Fabbri (2001), undertook a study to determine the degree of aquifer vulnerability, using the classification method. They classified the vulnerability indices based on a fixed interval of area percentage (Chung et al., 2001). After calculating vulnerability index they were then arranged in descending order and divided into classification as risk. Suitable colours were selected to represent the pixels. Aller is credit with introducing the colour coding of the vulnerability models (Aller, 1987). Assigned colours are; blue - low, green - moderate and red - high vulnerability. Colours make it easier for the vulnerability models to be interpreted. DRASTIC vulnerability index was calculated using equation 1. Value representation method is considered better to identify aquifer vulnerability of different areas. The higher the degree of DRASTIC index the greater the vulnerability of the aquifer to contamination. Qualitative risk categories can be derived from ordering the DRASTIC indices computed values into; low, moderate, high, and very high.

Sensitivity analysis

Generally, two types of sensitivity analysis tests can be computed; one is removal sensitivity analysis and the other is single parameter sensitivity analysis (Weldon, et al., 1990). By using seven parameters unperturbated vulnerability index can be obtained and perturbated vulnerability index

calculated by using minimum parameters. Removal sensitivity analysis test, computes vulnerability sensitivity by eliminating one or more parameters layers using the following equation;

$$S= (| V/N - V'/n |) \times 100 \qquad (5)$$

Where:

S= the sensitivity measure, V and V' =the unperturbated and perturbated vulnerability indices, respectively.

N and n = the number of data layers used to compute V and V'.

Sensitivity analyses examine the behavior of individual parameters towards aquifer vulnerability and present the result in the form of an analytical model (Ckakraborty, et al., 2007). Application of sensitivity analysis provides credible information on assigned rating, weight and assessing the contribution of each parameter to vulnerability (Al-Adamat, et al., 2003). This is important since other models may create errors and uncertainties of the individual parameters in output (Rosen, 1994). In previous research minimum numbers of parameters were used to develop DRASTIC model by treating some parameters as constant values (McLay et al., 2001).

Single parameter sensitivity analysis was obtained by identifying vulnerability impact of each parameter in DRASTIC model on vulnerability index. It compares the "effective" or "real" weight of each input parameter in each polygon with the "theoretical" weight assigned by the analytical model. The "effective" weight of each polygon was obtained using the following formula;

$$W= (Pr \times Pw / V) \times 100 \qquad (6)$$

Where: W = effective weight of each parameter, Pr and Pw= the rating value and weight of each parameter and V = overall vulnerability index.

Results and discussion

Following the methodological application, thematic map of each parameter and aquifer vulnerability map were developed to evaluate groundwater deterioration vulnerability and risk. In this section, vulnerability results for each parameter are presented and discussed for Lahore City.

Water depth and Recharge

Water level in Lahore aquifer, serving the city, has decreased from 5m to 44m over the past five years. Over-exploitation of groundwater linked increasing urbanisation and many reasons such as domestic use, horticulture demand, local industries etc. An editorial in a local daily newspaper (Dawn) reported that a WASA study in 2010, which was undertaken with assistance from the Pakistan Institute of Nuclear Science and Technology (PINSTECH), an arm of the Pakistan Atomic Energy Commission, revealed that the minimum aquifer level in Lahore (main city area) reached a minimum of 21.55mASL and maximum 43.90mASL (Dawn, 2012). The unconfined nature of the Lahore aquifer contributes to its high vulnerable to pollution.

The west-south belt shows highest water table occurring between 5m to 14m, due to irrigation based recharge. The unequal distribution of groundwater resources means that water is flowing towards the Central Business District (CBD) of the city from other peripheral areas. Water flowing from other areas brings with is pollutants from rivers and from industrial areas adding to further contamination. Final water level map (Figure 3(A)) represents four respective water levels;

Level I: 5m to 14m covering 8% of the area,
Level II: 14m to 24m covering 14% of the area,
Level III: 24m to 34m covering 42% of the area, and,
Level IV: 34m to 44m covering 36% of the area.

The dense urban settlement grid of the Lahore area could possibly explain this low recharge rate in this area. Similarly, less urbanised area mean greater opportunity for surface recharging from rainfall and irrigation. Lahore aquifer depends on rainfall for groundwater recharge, however a number of other factors equally participate in the recharge process such as; River Ravi, irrigation and cultivation system, city water and sanitation system and storm water drains. National Engineering Services Pakistan (NESPAK) has computed recharge value through soil moisture and other research also used various methods. Considering the topography and lithology, the recharge rate has been computer to vary from between 0.18mm/day to 0.5mm/day. Contamination transportation from surface to aquifer depends on recharge rate (Madl-Szonyi and Fule, 1998). The water from shallow aquifer is not potable; therefore domestic water supply

pumping stations go as deep as 600ft to access potable water. Three categories of recharge rates were computed in final map (Figure 3(B)), which covered an area of 9% (DRASTIC Index value 6), 17% (DRASTIC Index value 7) and 74% (DRASTIC Index value 8).

Aquifer Media

Aquifer media and constituents are the path through which water is transported to the aquifer. This can determine the flow rate and levels and types of contamination, as well as aquifer groundwater reserves. These contaminates reach the groundwater through weak soil layers within the aquifer media. The soil layers within the aquifer region recorded a high porosity due to its high sand constituent. The aquifer media has a homogeneous property which is consist of sand and gravel. Historically the area was part of the famous Indus River; therefore sand occurs in high quantities and is a major component in all layers. Uniform rating 8 was assigned for developing aquifer media map. Aquifer media for the complete area is covered with sand and gravel material.

Soil Media

The nature of the surface soil is an important factor in protecting the aquifer from contamination. During recharge this layer absorbs pollutants and influence infiltration into groundwater, thus retarding contamination. In Lahore the material in soil media is composed of silt loam, clay loam and sand, although most areas are clay loam. Rating assigned to clay loam, silt loam and sand are 3, 4 and 9 respectively, DRASTIC weight is 2 for soil media. Clay has less porosity value then sand and silt, reducing aquifer vulnerability. The highest rating is 18, which covers 13% while 6 and 8 rating occupied 68% and 18% of total area respectively. Silty loam and sand is found in the central area and west with small area, while the remaining areas are partly covered by clay loam.

Topography

Lahore's topography is generally flat and slopes towards south and south west at an average gradient of 1:3000. The slope varying from nearly flat to very gentle are assigned DRASTIC index maximum rating 9 and minimum 5, respectively. The topography layer with slopes of 0-5% covers most of the area (Figure 3C). The slope percentage increases from east-north and northwest of Lahore, in areas associated with the river. River banks have lowest slope value and percentage. Topography is assigned a

rating value of 1, reflecting its low to moderate effect on groundwater vulnerability.

Impact of Vadose Zone (VZ)

The layer in the VZ has two types of material; 1) sand, silt and clay with rating 6, and 2) sand and gravel assigned rating 8. DRASTIC model assigned a value of 5 to the VZ as indication of its importance to percolation and thus aquifer contamination (vulnerability). Similarly, a DRASTIC index of 30 and 40 for the VZ impact indicates its high influence on aquifer vulnerability. Areas to the west-south and west-north side's the River Ravi are composed mainly of sand and gravel. However, central and east-south regions of Lahore have secondary category material. Impact of VZ was prepared from the lithological cross-sections obtained from the geophysical data. The VZ media is evaluated with ~51.4% (DRASTIC Index 6) of the study area covered by sand, silt and clay soils. The sand and gravel account approximately 49.6% (DRASTIC Index 8) of the study area (Figure 3D).

Hydraulic Conductivity

The hydraulic conductivity correlated with aquifer capacity to transmit water. High values mean high contamination potential. NESPAK, 1991:Ref (Gabriel and Khan, 2010) calculated average value in the area of 34.04m/day and standard deviation of 5.67m/day with minimum and maximum hydraulic conductivity values of 24.06m/day and 56.23m/day respectively. The Lahore aquifer area is divided into three categories relating to hydraulic conductivity values and assigned rating 4, 6 and 8. Hydraulic Conductivity is affected by water level and layers material. Using DRASTIC Index, calculated values for hydraulic conductivity were 1.7% (4), 19.6% (6) and 78.7% (8) in Lahore (Figure 3E). Hydraulic conductivity index values between 9 and 18 are regarded as moderate. High hydraulic conductivity represents more pollutants potential degree in DRASTIC model technique (Aller, 1987).

Vulnerability of the DRASTIC model

Considering equation 1, final computed values for DRASTIC Index provide numerical range for vulnerability criteria and aquifer vulnerability analysis. For Lahore, the DRASTIC index value degree varied from 95 to 162 divided into four categories; (1) no risk area (95–112), (2) low vulnerability (113–129), (3) moderate vulnerability (130–147), and (4) high vulnerability (148–162). These are further shown in Table 2.
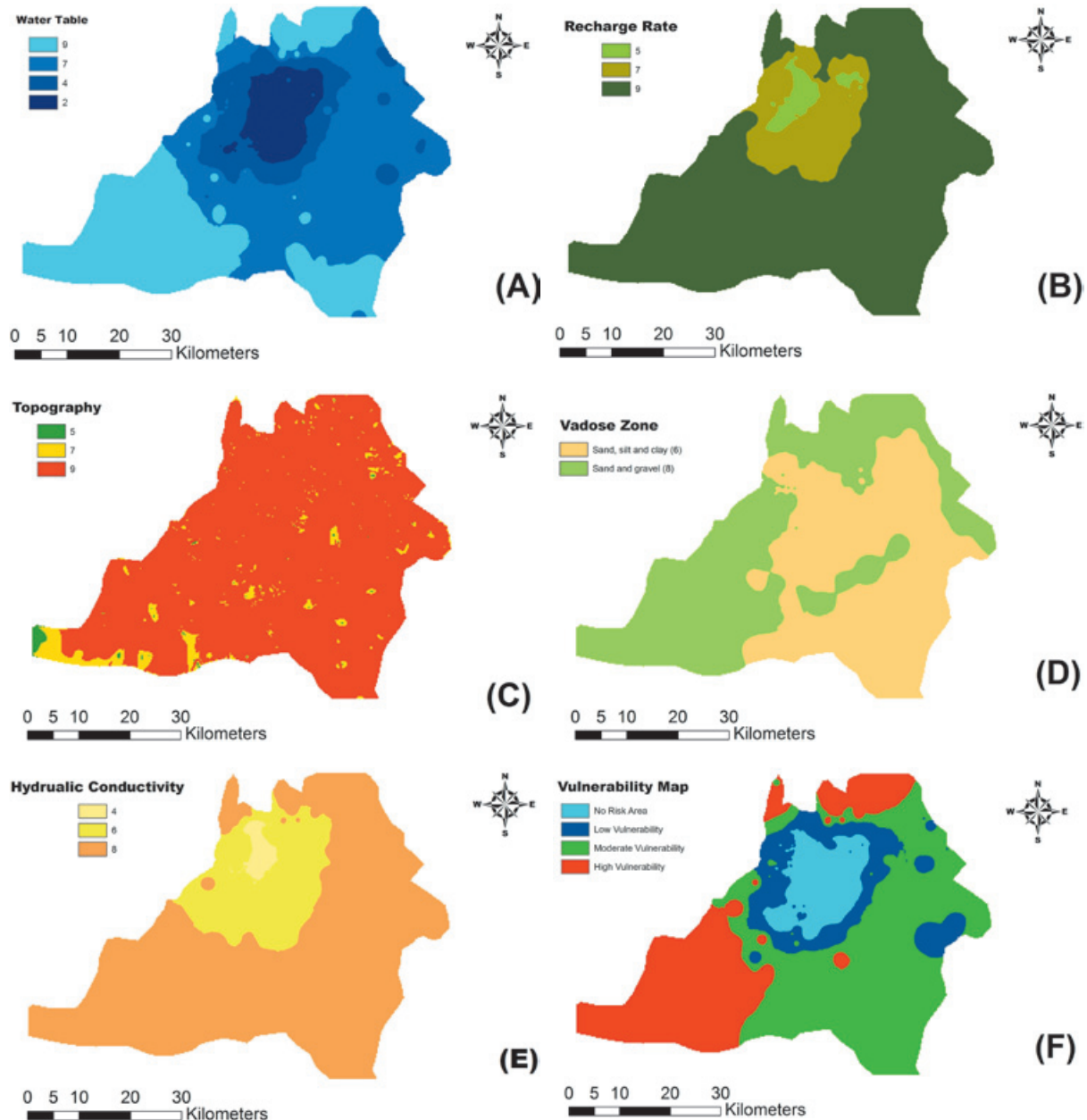
Figure 3. Evaluation layer of the seven parameters and groundwater vulnerability. (A - F) evaluation layer of the water depth, net recharge, topography, impact of vadose zone and hydraulic conductivity. The simulated year is 2000. (F) Groundwater vulnerability evaluation layer of study area.

Table 2. DRASTIC index values in Lahore City with Vulnerability zones and Area Percentage.

DRASTIC index value	Vulnerability zone	Area (%)
95-112	NO Risk Area	10.4
113-129	Low	14.5
130-147	Moderate	46.3
148-162	High	28.8

Based on vulnerability, appropriate colours were applied to each category. In the final DRASTIC vulnerability map four distinct categories are represented; (1) high vulnerability - red (north and south-west of map) associated with high risk of contamination; (2) no risk - light blue (Central areas); (3) low vulnerability – dark blue ribbon, surrounding the light blue and (4) moderate vulnerability - green (north-east and south-east areas), where vulnerability is intrinsic

to the aquifer's characteristics under Lahore city (Figure 3F). Vulnerability map (Figure 3F) shows that vulnerability level is low in the CBD of Lahore, due to low groundwater level and less recharge rate due to urban ground cover.

Urban density decreases with increase distance from the CBD, and thus decreasing groundwater contamination, showing the positive correlation between urbanisation and groundwater contamination. However, less populated areas and areas of irrigation represents higher degree of vulnerability. Evidently, high pollution level within the study area relates to the extent of settlement and agricultural activities. Figure 6(F) shows that total high risk area covers 28.8% of total study area. Moderate, low and no risk aquifer vulnerability areas covers 46.3%, 14.5% and 10.4% area respectively. Areas composed of high quantity of sand and silt as mentioned earlier contains high risk of contamination transportation. Sand dunes area indicates high recharge potential, shallow water level and more permeable soils, represents high and moderate aquifer vulnerability.

Sensitivity of the DRASTIC model

The statistical summaries, of the seven hydro-geological parameters calculated using the DRASTIC index, are shown in Table 3. Two parameters (topography and aquifer media) show high vulnerability degree with mean value more than 8. However recharge rate shows the lowest mean value of 2.08. Recharge rate and soil media reveal low risk aquifer contamination with mean values 2.08 and 4.27 respectively; while water depth, VZ impact and hydraulic conductivity show moderate vulnerability level with mean values 4.54, 6.99 and 6.20 respectively.

Table 3 shows water depth with highest variable value of 54.61% and aquifer media has lowest variable value zero of percentage coefficient of variance (CV). Soil media 37.06%, recharge rate 36.72% and hydraulic conductivity

22.85%, represent moderate variable, while topography 10.18% and hydraulic conductivity 14.33%, are low variable parameters.

Summary of rank order correlation analysis amongst the seven DRASTIC parameters is shown in table 4. High relationship can be seen between net recharge and hydraulic conductivity (Value of r=0.89), depth to water and hydraulic conductivity (value of r=0.73), depth to water and Recharge rate (value of r=0.71), while a weak relationship exists between hydraulic conductivity and VZ impact (value of r=0.17). The value indicating relationship between recharge and hydraulic conductivity shows that recharge rate at urban and rural area differs and greatly affects aquifer's Transmissivity. Similarly, water depth shows strong correlation with recharge and hydraulic conductivity. Table 4, identify over exploitation of groundwater, less recharge and decreasing water level at Lahore city. Only water depth and VZ impact (value of r=0.3) exposed moderate correlation, due to unsaturated material at VZ. Evidences of relatively few significant correlations at 95% confidence level (Table 4), shows that the DRASTIC parameters in Lahore Heights were generally considered independent.

Single-parameter sensitivity analysis

In single parameter sensitivity analysis section theoretical weight and effective weight of the seven parameters are compared and verify individual parameter effect on vulnerability index. Theoretical weight represents DRASTIC index weight of each parameter and effective weight assigned values by the analytical model. The "effective" weight is a function of the value of the single parameter with regard to the other six parameters as well as the weight assigned to it by the DRASTIC model (Rahman, 2008).

The DRASTIC model effective weight of seven parameters presented deviation of each parameter's theoretical weight in table 5. The research shows that the VZ impact and aquifer media possess high degree of effective weight

Table 3. A Statistical Summary of the DRASTIC Parameters map.

Parameter	Mean	Minimum	Maximum	Std. Dev.	CV (%)
D	4.54	2	9	2.48	54.61
R	2.08	1	3	0.76	36.72
A	8.00	8	8	0.00	0.00
S	4.27	3	9	1.58	37.06
T	8.70	5	9	0.89	10.18
I	6.99	6	8	1.00	14.33
C	6.20	4	8	1.42	22.85

Table 4. Summary of rank-order correlation analysis result between seven DRASTIC parameters.

Correlated parameters	Correlation coefficient, r	Significance level, p
Water depth and Vadose Zone Impact	0.3	p<0.0001
Net recharge and Hydraulic conductivity	0.89	p<0.0001
Depth to water and Hydraulic conductivity	0.73	p<0.0001
Hydraulic conductivity and Vadose Zone Impact	0.17	p<0.0001
Water depth and Recharge rate	0.71	p<0.0001

Only statistically significant (confidence level at/or more than 95%) inter-correlations are tabulated.

in assessing vulnerability, with mean value of 28.17% and 19.56% respectively. Both effective weights contain higher value than theoretical weight used in developing DRASTIC model. Topography reveals an effective weight of 7.13%, compared to a low value of 4.30% for theoretical weight. However, water table, recharge rate and soil media all possess high theoretical weight with regard to effective weight. Effective weight of 14.72% for hydraulic conductivity is slightly high compared with a theoretical weight of 13%. The VZ impact and aquifer media shows the significance of obtaining accurate, detailed, and representative information about these layers.

Conclusions and recommendation

Lahore is now one of Pakistan's most rapidly urbanising cities, where like most cities in the developing world, urban management and development planning are far behind the pace of urbanisation. Most times the impacts of urbanisation are so visible on the surface that most studies simply ignore as impacts on underground resources, such as groundwater. Current research is conducted to assess aquifer vulnerability level at Lahore city by developing DRASTIC model in GIS environment. Seven hydro-geologic parameters were used to develop the final vulnerability map.

The DRASTIC Vulnerability Index was computed between 95 and 162. Based on hydro-geological field investigations and using a quintile classification method. These values were further reclassified into three classes namely high (148–162), medium (130–147), low (113–129) and no risk (95-112) vulnerable aquifer areas which cover 28.8%,46.3%, 14.5% and 10.4% of the aquifer, respectively.

Densely urbanized areas were identified having the lowest vulnerability, and less permissible to contamination transportation, while cultivation and high water level area were identified as easily polluted. It was also noticed that north-east and east-south sides has moderated vulnerability potential and west-south part contains high vulnerability degree. Central regions were more susceptible to contamination due the variation in groundwater level. Accordingly, the importance of protecting high vulnerability area and contamination sources is crucial. Topography and aquifer media are the two hydro-geological parameters calculated using the DRASTIC which show high vulnerability degree with mean value more than 8. In terms of aquifer vulnerability, vadose zone and aquifer media represent it more precisely as these both criteria provide highest weight in vulnerability assessment compared to recharge rate, water depth, VZ impact and

Table 5. Statistics of the single parameter sensitivity analysis.

Parameter	Theoretical weight	Theoretical weight (%)	Effective weight (%)	SD*
D	5	21.7	17.08	6.85
R	4	17.4	6.46	1.77
A	3	13	19.56	3.08
S	2	8.7	6.87	2.49
T	1	4.3	7.13	1.47
I	5	21.7	28.17	4.32
C	3	13	14.72	2.04

*SD Refer to Standard Deviation

hydraulic conductivity, which represent low to moderate values for vulnerability.

Due to high abstraction rate of groundwater, the water table has declined by approximately 0.84m yearly. As per the DRASTIC method, declining water table reduces the aquifer vulnerability; however, it enhances saltwater intrusion. Groundwater quality monitoring system must be established for regular groundwater observation and can use as prevention tool to avoid aquifer pollution.

The developed groundwater vulnerability maps can be used for groundwater assessment, water resources risk and human activities planning for future. It is also useful for water authorities and land development planner for land and groundwater resources management according to local demand. Aquifer vulnerability assessment is very important for environment, economy and social development.

The current research provides the catalyst for further investigation into the subject of groundwater quality in Lahore and cities with similar geo-hydrological conditions. These studies can be designed along similar lines as the extant research, with considerations for modifications to the DRASTIC model. The results obtained from this research, may be improved by incorporating other social, and ecological factors, as well as the use of mathematical modeling and GMS software to enhance the efficiency of the model.

Acknowledgments

References

Ahmed K., 2010, Impacts of Solid Waste Leachate on Groundwater and Surface Water Quality, *Journal of the Chemical Society of Pakistan*, 32, 606.

Ahn J.J., Kim Y.M., Yoo K., Park J., Oh K.J., 2011, Using GA-Ridge regression to select hydro-geological parameters influencing groundwater pollution vulnerability, *Environmental monitoring and assessment*, 1-9.

Al-Adamat R.A.N., Foster I.D.L., Baban S.M.J., 2003, Groundwater vulnerability and risk mapping for the Basaltic aquifer of the Azraq basin of Jordan using GIS, Remote sensing and DRASTIC, *Applied Geography*, 23, 303-324.

Al-Zabet T., 2002, Evaluation of aquifer vulnerability to contamination potential using the DRASTIC method, *Environmental Geology*, 43, 203-208.

Albinet M., Margat J., 1970, Cartographie de la vulnérabilité à la pollution des nappes d'eau souterraine, *Bull. BRGM, 2ème série,* 3,4, 13-22.

Aller L., Bennet T., Leher J.H., Petty R.J., Hackett G., 1987, DRASTIC: A standardized system for evaluating ground water pollution potential using hydrogeologic settings, pp 622.

Baalousha H., 2006, Vulnerability assessment for the Gaza Strip, Palestine using DRASTIC, *Environmental Geology*, 50, 405-414.

Baalousha H., 2010, Assessment of a groundwater quality monitoring network using vulnerability mapping and geostatistics: A case study from Heretaunga Plains, New Zealand, *Agricultural Water Management*, 97, 240-246.

Babiker I.S., Mohamed M.A.A., Hiyama T., Kato K., 2005, A GIS-based DRASTIC model for assessing aquifer vulnerability in Kakamigahara Heights, Gifu Prefecture, central Japan, *Science of the Total Environment,* 345, 127-140.

Bai L., Wang Y., Meng F., 2012, Application of DRASTIC and extension theory in the groundwater vulnerability evaluation, *Water and Environment Journal,* 26,3,381-391.

Batool S.A., Ch M.N., 2009, Municipal solid waste management in Lahore city district, Pakistan, *Waste management*, 29, 1971-1981.

Bazimenyera J.D.D., Zhonghua T., 2008, A GIS Based DRASTIC Model for Assessing Groundwater Vulnerability in Shallow Aquifer in Hangzhou-Jiaxing-Huzhou Plain, China, *Research Journal of Applied Sciences*, 3, 550-559.

Bishop P., Misstear B., White M., Harding N., 1998, Impacts of sewers on groundwater quality, *Water and Environment Journal*, 12, 216-223.

Chung C., Fabbri A., 2001, Prediction models for landslide hazard zonation using a fuzzy set approach. Geomorphology and Environmental Impact Assessment Balkema, Lisse, The Netherlands, 31-47.

Ckakraborty S., Paul P., Sikdar P., 2007, Assessing aquifer vulnerability to arsenic pollution using DRASTIC and GIS of North Bengal Plain: A case study of English Bazar Block, Malda District, West Bengal, India, *Journal of Spatial Hydrology,* 7,1.

Ebadati N., Motlagh K. S., Behzad N., 2012, Application of DRASTIC Model in Sensibility of Groundwater Contamination (Iranshahr–Iran) Paper presented at the 2012 International Conference on Environmental Science and Technology, Singapore 2012.

Evans B.M., Myers W.L., 1990, A GIS-based approach to evaluating regional groundwater pollution potential with DRASTIC, *Journal of Soil and Water Conservation,* 45, 242-245.

Foster S., 1987, Fundamental concepts in aquifer vulnerability, pollution risk and protection strategy Vulnerability of Soil and Groundwater to Pollutants, TNO Committee on Hydrogeological Research, Proceedings and Information, pp. 69-86.

Gabriel H., Khan S., 2010, Climate Responsive Urban Groundwater Management Options in a Stressed Aquifer System. IAHS-AISH publication: 166-168.

Ghanbari F., Amin S.F., Monavari M., Zaredar N., 2011, A new method for environmental site assessment of urban solid waste landfills, *Environmental monitoring and assessment*, 184, 1221-1230.

Gogu R., Dassargues A., 2000, Current trends and future challenges in groundwater vulnerability assessment using overlay and index methods, *Environmental Geology,* 39, 549-559.

Greenman D.W., Swarzenski W.V., Bennett G.D., 1967, Ground-water hydrology of the Punjab, West Pakistan, with emphasis on problems caused by canal irrigationsU S geol Surv Wat-Supply pap 1608-H U S Govt Printing Office, Washington,D.C, pp. 70.

Hasiniaina F.Z.J., Guoyi L., 2010, Regional assessment of groundwater vulnerability in Tamtsag basin. Mongolia using drastic model. *Journal of American Science*, Marsland Press, 6, 65-78.

Hentati I.M., Ben D.H., 2011, A statistical and geographical information system analysis for groundwater intrinsic vulnerability: a validated case study from Sfaxâ€"Agareb, Tunisia, *Water and Environment Journal*, 25, 400-411.

Jamrah A., Al-Futaisi A., Rajmohan N., Al-Yaroubi S., 2008, Assessment of groundwater vulnerability in the coastal region of Oman using DRASTIC index method in GIS environment, *Environmental monitoring and assessment,* 147, 125-138.

Khan A., Miura H., Prusinski J., Ilyas S., 1990, Matriconditioning of seeds to improve emergenceProceedings of The Symposium on Stand Establishment of Horticultural Crops, pp. 13-28.

Khan S., 2003, Investigating conjunctive water management options using a dynamic surface-groundwater modelling approach: a case study of Rechna Doab CSIRO Land and Water.

Lapworth D.J., Gooddy D., Stuart M., Chilton P., Cachandt G., Knapp M., Bishop S., 2006, Pesticides in groundwater: some observations on temporal and spatial trends, *Water and Environment Journal,* 20, 55-64.

Madl-Szonyi J., Fule L., 1998, Groundwater vulnerability assessment of the SW Trans-Danubian central range, Hungary, *Environmental Geology*, 35, 9-18.

Martinez-Bastida J.J., Arauzo M., Valladolid M., 2010, Intrinsic and specific vulnerability of groundwater in central Spain: the risk of nitrate pollution, *Hydrogeology Journal,* 18, 681-698.

Massone H.Q., Lo M., Martanez D., 2010, Enhanced groundwater vulnerability assessment in geological homogeneous areas: a case study from the Argentine Pampas, *Hydrogeology Journal*, 18, 371-379.

McLay C., Dragten R., Sparling G., Selvarajah N., 2001, Predicting groundwater nitrate concentrations in a region of mixed agricultural land use: a comparison of three approaches, *Environmental Pollution*, 115, 191-204.

Merchant J.W., 1994, GIS-based groundwater pollution hazard assessment: a critical review of the DRASTIC model, *Photogrammetric engineering and remote sensing*, 60, 1117-1128.

Padagett D., 1994, Using DRASTIC to improve the integrity of geographical information system data used for solid waste management facility sitting, a case study, *Environ Prof*, 16, 211-219.

Pakistan's Punjab Province Faces 50 Percent Water Shortfall, 2012, http://www.ooskanews.com/international-water-weekly/pakistan%E2%80%99s-punjab-province-faces-50-percent-water-shortfall_21820.

Panagopoulos G., Antonakos A., Lambrakis N., 2006, Optimization of the DRASTIC method for groundwater vulnerability assessment via the use of simple statistical methods and GIS, *Hydrogeology Journal*,14, 894-911.

Prasad R.K., Singh V., Krishnamacharyulu S.K.G., Banerjee P., 2010, Application of drastic model and GIS: for assessing vulnerability in hard rock granitic aquifer, *Environmental monitoring and assessment*, 176, 143-155.

Qian H., Li P., Howard K.W.F., Yang C., Zhang X., 2011, Assessment of groundwater vulnerability in the Yinchuan Plain, Northwest China using OREADIC, *Environmental monitoring and assessment*, 184, 3613-3628.

Rahman A., 2008, A GIS based DRASTIC model for assessing groundwater vulnerability in shallow aquifer in Aligarh, India, *Applied Geography*, 28, 32-53.

Rosen L., 1994, A study of the DRASTIC methodology with emphasis on Swedish conditions. *Ground Water*, 32, 278-285.

Samake M., Tang Z., Hlaing W., Innocent N., Kasereka K., Balogun W.O., 2011, Groundwater Vulnerability Assessment in Shallow Aquifer in Linfen Basin, Shanxi Province, China Using DRASTIC Model, *Journal of Sustainable Development,* 4, 53.

Sami F., 2001, 'Water quality monitoring of Hudiara drain', an independent consultancy for data analysis and water quality management plan. In: Department PEP (ed), Lahore. Schnoor J.L., 1996, Environmental modeling: fate and transport of pollutants in water, air, and soil, *John Wiley and Sons.*

Secunda S., Collin M., Melloul A., 1998, Groundwater vulnerability assessment using a composite model combining DRASTIC with extensive agricultural land use in Israel's Sharon region*, Journal of Environmental Management*, 54, 39-57.

Sener E., Sener S., Davraz A., 2009, Assessment of aquifer vulnerability based on GIS and DRASTIC methods: a case study of the Senirkent-Uluborlu Basin (Isparta, Turkey), *Hydrogeology Journal,* 17, 2023-2035.

Shamsuddin S., 2000, A study of groundwater pollution vulnerability using DRASTIC/GIS, West Bengal INDIA*, Journal of Enviromental hydgeology,* 8, 1-8.

Shimura S., Yokota I., Nitta Y., 2001, Research for MSW flow analysis in developing nations, *Journal of Material Cycles and Waste Management,* 3, 48-59.

Solley W., 1988, Estimated Use of Water in the United States in 1985. *US Geological Survey Circular 1004*, 82.

Thirumalaivasan D., Karmegam M., Venugopal K., 2003, AHP-DRASTIC: software for specific aquifer vulnerability assessment using DRASTIC model and GIS, *Environmental Modelling & Software*, 18, 645-656.

United State Environmental Protection Agency E., 1985, DRASTIC: a standard system for evaluating groundwater potential using hydrogeological settings, Ada, Oklahoma.

Vias J., Andreo B., Perles M., Carrasco F., 2005, A comparative study of four schemes for groundwater vulnerability mapping in a diffuse flow carbonate aquifer under Mediterranean climatic conditions, Environmental Geology, 47, 586-595.

Voudouris K., Kazakis N., Polemio M., Kareklas K., 2010, Assessment of intrinsic vulnerability using DRASTIC model and GIS in Kiti aquifer, Cyprus. *European Water.*

Wang Y.M., Li B.J., Ye Y., Fu H., Ihm, D.S., 2007, Vulnerability of groundwater in Quaternary aquifers to organic contaminants: a case study in Wuhan City, China, *Environmental Geology,* 53, 479-484.

Weldon A.L., Monson W., Svoboda L., 1990, Attribute error and sensitivity analysis of map operations in geographical informations systems: suitability analysis, *International Journal of Geographical Information System*, 4, 413-428.

Seismicity in the Basin and Range Province of Sonora, México, between 2003 and 2011, near the Rupture of the 3 May 1887 Mw 7.5 Earthquake

Raúl R. Castro

Resumen

Se estudió sismicidad regional en la Provincia de Cuencas y Cordilleras de Sonora, México, cerca de la región epicentral del sismo del 3 de mayo de 1887 Mw 7.5. Se usaron tiempos de arribo de ondas de cuerpo registradas por la red local RESNES (Red Sísmica del Noreste de Sonora) y dos estaciones de banda ancha regional de la red RESBAN (Red Sismológica de Banda Ancha del Golfo de California) para localizar las fuentes sísmicas originadas entre 2008 y 2011. Primero, se determinaron coordenadas hipocentrales preliminares con el programa Hypoinverse (Klein, 2002) y entonces las coordenadas iniciales fueron determinadas con el método de corrección por estación de fuente específica (Lin and Shearer, 2005). Este procedimiento fue usado en un estudio previo (Castro *et al*., 2010) para localizar sismos originados en la misma región entre 2003 y 2011. La mayoría de los eventos relocalizados se agrupan cerca de las fallas que rompieron durante el sismo de 1887. Adicionalmente, se documenta la sismicidad a lo largo de las fallas normales de la Provincia de Cuencas y Cordilleras al sur de la ruptura de 1887, tales como las fallas Villa Hidalgo y Granados, y las fallas que confinan la cuenca de Bacadéhuachi. La región del centro poblacional más grande, Hermosillo, parece estar sísmicamente quieta. Esta observación es apoyada por la ausencia de sísmos en el catálogo del Centro Sismológico Internacional (ISC) o sismicidad histórica documentada en esta área.

Palabras clave: sismicidad en Sonora, sismo de Sonora de 1887, provincia de Cuencas y Coordilleras.

Abstract

The regional seismicity in the Basin and Range Province of Sonora, México, near the epicentral region of the 3 May 1887 Mw 7.5 earthquake was studied. Body wave arrival times recorded by the local network RESNES (Red Sísmica del Noreste de Sonora) and two regional broadband stations of the RESBAN (Red Sismológica de Banda Ancha del Golfo de California) network were used to locate the seismic sources originating between 2008 and 2011. Preliminary hypocenter coordinates were first determined with the program Hypoinverse (Klein, 2002) and then relocated the initial coordinates with the source-specific station term method (Lin and Shearer, 2005). The same procedure was used in a previous study (Castro *et al*., 2010) to locate the earthquakes originating in the same region between 2003 and 2007. I also present in this paper a depurated catalog of events recorded from 2003 to 2011. Most relocated events cluster near the faults that ruptured during the 1887 earthquake. Additionally, I document seismicity along Basin and Range Province normal faults south of the 1887 rupture, such as the Villa Hidalgo and Granados faults and the faults bounding the Bacadéhuachi basin. The region of the largest population center, Hermosillo, appears to be seismically quiescent. This observation is supported by a lack of entries in the catalog of the International Seismological Centre (ISC) or documented historical seismicity in that area.

Key words: seismicity in Sonora, 1887 Sonora earthquake, Basin and Range province.

R. R. Castro
Centro de Investigación Científica
y de Educación Superior de Ensenada (CICESE),
División Ciencias de la Tierra
Departamento de Sismología
Carretera Ensenada-Tijuana, 3918
22860 Ensenada
Baja California, México.
Corresponding author: raul@cicese.mx

Introduction

The tectonic-physiographic province of the southern Basin and Range is characterized by active extension (Yeats, 2012). The 3 May 1887 Mw 7.5 Sonora, Mexico earthquake is the largest historical event in this region (de Polo *et al*., 1991; Yeats *et al*., 1997), in which an array of three north-south striking, west-dipping normal faults (Pitáycachi, Teras and Otates, Figure 1) slipped sequentially along the western edge of the Sierra Madre Occidental plateau. The documented surface rupture has a length of 101.8 km and a maximum structural displacement of 5.2 m (Suter and Contreras, 2002; Suter, 2008a, 2008b).

The major purpose of this study is to constrain areas of active faulting in northeastern Sonora, specifically in the epicentral region of the 1887 earthquake. In 2002, the Centro de Investigación Científica y de Educación Superior de Ensenada (CICESE), in collaboration with the Instituto de Geología, Universidad Nacional Autónoma de México (UNAM), installed for that reason Red Sísmica del Noreste de Sonora (RESNES), a seismic network surrounding the surface rupture of the 1887 earthquake. The data recorded by RESNES from 2003 to 2007 were presented by Castro *et al*. (2010). Here, we add the recordings from 2008 until 2011, when the monitoring was discontinued and the network was dismantled. Additionally, we present in this paper a depurated catalog of the events recorded by RESNES during the entire existence of the network between 2003 and 2011.

Previous studies

The 1887 Sonora earthquake has generated a long-lasting, still ongoing, and well documented aftershock sequence, as summarized in Castro *et al*., (2010). Based on felt reports and observations with an improvised seismoscope, Goodfellow (1888) and Aguilera (1888) located aftershocks in the stepover between the Pitáycachi and Teras, and Vazquez (1887) in the region of the Otates rupture segments (Figure 1). The seismicity catalogs by Orozco y Berra (1887, 1888) contain compilations of shocks of the 1887 seismic sequence. A summary of the contemporary studies of the 1887 Sonora earthquake was made by Suter (2006). The 1907 MI 5.2 Colonia Morelos earthquake and the 1913 MI 5.0 and 1923 MI 5.7 earthquakes in the Granados-Huásabas region (Suter, 2001) have also been considered aftershocks of the 1887 event, since the distribution of these aftershocks correlates well with calculated changes in Coulomb failure stress resulting from the 1887 rupture (Suter and Contreras, 2002).

Natali and Sbar (1982) studied the microseismicity in the region of the Pitáycachi fault. They deployed a temporal network of 7–10 portable seismographs that operated between 1978 and 1979. They located small earthquakes, with magnitudes M< 2, to the west of the Pitáycachi fault trace and farther south, beyond the network, near the Teras and Otates rupture segments.

Wallace *et al*. (1988) and Wallace and Pearthree (1989) relocated a series of earthquakes that occurred in this region in 1987–1989, the largest one having a magnitude of 4.2. These events together with the 1908 MI 4.8 Fronteras earthquake (Suter, 2001) form a cluster that is likely to have originated on the Teras fault (Suter, 2008b).

Instrumentation and data acquisition

All stations of the RESNES network (Table 1; triangles in Figure 1) are autonomous and consist of Kinemetrics digital recorders (model K2) with an internal triaxial force-balance accelerometer registering three components of ground acceleration and have a built-in Global Positioning System (GPS) timing system. A vertical-component short-period sensor (model L4C) is connected to a fourth recording channel. These stations record local and regional events with a rate of 200 samples per second. Figure 2 shows velocity records from a sample of six earthquakes recorded by three stations (ELO, OAX, and BAC) at different epicentral distances. These well-recorded seismograms show clear P- and S-wave arrivals and a high signal-to-noise ratio for both, local and regional distances.

For events between 2008 and 2011, I started with an initial data set consisting of 504 events (M < 3.6) recorded by at least three stations of the RESNES array and permitting a minimum of five P- and S-wave arrival time readings. For some of these events, particularly those having originated south of the RESNES array, I also used arrival times from stations NE80 and NE81 (Table 1 and Figure 1; located near Caborca and El Novillo dam, respectively) of the RESBAN (Red Sismológica de Banda Ancha del Golfo de California) network. Castro *et al*. (2010) had located events recorded 2003–2007 by RESNES and by stations of the NARS (Network of Autonomously Recording Seismographs) -Baja array. For events having originated between April and December 2007, they had additionally used arrival times from USArray stations located within 150 km of the United States – Mexico border.

Table 1. Station coordinates.

NETWORK	CODE	LATN (deg)	LONG (deg)	ALTITUDE (m)
RESNES	MOC	29.73233	-109.66533	621.0
	MOR	30.85117	-109.16267	998.0
	BAC	29.81117	-109.16300	778.0
	VIH	30.12717	-109.32317	610.0
	SMG	30.55317	-108.96983	945.0
	OAX	30.73650	-109.06050	902.0
	NAC	30.34567	-109.64333	1261.0
	ELO	31.22750	-109.37083	1210.0
	OJO	31.31500	-109.01555	1454.0
	DIV	29.66183	-109.44333	745.0
	CUM	30.10450	-109.66700	1243.0
	HUA	30.23433	-108.95867	1181.0
	ARI	30.08217	-109.05500	1546.0
RESBAN	NE80	30.50000	-112.31983	225.0
	NE81	28.91833	-109.63633	295.0

Figure 1. Distribution of stations (triangles) of the RESNES network and preliminary epicenter locations originating 2003–2011. Stations NE80 and NE81 (black squares) belongs to the RESBAN seismic network. The stars represent centers of population. P (Pitáycachi), T (Teras), and O (Otates) are the faults that ruptured in the 1887 earthquake. Also shown is the Imuris lineament (based on Nourse *et al.*, 1994). The boundaries of the three rectangles delimit areas where mines are located. We eliminated mine blasts inside these rectangles that occurred within the schedule provided by the mine company.
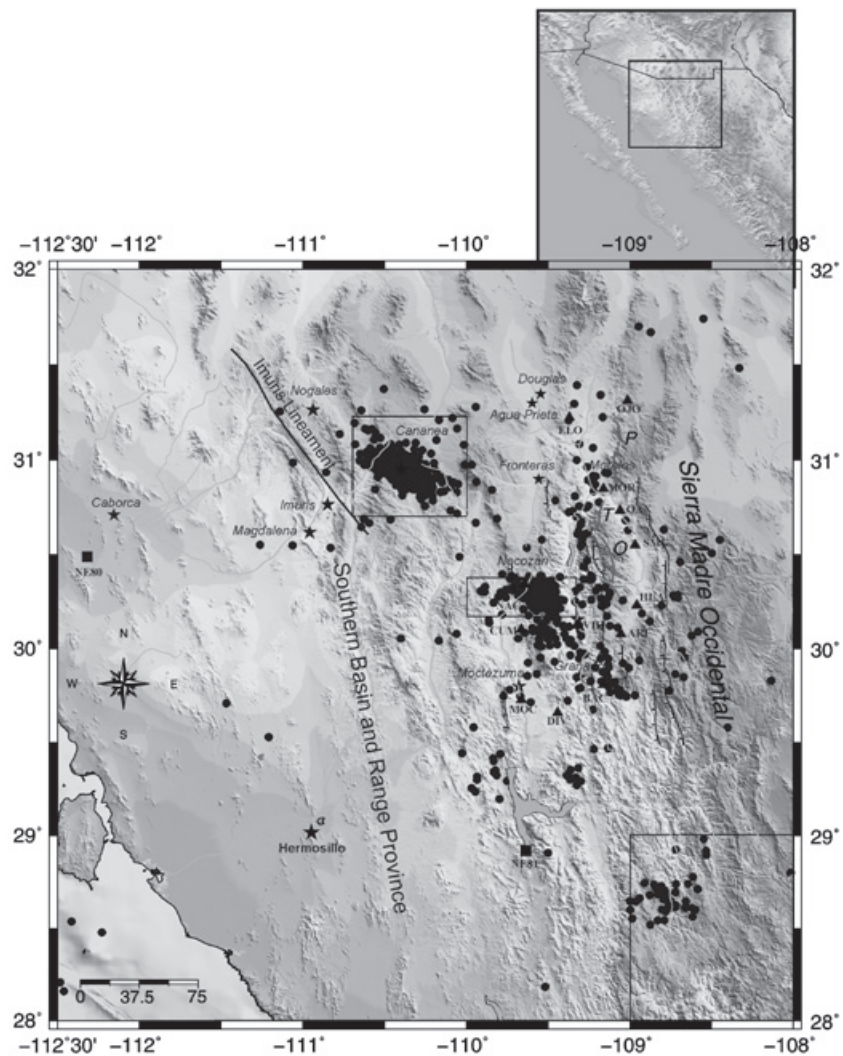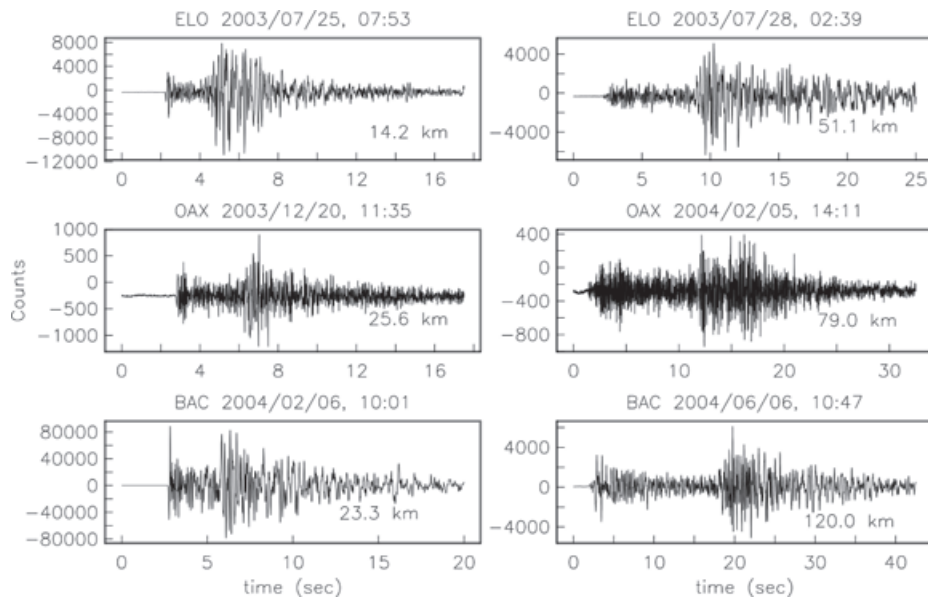
Figure 2. A sample of vertical component seismograms recorded at stations ELO (top), OAX (middle) and BAC (bottom) from different earthquakes. The hypocentral distances are indicated inside the frames (lower right corner).

Methodology

The initial epicentral coordinates and the source depth of the 504 events that had originated between 2008 and 2011 were calculated using the Hypoinverse computer code (Klein, 2002) and the P-wave seismic velocity model V1 (Figure 3 and Table 2) obtained by Harder and Keller (2000) from a wide-angle seismic north-south profile in southwestern New Mexico, close to the epicentral region of the 1887 Sonora earthquake. A very similar model was more recently obtained by Averill and Miller (2013) from an east-west seismic refraction/reflection survey along the New Mexico-Chihuahua border. Only events recorded by at least three stations with more than four clear body wave arrivals and (S-P) ≤ 25 sec were located. P and S wave arrival times were handpicked, with an approximate accuracy of one tenth of

Table 2. P-wave velocity models V1 and V2 (with a gradient) used to calculate the initial hypocentral locations.

Depth intervals (km)	vP (km/s)
0.0 − 1.0	5.10
1.0 − 22.0	5.88
22.0 − 35.0	6.90
Below 35.0	7.95

a second. Then the initial hypocentral locations were added to the nearly 600 local and regional events obtained by Castro *et al*. (2010) for the period 2003–2007. Figure 1 displays the 1107 epicenters located with Hypoinverse for the period 2003-2011. The smallest magnitude of the earthquakes located is 0.9; although not all the events with M>0.9 were located due to the restrictions described above. Subsequently, I dequarried this 2003–2011 initial catalog by removing daylight events (from 18:00 hrs UT to 06:00 hrs UT) and events with a focal depth shallower than 2 km, resulting a new catalog consisting of 300 earthquakes. To dequarry the initial catalog, event swarms near mines were identified based on the seismicity map reported by Castro *et al*. (2010). The boxes in Figure 1 delimit the extent of the swarms in the neighborhood of three main mines: Cananea in the northwest, Nacozari in the central part of the network and Mulatos in the southeast. Events inside those boxes that occurred from 18:00 hrs UT to 06:00 hrs UT were discarded.

The 300 remaining hypocenters were relocated using the source-specific station term (SSST) technique (Richards-Dinger and Shearer, 2000). This method consists of selecting events within a sphere of a specified radius (rmax), with the target event being located at the center. With this technique, each station has a station correction function that varies with source position. This location method is useful for northeastern Sonora,
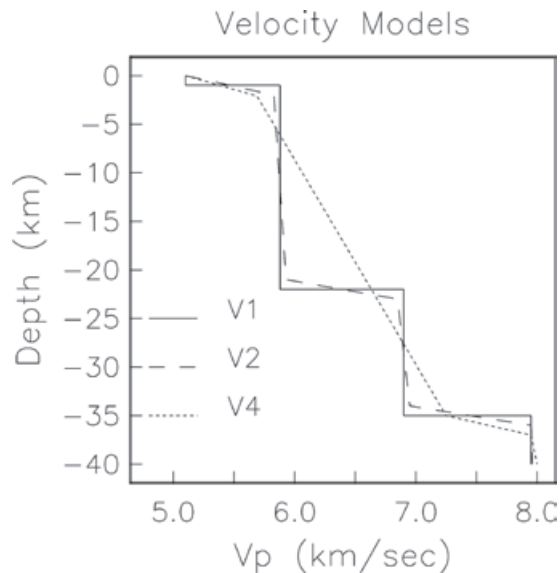
Velocity Models

Figure 3. P-wave velocity models (Tables 2 and 3). We used model V1 (solid line), obtained by Harder and Keller (2000) for southwestern New Mexico, to calculate the original hypocentral locations and models V2 (dashed line) and V4 (dotted line) to relocate the hypocenters.

where the seismic events cover a large area and where lateral velocity heterogeneities can be expected (Castro *et al.*, 2010).

The SSST method was implemented by Lin and Shearer (2005) in their COMPLOC earthquake location code. I relocated the initial dequarried hypocenters, obtained with Hypoinverse, with a modified version of COMPLOC that permits to include regional phases (Pn, Pg, Sn, Sg) and weights the phase arrival picks according to the source-station distance. For this relocation I used the same procedure and velocity models (V2 and V4 in Figure 3) as Castro *et al.* (2010). These velocity models give smaller travel-time residuals than other velocity models tested by Castro *et al.* (2010). Models V2 (Table 2) and V4 (Table 3) consist of three and four layers, respectively, with small gradients to make the change of velocity with depth gradual. The P-wave velocity of the shallowest layer is 5.1 km/s, like in the V1 model by Harder and Keller (2000), and 7.95 km/s at the base of the crust (Tables 2 and 3). We divided the region into five rectangles, shown on Figure 4, to minimize regional variations of the velocity structure. One of the rectangles, northwest of the RESNES array, covers the area near Cananea; three rectangles cover the fault segments that ruptured in 1887; and the last rectangle, located in the southeast, covers the plateau of the Sierra Madre Occidental.

Table 3. P-wave velocity model V4 used to relocate the events.

Depth intervals (km)	vP (km/s)
0.0 − 2.1	5.10
2.1 − 35.0	5.69
35.0 − 37.0	7.25
35.0 40.0	7.95
Below − 40.0	8.00

The catalog of relocated events was filtered again using the same spatial criteria as before, relocated events near the mines (inside boxes in Figure 1) that occurred from 18:00 hrs UT to 06:00 hrs UT were discarded and only the best relocated events (rms< 1 sec) were kept for further analysis.

Results

Figure 4 shows the best relocated epicenters (with rms< 1 sec) obtained using model V2 and having originated between 2003 and 2011, the fault segments that ruptured during 1887, and the locations of the stations of the RESNES array. To assure that other random quarries were not included, relocated events with focal depths shallower than 2 km were also eliminated. Two groups of earthquakes can be identified: a first group on the western margin of the Sierra Madre Occidental, along the fault segments that ruptured in 1887; and a second group near the southern end of the RESNES array, east of Bacadéhuachi (BAC). Castro *et al.* (2010) had located an additional group of events in the Sierra Madre Occidental, near the Mulatos, Sonora gold mine (southeasternmost rectangle on Fig. 1), and near Cananea and Nacozari mines. However, the origin times of these events are within the time window and or focal depths used to eliminate quarry blasts from the data set. Most of the events in the Mulatos, Nacozari and Cananea regions are likely to be mining-related; consequently, they were not include in this study.

Figure 5 shows the focal depth distributions of the original locations obtained with Hypoinverse (top row) and of the events relocated with velocity models V2 (bottom row) and V4 (middle row). The hypocenters are projected onto an east-west section (left column) and onto a north-south section (central column). The relocated events show significantly less scatter than the original locations. The seismicity shows well-defined subvertical alignments reaching a depth of 40 km, which are interpreted below. Comparing
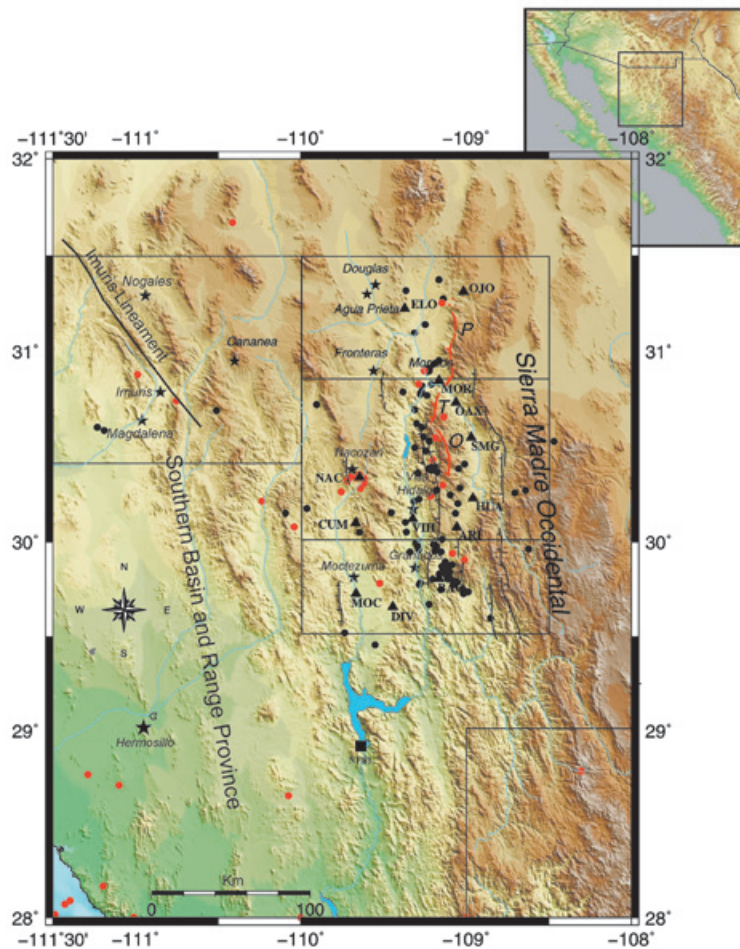
Figure 4. Relocated epicenters originating 2003–2011 (circles filled in black). The stars represent centers of population. P (Pitáycachi), T (Teras), and O (Otates) are the faults that ruptured in the 1887 earthquake. The boundaries of the five rectangles are used to subdivide the region for relocation purposes. The circles filled in red correspond to epicenters reported by the Bulletin of the International Seismological Centre originating between 22 March 1964 and 27 June 2013.

the initial locations made with Hypoinverse (Figure 5 top row) with those relocated with the SSST algorithm (middle and bottom rows in Figure 5) one can see that events initially located outside of the network (near 1120W and 28.50N) were eliminated for being poor located events (rms> 1.0 sec). These events are difficult to relocate with the SSST method because they are sparse and there are not enough events in their vicinity to calculate an adequate station correction term.

In the right column of Figure 5, the focal depths are grouped in 5-km bins. The depths obtained with the SSST method and model V4 (middle row) show two maxima, one at shallow depths (0-15 km), with 60.6% of the events, and another one near the base of the crust (35-40 km), with 12.8% of the events. On the other hand, most of the foci (84%) located with Hypoinverse have shallow depths (0-15 km). The events relocated with model V2 are all above 30 km, 52% concentrate between 5-15 km, 37% between 15-30 km and the rest (11%) above 5 km. Although the velocity models V2 and V4 give both low

residuals compared with other velocity models tested by Castro *et al*. (2010), the focal depth distribution obtained here with model V2 is more realistic, since all the events are located above the base of the crust and most of them (63%) have shallow depths (above 15 km), as observed in other regions of the Basin and Range province (e.g. Gomberg, 1991). Thus, model V2 is the preferred velocity model used in the next section to interpret the regional seismicity shown in Figures 4 and 6.

Seismotectonic interpretation

The seismicity originating 2003–2011 and relocated with the SSST method are displayed in maps and sections in Figures 1, 4 and 5 (lower row). It shows several clusters and alignments, which are placed here within their neotectonic framework. We also compare the distribution of seismicity of the period 2003–2007 (Castro *et al*. 2010) with the more recent one during 2008–2011.

As in the period 2003–2007, several microearthquakes of the period 2008–2011
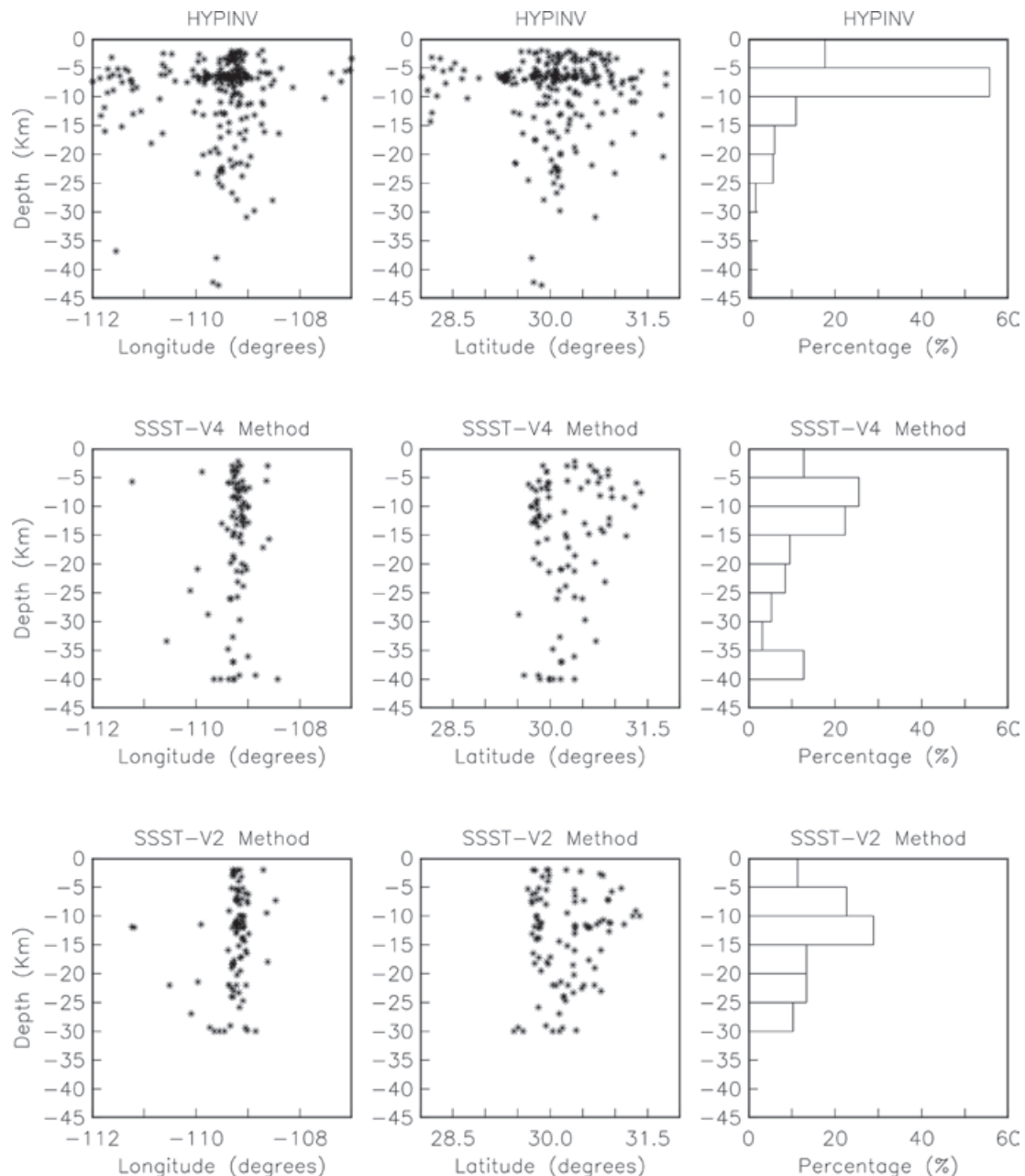
Figure 5. Focal depths calculated with the program Hypoinverse and velocity model V1 (top row) and with the SSST method and velocity models V4 (middle row) and V2 (bottom row). The graphs of the left column are east-west sections and the graphs of the central column north-south sections. In the right column, the focal depths are grouped in 5-km bins.

originated to the west and to the south of the segmented 1887 rupture trace (segments Pitáycachi, Teras, and Otates, marked by bold lines and letters P, T, and O, respectively in Figure 6). Four new events originated near and beyond the northern tip of the documented 1887 surface rupture, where additional events were recorded by the Earthscope USArray (Lockridge *et al.*, 2012). Two new events were recorded in 2008–2011 in the stepover between the Pitáycachi and Teras segments, and one additional event west of the Teras segment, but no additional event west of the Otates rupture segment (Figure 6). In the east-west section shown in Figure 5 (bottom row), the recorded microseismicity located along the 1887 rupture trace shows a well-defined subvertical alignment at 109.25° W from the surface to a depth of 30 km.
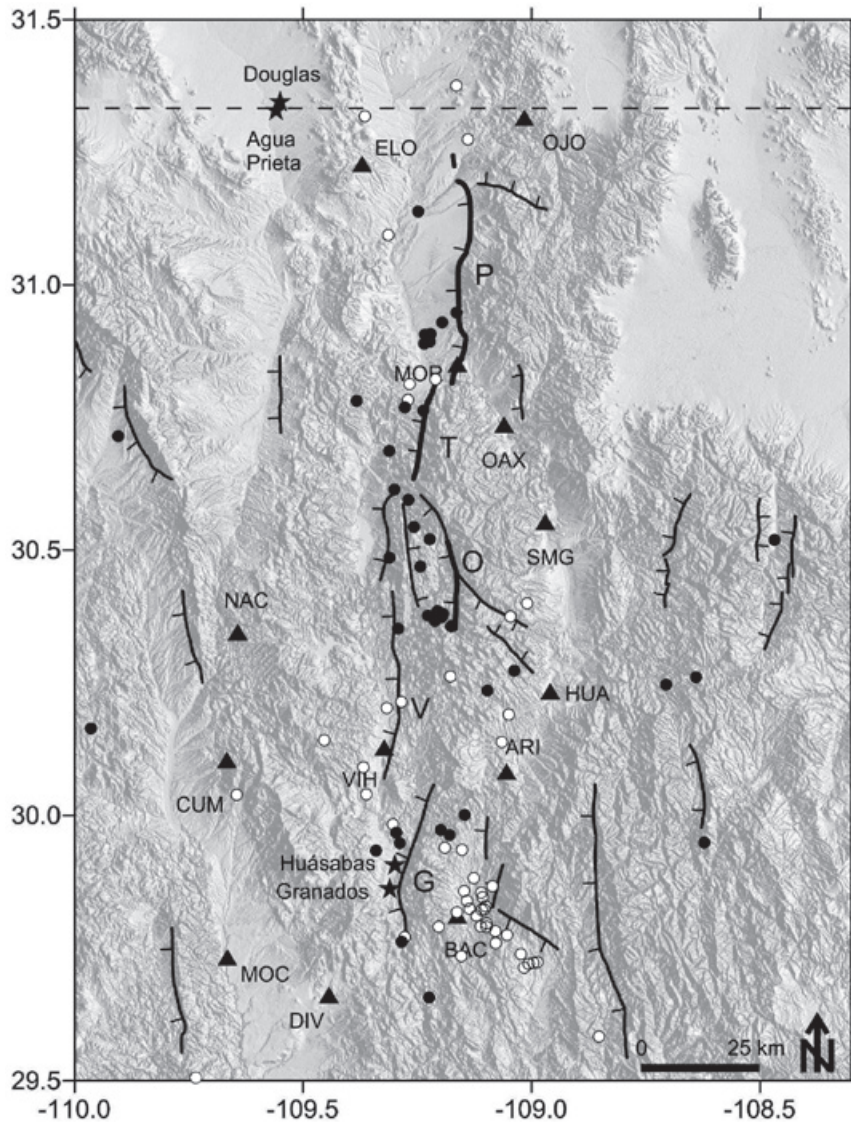
Figure 6. Relocated microseismicity epicenters originating between 2003 and 2011 and located near the faults that ruptured in 1887 (P, Pitáycachi; T, Teras; O, Otates) and the Villa Hidalgo (V) and Granados (G) faults. Circles filled in black correspond to epicenters originating 2003–2007 and circles filled in white to epicenters originating 2008–2011. The triangles indicate the locations of the seismic stations.

In addition to the two events documented by Castro *et al*. (2010), several new events occurred between 2008 and 2011 to the west of the Villa Hidalgo fault (V on Figure 6). Many new events were also recorded in the Bacadéhuachi basin, near station BAC (Figure 6). This basin is bound on its eastern side by several map-scale normal faults (Piguet, 1987; Montigny *et al*., 1987). Similarly to the microearthquakes recorded along the Villa Hidalgo fault and in the Granados-Huásabas area (Figure 6), these events can be explained by an increase in Coulomb failure stress in this region resulting from the 1887 rupture (Suter and Contreras, 2002). In an alternative interpretation of the microseismicity along these faults, the 1887 rupture may have extended farther south than documented and ruptured one or several of them. However, field checking of the trace of the Villa Hidalgo fault east of Villa Hidalgo did not reveal any obvious morphological or stratigraphic evidence for a recent rupture (Suter, 2013, personal comunication), neither did the detailed structural mapping by Piguet (1987) of the faults between Granados and the plateau of the Sierra Madre Occidental (Figure 6). Nevertheless, these faults should become the target of more detailed, field-based structural and stratigraphic studies to document their activity in the geologically recent past. North of the Bacadéhuachi basin, between stations ARI and HUA, near 109ºW (Figure 6) are three new events (white circles) and one that originated in the 2003-2007 period. These events could be the result of tensional stress that concentrates between the adjacent normal faults, the Villa Hidalgo fault on the west (V in Figure 6) and Otates on the east.

A NNW-SSE oriented epicenter alignment, 70 km long, can be seen on Figure 1, 30–40 km west of Cananea, in north-central Sonora. It is possible that some of these events are caused by mining excavations and the related redistribution of tectonic stress. However, they were removed from the catalog because were originated within the time window scheduled for the mining blasts. Local mapping and compilation of previous mapping by Manuel *et al*. (2011, plate 2) indicate that the major ranges of this region are bound by normal faults that displace bedrock against Miocene to Holocene sedimentary and volcanic rocks. The Imuris lineament (Figure 1), a major crustal discontinuity (Nourse *et al*., 1994; Nourse, 1995), passes across the mountain range located to the west of the epicenter alignment, where it is characterized by linear, unembayed regional-scale fault scarps. However, no detailed neotectonic studies exist of this region. Historical earthquakes in the general vicinity of the recorded microseismicity alignment are the 30 March 1916 MMImax VI Nogales and the 16 October 1999 ML 4.5 MMImax VI Magdalena earthquakes (Suter, 2001), as well as an additional 15 June 1897 earthquake felt in the Magdalena area (Boletín Mensual del Observatorio Meteorológico Central de México, 1897, p. 80). Figure 4 shows three events relocated in this area and two reported by the Bulletin of the International Seismological Centre (red circles in Figure 4).

Another major seismicity cluster is observed near Nacozari (station NAC on Figure 1), which is characterized by intense copper mining activity. Since I filtered quarry blasts from the catalog they are absent in the maps of relocated events (Figures 4 and 6), and it is likely that most of these events are mining-related earthquakes, such as mining-induced implosions by rock collapse (Ford *et al*., 2008; Julià *et al*., 2009).

Discussion

The seismicity detected by the RESNES array in the period 2008–2011 shows a concentration of events along and southward of the fault segments that ruptured during the 3 May 1887 Mw 7.5 earthquake (Figure 6). This distribution of seismicity enhances the pattern recorded between 2003 and 2007 by the same network (Castro *et al*., 2010) and can be interpreted as long-lasting aftershock activity taking place in the epicentral area of the 1887 main shock. Large intraplate earthquakes can increase locally the strain energy in the crust and can also increase the Coulomb stress significantly (Li *et al*., 2007). Changes in Coulomb failure

stress resulting from the 1887 earthquake calculated by Suter and Contreras (2002) correlate well with the distribution of events relocated in this study. Stein and Liu (2009) propose that the strain energy release from large intraplate earthquakes may dominate the local strain energy budget for many years following the main shock.

Comparing the errors in location reported by Castro *et al*. (2010) with those obtained in this study, in term of travel time residuals, Figure 7 shows that 83.2% of the events relocated in this study and 91.1% of the events relocated by Castro *et al*. (2010) have average residuals of less than 0.5 sec. Although the method (SSST) and the velocity model (V2) used in both studies is the same, Castro *et al*. (2010) used a larger number of additional stations, from the NARS-Baja and USArray networks. These explain why more events with small average residuals were obtained by Castro *et al*. (2010).

Based on the parametric catalog of the historical seismicity of northeastern Sonora by Suter (2001) and the seismicity recorded by RESNES during 2003–2007, the region southwest of the RESNES array, near Hermosillo, seems to be seismically inactive (Castro *et al*., 2010), which is confirmed by the lack of events recorded during 2008–2011. To verify whether this observation is not due to limitations in detection capability of the
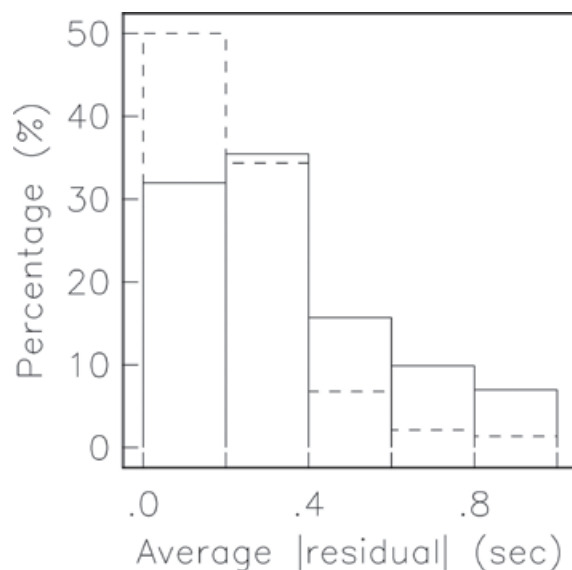

Figure 7. Histogram of the average absolute value of travel-time residuals. Solid lines, SSST relocations using velocity model V2 (Figure 3 and Table 2) and dashed lines for the relocations reported by Castro *et al*. (2010) with the same velocity model.

RESNES network, we searched the Bulletin of the International Seismological Centre (ISC) for earthquakes occurring in our region of interest. Figure 4 (circles filled in red) displays the epicenters reported in the ISC Bulletin from their earliest entry in 1964 to June 2013. Some of the events reported by ISC near Hermosillo are earthquakes caused by motion along faults in the Gulf of California. It is likely that the few events located on the continent are poorly located and actually originated in the Gulf of California. ISC also reports two events southwest of Cananea, next to the Imuris lineament, including the 16 October 1999 ML 4.5 Magdalena earthquake already mentioned previously, and several events near Nacozari. Two of the latter were flagged by the ISC as possible mine blasts, other ones may have been caused by mining excavations and the related redistribution of tectonic stress. Castro *et al.* (2010) located a larger number of events near Cananea because they eliminated events that occurred only on the schedule provided by the mining company or events having wave forms typical of blasts. In this study all the events within the time window of the blast schedule (from 18:45 hr UT to 04:30 hr UT) were eliminated and the time window was extended 45 min before and 90 min after the schedule in case the blast started before or after the schedule programed.

Conclusions

The microseismicity recorded by the RESNES array during 2003–2011 is mostly located in the epicentral area of the 3 May 1887 Mw 7.5 earthquake, which confirms that this large intraplate event is still generating aftershocks. Most of the relocated earthquakes originated at a crustal depth close to the fault segments that are known to have ruptured in 1887. Additionally, much microseismicity was recorded near the Basin and Range Province faults located to the south of the 1887 rupture, such as the Villa Hidalgo and Granados faults, and the faults bounding the Bacadéhuachi basin. The distribution of seismicity correlates well with numerical models of the changes in Coulomb failure stress resulting from the 1887 earthquake. More knowledge about the past activity of these faults should be gained from field-based geological studies of their structure and Quaternary stratigraphy.

The NNW-SSE oriented alignment of microseismicity located beyond the RESNES network, to the west of Cananea, near the epicenter of the 16 October 1999 ML 4.5 Magdalena earthquake and near a major crustal discontinuity known as the Imuris lineament (Figure 1) is probably caused by mining excavations and the related redistribution of tectonic stress. Similarly, the cluster of microseismicity recorded in the Nacozari region is most likely due to mine tremors induced by rock bursting.

Data and resources

An extensive bibliography related to the 1887 earthquake is posted at www.geo.arizona.edu/gsat/1887eq/bibliography.html. It includes the digitized 1888 report by José Guadalupe Aguilera. The seismograms used in this paper were recorded by stations of the RESNES seismic array. Data from the RESNES network can be requested from the author of this study. Some figures were made using the Generic Mapping Tools (www.soest.hawaii.edu/gmt; Wessel and Smith, 2009). The digital elevation model in Figure 6 was created from SRTM (Shuttle Radar Topography Mission) data with Surfer®9 (www.goldensoftware.com).

Acknowledgments

References

Aguilera J.G., 1888, Estudio de los fenómenos séismicos del 3 de mayo de 1887. Anales del Ministerio de Fomento de la República Mexicana 10, 5-56.

Averill M.G., Miller K.C., 2013, Upper crustal structure of the southern Rio Grande rift: A composite record of rift and pre-rift tectonics, in New Perspectives on Rio

Grande Rift Basins: From Tectonics to Groundwater, M. R. Hudson, and V. J. S. Grauch (Editors), *Geological Society of America Special Paper* 494, p. 463–474, doi:10.1130/2013.2494(17).

Castro R.R., Shearer P.M., Astiz L., Suter M., Jacques-Ayala C., Vernon F., 2010, The long-lasting aftershock series of the 3 May 1887 Mw 7.5 Sonora earthquake in the Mexican Basin and Range Province. *Bull. Seism. Soc. Am.* 100, 1153-1164.

de Polo C.M., Clark D.G., Slemmons D.B., Ramelli A.R., 1991, Historical surface faulting in the Basin-and-Range province, western North America–Implications for fault segmentation. *J. Struct. Geol.*, 13, 123-136.

Ford S.R., Dreger D.S., Walter W.R., 2008, Source Characterization of the 6 August 2007 Crandall Canyon Mine Seismic Event in Central Utah. *Seism. Res. Lett.*, 79, 637-644, doi:10.1785/gssrl.79.5.637.

Gomberg J., 1991, Seismicity and detection/location threshold in the Southern Great Basin Seismic Network. *J. Geophys. Res.,* 96, 16401-16414.

Goodfellow G.E., 1888, The Sonora earthquake. Science 11, 162-166.

Harder S., Keller G.R., 2000, Crustal structure determined from a new wide-angle seismic profile in southwestern New Mexico, in Southwest Passage: a trip through the Phanerozoic, New Mexico Geological Society Guidebook, Fifty-First Annual Field Conference, T. W. Lawton, N. J. McMillan, and V. T. McLemore (Editors), New Mexico Geological Society, Socorro, p. 75-78.

Julià J., Nyblade A.A., Durrheim R., Linzer L., Gök R., Dirks P., Walter W., 2009, Source Mechanisms of Mine-Related Seismicity, Savuka Mine, South Africa. *Bull. Seism. Soc. Am*., 99, 2801-2814, doi:10.1785/0120080334.

Klein F.W., 2002, User's guide to HYPOINVERSE-2000, a Fortran program to solve for earthquake locations and magnitudes, USGS Open File Report 02-171, 121pp.

Li Q., Liu M., Zhang Q., Sandvol E., 2007, Stress evolution and seismicity in the central-eastern United States: Insights from geodynamic modeling, in Continental Intraplate Earthquakes: Science, Hazard, and Policy Issues, S. Stein, and S. Mazzotti (Editors), *Geological Society of America Special Paper* 425, 149–166.

Lin G., Shearer P.M., 2005, Test of relative earthquake location techniques using synthetic data. *J. Geophys. Res.,* 110, B04304, doi:10.1029/2004JB003380.

Lockridge J.S., Fouch M.J., Arrowsmith, J. R., 2012, Seismicity within Arizona during the deployment of the EarthScope USArray transportable array. *Bull. Seismol. Soc. Am.* 102, 1850-1863, doi: 10.1785/0120110297.

Manuel D.J., Lawton T.F., González-León C., Iriondo A., Amato J.M., 2011, Stratigraphy and age of the Upper Jurassic strata in north-central Sonora, Mexico: Southwestern Laurentian record of crustal extension and tectonic transition. *Geosphere*, 7, 390–414; doi: 10.1130/GES00600.1.

Montigny R., Demant A., Delpretti P., Piguet P., Cochemé J.J., 1987, Chronologie K/Ar des séquences volcaniques tertiaires du nord de la Sierra Madre Occidental (Mexique). Comptes Rendus de l'Académie des Sciences, série II, 304(16), 987-992.

Natali S.G., Sbar M.L., 1982, Seismicity in the epicentral region of the 1887 northeastern Sonora earthquake, Mexico. *Bull. Seism. Soc. Am.*, 72, 181-196.

Nourse J.A., 1995, Jurassic-Cretaceous paleogeography of the Magdalena region, northern Sonora, and its influence on the positioning of Tertiary metamorphic core complexes, in Studies on the Mesozoic of Sonora and adjacent areas, C. Jacques-Ayala, C. M. González-León, and J. Roldán-Quintana (Editors), *Geological Society of America Special Paper* 301, p. 59–78.

Nourse J.A., Anderson T.A., Silver L.T., 1994, Tertiary metamorphic core complexes in Sonora, northwestern Mexico. *Tectonics*, 13, 1161-1182.

Orozco y Berra J., 1887, Efemérides séismicas Mexicanas, Memorias de la Sociedad Científica Antonio Alzate 1, 303-541.

Orozco y Berra J., 1888, Efemérides séismicas Mexicanas, adiciones y rectificaciones, Memorias de la Sociedad Científica Antonio Alzate 2, 261-288.

Piguet P., 1987, Contribution à l'étude de la Sierra Madre Occidental (Mexique): La séquence volcanique tertiaire de la transversale Moctezuma – La Norteña: Université de Droit, d'Economie et des Sciences d'Aix-Marseille, Faculté des Sciences et Techniques de St-Jérome, Thèse pour obtenir le grade de Docteur en Sciences, 208 p.

Richards-Dinger K., Shearer P., 2000, Earthquake locations in southern California obtained using source-specific station terms. *J. Geophys. Res*., 105, 10,939-10,960.

Stein S., Liu M., 2009, Long aftershock sequences within continents and implications for earthquake hazard assessment. *Nature*, 462, 87-89.

Suter M., 2001, The historical seismicity of northeastern Sonora and northwestern Chihuahua, Mexico (28-32° N, 106-111° W), *J. South Am. Earth Sci.,* 14, 521-532.

Suter M., 2006, Contemporary studies of the 3 May 1887 Mw 7.5 Sonora, Mexico (Basin and Range Province) earthquake. *Seism. Res. Lett.,* 77, 2, 134-147.

Suter M., 2008a, Structural configuration of the Otates fault (southern Basin and Range Province) and its rupture in the 3 May 1887 MW 7.5 Sonora, Mexico, earthquake. *Bull. Seism. Soc. Am.*, 98, 2879-2893.

Suter M., 2008b, Structural configuration of the Teras fault (southern Basin and Range Province) and its rupture in the 3 May 1887 MW 7.5 Sonora, Mexico earthquake. *Revista Mexicana de Ciencias Geológicas,* 25, 179-195.

Suter M., Contreras J., 2002, Active Tectonics of Northeastern Sonora, Mexico (Southern Basin and Range Province) and the 3 May 1887 MW 7.4 Earthquake. *Bull. Seismol. Soc. Am.,* 92, 581-589.

Vázquez L., 1887, El terremoto del 3 de Mayo, La Constitución, Periódico Oficial del Gobierno del Estado (Hermosillo, Sonora) 9, 24, 1–2.

Wallace T.C., Domitrovic A.M., Pearthree P.A., 1988, Southern Arizona earthquake update. Arizona Geology 18, 4, 6-7.

Wallace T.C., Pearthree P.A., 1989, Recent earthquakes in northern Sonora. *Arizona Geology* 19, 3, 6-7.

Wessel P., Smith W.H.F., 2009, The Generic Mapping Tools (GMT) version 4.5.0 technical Reference & Cookbook, SOEST/NOAA.

Yeats R.S., Sieh K., Allen C.R., 1997, The geology of earthquakes, Oxford University Press, Oxford, United Kingdom, 568 p.

Yeats R., 2012, Active faults of the World, Cambridge University Press, Cambridge, United Kingdom, 621 p.